Communauté UNIVERSITÉ Grenoble Alpes

THÈSE

Pour obtenir le grade de

DOCTEUR DE LA COMMUNAUTÉ UNIVERSITÉ GRENOBLE ALPES

Spécialité : Sciences de la Terre et de l'Univers et de l'Environnement (CESTUE)

Arrêté ministériel : 25 mai 2016

Présentée par

Tijan MEDE

Thèse dirigée par **Guillaume CHAMBON**, Directeur de recherches, IRSTEA et codirigée par **François NICOT**, Directeur de recherches, IRSTEA

préparée au sein du **Laboratoire IRSTEA Grenoble**
dans **l'École Doctorale Terre, Univers, Environnement**

Étude numérique du comportement mécanique de la neige: une perspective microstructurale

Numerical investigation of snow mechanical behaviour: a microstructural perspective

Thèse soutenue publiquement le **6 février 2019**,
devant le jury composé de :

Monsieur Farhang RADJAÏ
Directeur de Recherche, CNRS, Président
Monsieur Jürg SCHWEIZER
Directeur de Recherche, WSL/SLF, Rapporteur
Madame Barbara FRIGO
Maître de Conférences, Politecnico di Torino, Examinateur
Monsieur Eduardo ALONSO
Professeur, Universidad Politécnica de Cataluña, Examinateur
Madame Lydie STARON
Chargé de Recherche, Institut Jean le Rond d'Alembert, Examinateur
Monsieur Guillaume CHAMBON
Directeur de Recherche, IRSTEA, Directeur de thèse
Monsieur François NICOT
Directeur de Recherche, IRSTEA, Co-directeur de thèse
Monsieur Pascal HAGENMULLER
Ingénieur des Ponts, des Eaux et des Forêts, CEN, CNRM, Co-encadrant de thèse

In the memory of Alen Mlekuž.

Abstract

Dry slab snow avalanches represent a major natural hazard that is extremely difficult to manage. Attempts to model this phenomenon are hindered by the lack of a constitutive law that would describe the mechanical behaviour of snow on a material scale. In particular, relatively little is known on the failure and post-failure response of snow at high loading-rates. The highly fragile nature of the material in this deformation regimerenders experimental investigation difficult and complicates observation at the microstructural level.

As an alternative to experiments, a Discrete Element Method-based numerical model of snow is developed in this thesis. The model enables us to simulate the response of snow to mechanical loading, while accounting for actual snow microstructure by using X-ray attenuation images of snow microstructure as input. Snow is considered as a cohesive granular material and an original methodology is developed in order to model the shape of each grain. Individual grains are bound into the snow matrix by modelling cohesion between neighbouring grains.

The model is then used to explore the macroscopic mechanical response of different snow samples to mixed-mode loading. Three typical modes of failure are observed in all tested snow samples, depending on the level of applied normal stress: a localized shear failure at low normal stress (mode A), a shear failure-induced volumetric collapse at intermediate levels of normal stress (mode B), and a normal failure and collapse for high values of normal stress (mode C). The observed failure modes result in closed failure envelopes and no qualitative difference is observed between the mechanical responses of different snow types.

The internal mechanisms that lead to volumetric collapse are further examined on the microscale. Force chain buckling is identified as a trigger of this material instability. Additionally, force chain stability appears to be controlled by the contacts between the force chain members and the surrounding grains. The failure in these contacts, which is evidenced in modes B and C, allows force chain buckling to develop and results in subsequent volumetric collapse.

Résumé

Les avalanches de plaque représentent un risque naturel majeur dont la prévision demeure très difficile. Le manque de lois constitutives fiables à l'échelle du matériau rend difficiles les tentatives de modélisation de ce phénomène. Plus spécifiquement, la réponse mécanique de la neige durant et après la rupture, dans des régimes de chargements rapides , demeure relativement méconnue. La nature particulièrement fragile du matériau au sein de ce régime de déformation rend ardue la réalisation d'expériences et complique l'observation à l'échelle microstructurale.

Dans ce travail de thèse, un modèle numérique de neige fondé sur la Méthode des Éléments Discrets a été développé en tant qu'alternative aux expériences. Le modèle nous permet de simuler la réponse de la neige à des chargements mécaniques en tenant compte de la microstructure réelle du matériau grâce à l'intégration d'images acquises par microtomographie à rayons X en entrée du modèle. La neige est considérée comme un matériau granulaire cohesif, et une méthode originale a été développée afin de modéliser la forme de chaque grain. Les grains individuels sont ensuite assemblés pour reconstituer la matrice de la neige grâce à la prise en compte de lois de contact cohésives.

Le modèle a été utilisé afin d'explorer la réponse mécanique macroscopique de différent échantillons de neige à un chargement mixte normal-cisaillant. Trois modes de rupture ont été observés dans tous les échantillons de neige testés, en fonction du niveau de contrainte normale appliquée : une rupture en cisaillement localisée pour des niveaux de contrainte normale faibles (mode A), un effondrement normal induit par rupture en cisaillement à des niveaux intermédiaires de contrainte normale (mode B) et un effondrement normal pour des valeurs de contrainte normale élevées (mode C). Ces différents modes de rupture produisent une enveloppe de rupture fermée dans l'espace des contraintes, ce pour les différents types de neige étudiés.

Les mécanismes internes conduisant à l'effondrement normal des échantillons ont été étudiés plus en détail à l'échelle microscopique. Il a été montré que ce mode de rupture était associé à un mécanisme de flambement des chaînes de force. En outre, la stabilité de ces chaînes de force semble être contrôlée par les contacts entre les éléments des chaînes et les grains environnants. La rupture de ces contacts, observée dans les modes B et C, autorise le développement du flambement des chaînes de force et aboutit à

l'effondrement volumique.

Acknowledgements

First of all I would like to thank my supervisors for the trust that they invested in me and the scientific support that that offered me during these three years. Let me start by expressing my appreciation for all the interesting scientific debates with François. Studying his previous work and hearing his point of view during the debates regarding my work opened my eyes to a completely different understanding of the field as well as science in general. Next, I would like to thank Pascal for the support on the snow-related issues and all the interesting ideas that he contributed. And finally, I want to thank Guillaume for his absolutely outstanding mentorship. His door was always opened for me and he always found time for much needed discussions. He was able to find that thin line between leaving me my academic freedom to make my own decisions (as well as my own mistakes) and offering leadership when needed. Moreover, when problems arose, he offered prudent advice and managed to guide me towards a solution even when I could not see one. But the thing I admire the most was the calmness with which he handled the difficulties during my PhD. Rather than showing frustration in the face of problems, Guillaume radiated competence, constructiveness and composure which inspired confidence and helped enormously with my work. This is truly something which I intend to look up to, wherever my future might take me. Thank you Guillaume.

I would also like to express my gratitude to the members of the jury for travelling so very far to hear my PhD defence. It was and honour hosting such prominent names as Farhang Radjaï, Jürg Schweizer, Eduardo Alonso, Lydie Staron and Barbara Frigo. Their comments were most constructive and the debate that followed after the PhD defence was truly interesting.

Of course life does not stop for a PhD and keeping the spirits up during the three years is every bit as important as the work. The latter was made easier by the Irstea collective, particularly mu wonderful officemates Alexandra, Florie and Ségolène. Florie, the smile on your face and the kindness you radiated truly made the office feel like home. And Alexandra... my stay in France would not have been the same without you. It was you who introduced my to the ways of French language and culture for which I will forever be grateful. Thank you for all the bad moments in which you supported me and thank you for all the wonderful times we spent together.

Next I need to mention my group of friends from 3SR, who accepted me as a member of their own laboratory and who often felt like my real co-workers. I would particularly like to address Fabio, Bratislav, Eleni, Sonja and of course Cino. Thank you for all the late night beer sessions, all the laughs, dinners, band practices, skiing/snowboarding days and Montpellier adventures. Not to mention all the free croissants on Fridays.

However the people that really felt like family here in France were my flatmates Etienne, Anouk, Vadim, Pierre and Julia. It was them that made Grenoble feel like home and took me with them to so many adventures in the mountains.

Finally I want to thank my own family and friends for all the support during my PhD. Mom, dad, thank you for coming to my defence. Mateja, thank you for being my biggest supporter. You were always there for me and I appreciate it enormously. Timon and all the friends, thank you for all the visits in France and all the shenanigans elsewhere.

Contents

Chapter 1

Introduction

1.1 Context

Snow avalanches represent one of the major natural hazards in mountainous areas with seasonal or permanent snow cover. The destructive force of these rapidly descending snow masses is claiming a substantial human life toll as well as considerable damage to the infrastructure. The average number of snow avalanche casualties worldwide is estimated at 250 per year [Meister, 2002] and in the year 1999 in Switzerland alone, the direct costs incurred by insurance companies due to the damage caused by avalanche and snow loads exceeded 1 billion Swiss francs [Ancey, 2001].

Much about the release process remains unknown, mainly due to the highly variable, layered character of the snowpack, a highly porous material that exists close to its melting point [Schweizer et al., 2003]. It is however clear that snow avalanche release results from a complex interaction between terrain, snowpack, and meteorological conditions. The risk related to snow avalanches is currently managed by two separate approaches: short-term forecasting and long-term prevention.

Most countries with mountainous areas and seasonal snow employ an avalanche forecasting service that informs the public on the short-term risk of snow avalanche occurrence. The avalanche risk is given on an international scale from 1 (low) to 5 (high), along with the avalanche type and most favourable conditions for release. The risk assessment for a particular location is performed by the snow avalanche forecaster on the basis of performed snowpack measurements and human expertise. In France, the forecaster is aided by the national operational avalanche risk forecasting model SAFRAN-CROCUS-MEPRA, which computes the stability index as a function of the past and modelled weather conditions [Durand et al., 1999]. Effectively, the risk assessment is not performed in a deterministic manner, but rather depends on the expertise of the forecaster who heuristically weights different contributory factors.

The long-term prevention is based on hazard mapping, where the risk of snow avalanches is primarily assessed statistically from the observation performed over a large span of years. The historical data, needed for hazard mapping consists of either direct observations of snow avalanche deposition or indirect

observations such as the distribution of damage, caused by a snow avalanche [De Crécy, 1980]. However, since this kind of data is not available everywhere over a sufficiently long period, statistical models must be coupled with physically based models to overcome the limitations of missing historical data [Gaume, 2012]. The resulting hazard maps are used to regulate urbanism in mountainous areas and determine zones where construction is either permitted, either not permitted or, permitted provided they can sustain a certain mechanical load.
Although these established tools of snow avalanche risk management have proven effective, our knowledge on snow avalanche release and forecasting ability is still limited, leaving room for improvement. The increase in computing power and development of numerical tools in recent years have however opened unprecedented new prospects for snow avalanche risk management. As opposed to qualitative or semi-quantitative manner in which the effect of meteorological conditions or the mechanical response of snow is predicted in the established tools, currently developed numerical models aim for fully quantitative description of snow physics [Hagenmuller et al., 2015; Gaume et al., 2017a]. Large spatial and temporal variability of the snowpack, will most likely preclude fully deterministic models to be applied to snow avalanche modelling, but a probabilistic approach, based on accurate constitutive behaviour of snow on the material scale as well as the snow avalanche mechanics on the macroscale seems a realistic perspective. Although the field of numerical approaches to modelling in snow avalanche research is relatively new, it already shows a great potential.

1.2 Snow avalanche formation

Snow avalanches are generally classified into two separate types that differ in the mechanism of release and subsequently also in the necessary conditions for release and the typical volume of involved snow [Schweizer et al., 2003]:

- **Loose snow avalanches** occur in snow with a small amount of internal cohesion. These avalanches start from a point on the surface and then gradually gain volume by setting into motion more and more loose snow as they move down the slope. The initial failure is analogous to rotational slip in cohesionless sands or soils [Wittmer et al., 1996;

Schweizer et al., 2003]. The release volume as well as the final volume of avalanche are normally much smaller than those of slab avalanches.

- **Slab avalanches** involve a simultaneous release of a much larger volume than loose snow avalanches. The prerequisite for a slab avalanche is an existence of a weak layer underlying a cohesive slab of snow. The weak layer is loaded by the overlying slab and potential additional perturbations (skiers, animals etc.) in shear and normal mode. If the strength of the weak layer is locally exceeded, a localized initial failure occurs. Once the initial failure reaches a critical size, it starts propagating along the slope, diminishing support to the overlying slab. The loss of support in the weak layer creates tensile and bending stresses in the slab, which can eventually lead to failure of slab along a crown crack and the release of a slab avalanche.

Schweizer et al. [Schweizer et al., 2003] have classified five general contributory factors that influence the release of a snow avalanche: terrain, precipitation, wind, temperature and stratigraphy. The influence of these contributory factors is often interrelated and cannot be uncoupled, but in general they influence either the strength of snow or the external loading of snow in the following manner:

- **Terrain**: The slope influences the loading conditions of snow in terms of the ratio between the shear and normal load and it has been observed that a slope of $>30\ ^\circ$ is generally required for the release of a dry slab avalanche. This angle however depends on the terrain roughness and vegetation which represent a stabilizing effect on the snowpack.

- **Precipitation**: New snowfall is the strongest snow avalanche contributory factor. 30-50 cm of new snowfall during a storm is considered the critical depth for the spontaneous release of snow avalanches, while depths >1 m are considered critical for the initiation of extreme avalanches. It is however not only the depth of the new snowfall, but also it's rate that contributes to snow avalanche risk. While the snowfall increases the load on the buried weaknesses, these buried layers build up strength over time under additional loading. If the snowfall rate is ≥ 2.5 cm h^{-1}, the loading rate is faster than the strength gaining rate and the risk of a snow avalanche is increased.

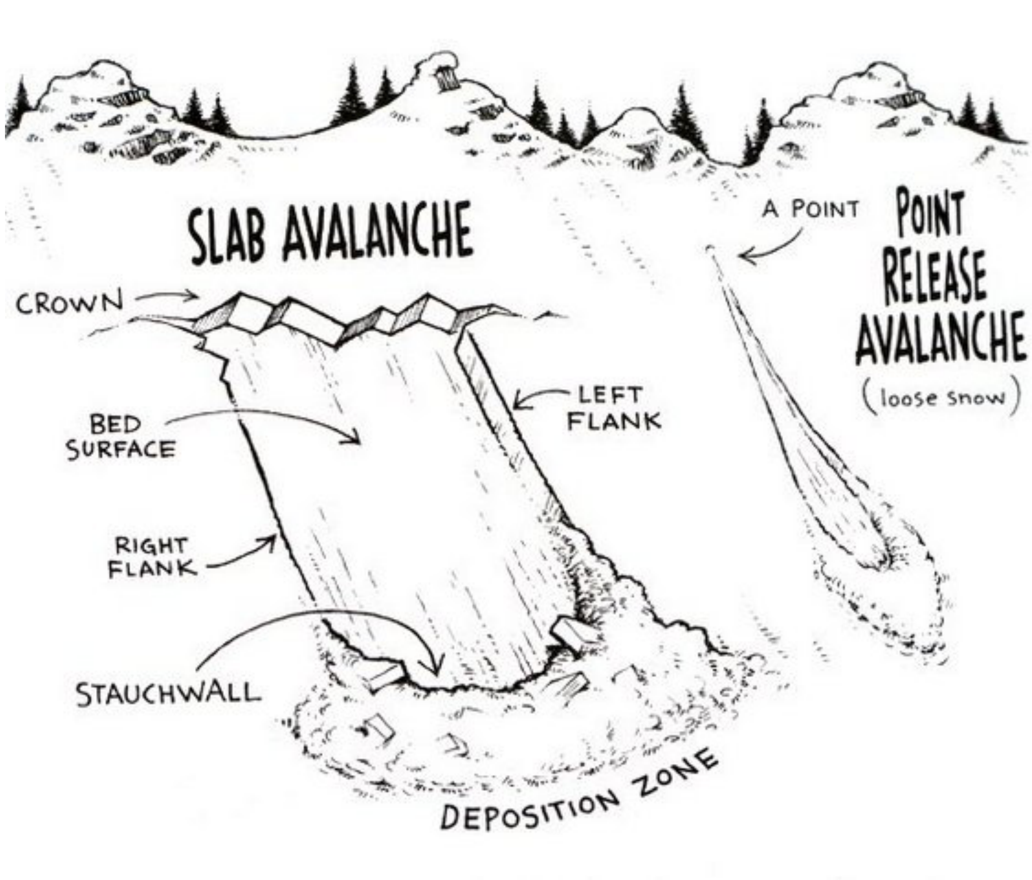

Figure 1.1: Schematic description of a slab avalanche and a point release avalanche [Clelland and O'bannon, 2012].

- **Wind**: Wind influences the snow avalanche release rate by redistributing the snow and creating a varying depth of snow cover with locally increased loading rates. Variations in wind speed and snow drift create layers of different density and hardness. The deposited snow has also been reported to be more brittle and therefore more prone to avalanching [De Quervain, 1966].

- **Temperature**: The influence of temperature or any incoming energy fluxes (radiation, rain, exchanges through air conductivity, convection) on the snow cover stability is complex, but it can be simplified into two groups of effects: (1) metamorphism of snow microstructure, which is dependent on temperature as well as temperature gradient and other factors and (2) direct influence of temperature on mechanical properties of snow including hardness, fracture toughness and strength.

- **Stratigraphy**: The layered structure of snow cover, referred to as snow cover stratigraphy is considered the key factor in dry snow slab avalanche release. Different layers of snow feature different microstructures with different mechanical properties. Existence of a weakness in the snow cover is a necessary, but not sufficient prerequisite for slab avalanche formation [Schweizer et al., 2003]. The instability and failure mechanism of weak snow layers that have the decisive effect on the release of the overlying slab are however poorly understood [Reuter and Schweizer, 2018].

1.3 Snow types

Snow cover is formed by snowflakes, generated in the atmosphere by water condensation around freezing nuclei [Jiusto and Weickmann, 1973]. Depending on the atmospheric conditions during the falling stage, these snow crystals take on different forms before they settle on the ground. Once on the ground, snow crystals continue to evolve depending on the atmospheric conditions and mechanical loads. This process is referred to as metamorphism and it creates layers of snow with varying microstructure (shape of ice grains, cross sections of the cohesive bonds between ice grains, porosity etc.). Individual typical microstructures are catalogued into so-called snow types, according to the international classification of seasonal snow on the ground [Fierz, 2009].

In general there are three main factors that influence ground snow metamorphism: vapour transport, melting and mechanical loading. Due to the fact that snow is a very porous material and that the atmospheric temperature is never far from its melting point, snow experiences intense vapour transport, which actively changes its microstructure by ice sublimation in certain regions and vapour condensation in other regions along the microstructure [Colbeck, 1997]. Low temperature gradient ($\nabla T \leq 5$ K m $^{-1}$) results in *equilibrium vapour exchange*, which tends to round off the snow grains and increase the size of cohesive bonds between the grains by promoting the vapour transport from convex to concave zones. Moderate and high temperature gradient ($\nabla T > 5$ K m $^{-1}$) on the other hand results in *kinetic vapour exchange*, promoting the metamorphism of snow grains into plane facets with sharp edges [Colbeck, 1983]. Melting and freezing cycles are known to increase the size of snow grains and produce rounded shapes. The quantity of liquid water in the snow matrix also influence the strength of the grain bonds - a low water content normally results in strong snow grain bonds, a moderate water content results in moderate capillary cohesion forces and high water content acts as a lubricant which decreases grain cohesion [Colbeck, 1974]. Finally, the mechanical load has a strong influence on the densification of snow, promoting sintering and strength increase of the snow cover.

As already mentioned, the stratigraphy that results from this complex interplay of atmospheric conditions and external loading has been identified as one of the major contributory factors to snow avalanche release and the existence of a weakness in the snow cover a necessary prerequisite for a slab avalanche release [Schweizer et al., 2003]. By definition this weakness refers to the layer of snow cover with a significantly lower ultimate strength under the applied mixed-mode loading conditions (Figs.1.2.a, 1.2.b) than the rest of the snowpack. Köchle and Schneebeli [2014] have noted that the weak layer is most clearly distinguished by a strong relative change in microstructure when compared to both adjacent layers, and not by any single descriptor of the microstructure. In general, the weak layer can consist of any snow type, but certain snow types are known to form persistent weak layers: faceted crystals (Fig. 1.2.c), surface hoar (Fig. 1.2.e) and depth hoar (Fig. 1.2.d) [Jamieson and Johnston, 1992]. These snow types are known to be extremely fragile and once formed in the snow cover, they can persist over extended periods of time with very little physical change as long as the snow temperature stays below freezing and the applied load is sufficiently low [Giddings and LaChapelle, 1962; Jamieson and Johnston, 1995]. Consequently, once formed, they pose a long-lasting risk for the release of a slab avalanche. Jamieson and Schweizer [2000] reported that although the large majority of avalanches during storms are released by nonpersistent weak layers, a majority of skier-triggered avalanches are released by weak layers of persistent grain types.

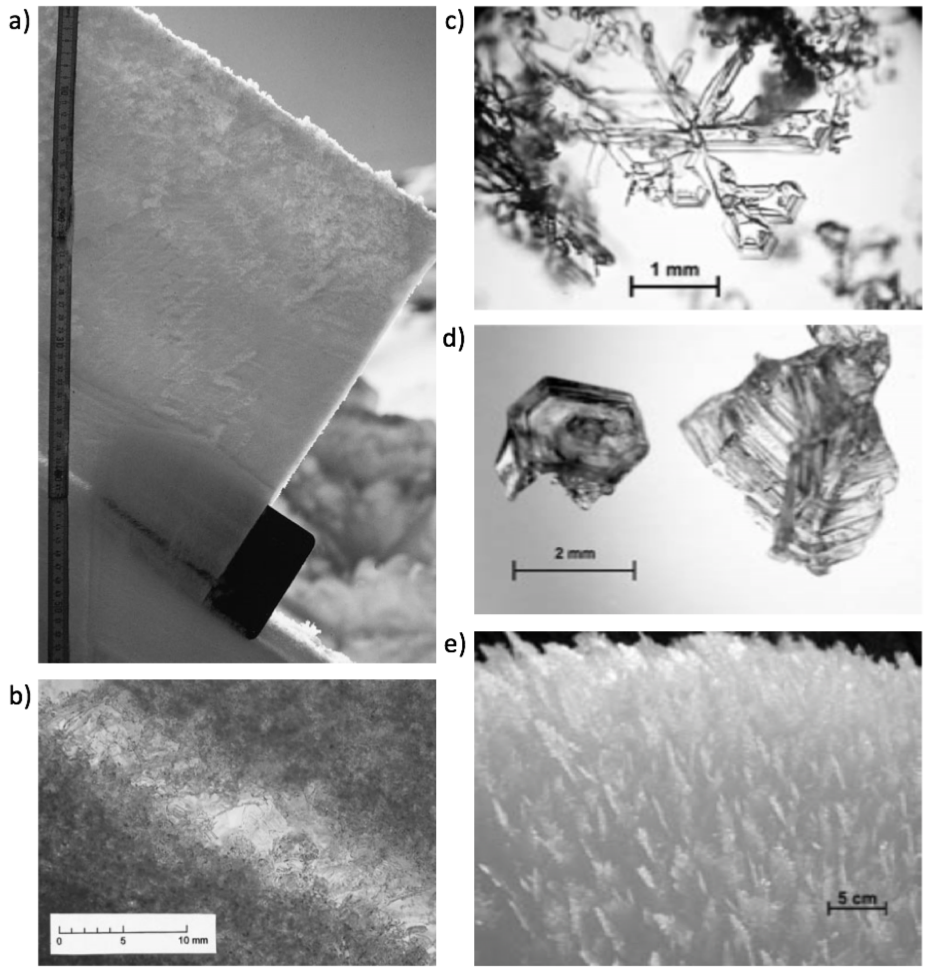

Figure 1.2: a) The remaining slab and a clearly visible weak layer after the release of an avalanche [Jamieson and Schweizer, 2000]. b) A zoom into the weak layer from image a). Examples of: c) faceted crystals, d) depth hoar and e) surface hoar, according to the international classification of seasonal snow on the ground [Fierz, 2009].

1.4 The scope of the thesis

Slab avalanches are known to be the most destructive type of snow avalanches as well as the most difficult ones to predict. Their release is linked to the failure of an underlying weakness in snow. The mechanics of failure of these weaknesses is recognized as a key ingredient for a deeper understanding and numerical modelling of snow avalanches.

The mechanical behaviour, particularly failure, of weak snow layers however remains poorly understood [Reuter and Schweizer, 2018]. The extremely low strength of weak layers and their sensitivity to environmental conditions render systematic experimental exploration difficult and complicate observation at the microscopic level.

The objective of this thesis is the exploration of mechanical behaviour of snow, relevant to the release of a dry slab snow avalanche. Particular emphasis will hence be given to the failure and post-failure response of different snow types under the loading conditions, experienced by the weak layer involved in dry slab avalanche initiation, namely low temperature and high strain rates. The research will therefore be limited to:

- mixed-mode shear and normal loading
- low temperatures ($T < 0°C$)
- strain rates $\dot{\gamma} > 10^{-4}s^{-1}$

The current state of the art on the topic of snow response to shear and normal loading is discussed in the next chapter, which is concluded by a detailed formulation of the scientific questions as well as a summary of the thesis structure.

Chapter 2

State of the art: snow under shear and normal loading

2.1 Experimental investigations

2.1.1 Constitutive mechanical behaviour of snow

Narita [1980, 1984] performed a large number of uniaxial tensile tests on snow samples of densities between 240 and 470 kg m^{-3} for varying strain rates $\dot{\varepsilon}$. With respect to strain rate, he identified four distinct deformational regimes (Fig. 2.1.a): type A ($\dot{\varepsilon} > 2.4 \cdot 10^{-4} s^{-1}$), marked by quasi-elastic stress build-up, followed by brittle fracture; type B ($7 \cdot 10^{-5} s^{-1} < \dot{\varepsilon} < 2.4 \cdot 10^{-4} s^{-1}$), where the elastic phase is followed by perfect plasticity and an abrupt rupture; type C ($10^{-6} s^{-1} < \dot{\varepsilon} < 7 \cdot 10^{-5} s^{-1}$), which differs from type B by the lack of abrupt rupture - instead, the stress is relieved by gradual strain softening; type D ($\dot{\varepsilon} < 10^{-6} s^{-1}$) where the response is governed by creep and a pronounced peak force is not observed. Narita also qualitatively described fracture and damage formation for each deformational regime (Fig. 2.1.b) and attributed the differences between the four regimes to viscous properties of the ice matrix as well as snow sintering process.

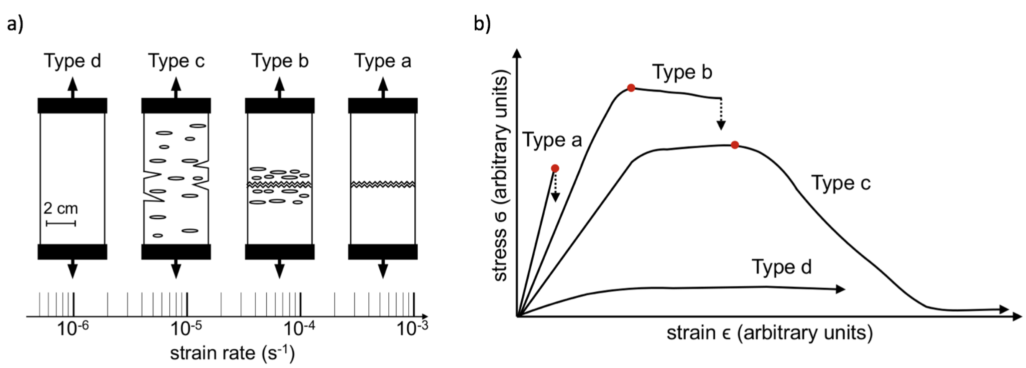

Figure 2.1: a) A graphical representation of the damage appearing in the four deformational regimes of the loaded samples. b) The typical stress-strain curves for the four deformational regimes of the loaded samples. Taken from Hagenmuller [Hagenmuller, 2014], who adapted it from Narita [Narita, 1984].

Similar qualitative observations on general shape of the stress-strain curve of snow were made by McClung [1977], de Montmollin [1982] and Schweizer [1998], who performed simple shear and mixed-mode loading experiments on natural snow in laboratory conditions under varying shear rates $\dot{\gamma}$. A (quasi) elastic deformation, followed by brittle fracture was observed for $\dot{\gamma} = 6.5 \cdot 10^{-3} s^{-1}$ [Schweizer, 1998]; a quasi-elastic deformation followed by strain hardening and an abrupt rupture for $\dot{\gamma} = 2.7 \cdot 10^{-4} s^{-1}$ [Schweizer, 1998], an elastic deformation, followed by strain hardening and a post-peak strain softening with no rupture for $\dot{\gamma} = 7.5 \cdot 10^{-5} s^{-1}$ [Schweizer, 1998] and a continuous strain hardening for $\dot{\gamma} < 1.2 \cdot 10^{-5} s^{-1}$ [McClung, 1977]. Similarly to Narita, de Montmollin attributed these influences of the strain rate on the stress-strain response to grain sintering that takes place during the test.

A strain rate in the vicinity of $10^{-4} s^{-1}$ was identified as transition from ductile to brittle response of snow under tensile as well as shear loading and the scope of the thesis allows us to limit our research to the brittle regime. Hence the following section, where the response of snow to mixed mode loading is studied, is partitioned into the following sub-sections according to the phases of the observed brittle response: quasi-elastic phase, ultimate strength and post-peak phase.

Quasi-elastic phase

The measured values of the Young's modulus E of snow scatter over several orders of magnitude (Fig. 2.2). The results were obtained with a variety of different measuring approaches.

Values between 20 MPa and 500 MPa have been obtained by uniaxial compression measurements on snow with densities between 400 and 900 kg m^{-3} [Kovacs et al., 1969]. Application of high frequency vibration tests resulted in Young's modulus values between 20 MPa and 1 GPa for snow densities between 210 and 900 kg m^{-3} [Nakaya, 1958; Smith, 1965; Sigrist, 2006]. Wave propagation measurement has also proven an efficient method for measuring Young's modulus of snow. The propagation of P waves depend on the density and the Young's modulus of the consitituting material. Providing that the density of the material is known, the elastic modulus can be calculated. Employing this methodology, Capelli et al. [2016] recovered E values between 30 MPa and 340 MPa for snow densities between 240 and 450 kg m^{-3}, while Gerling et al. [2017a] measured E values between 10 MPa and 340

MPa for snow densities between 170 and 370 kg m^{-3}. Several authors have attempted to recover the elastic modulus from the SnowMicropen (SMP) measurements. Marshall and Johnson [2009] reported elastic modulus values between 0.2 MPa and 20 MPa for variable snow types of density between 100 and 420 kg m^{-3}. Reuter et al. [Reuter et al., 2013] measured elastic modulus values between 1 MPa and 10 MPa for variable snow types of density between 100 and 350 kg m^{-3}. However after comparing these measurements with alternative measurements of E, the authors reported a shift of values of several orders of magnitude, rendering the SMP measurements of elastic modulus questionable.

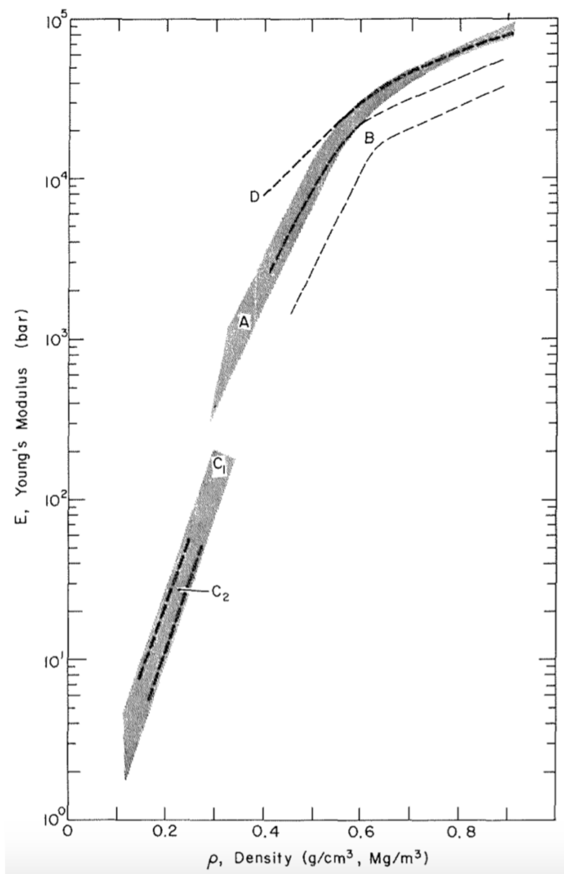

Figure 2.2: Comparison of various Young's modulus measurements synthesized by Mellor [1974].

Mellor [1974] summarized the results from a variety of different experimental campaigns and observed a roughly power law dependence of Young's modulus on the density of snow (Fig. 2.2).

Ultimate strength of snow

Effect of normal force: McClung [1977] performed direct simple shear tests on snow samples in laboratory conditions and reported a near-linear correlation between the peak shear stress and normal stress within the measured range (Fig.2.3.a) The linear relation between shear and normal stress at failure is typical of granular materials and usually referred to as the Mohr-Coulomb law [Terzaghi, 1951]. The results are consistent with in-situ shear frame measurements by Chandel et al. [2014b] as well as laboratory bevametre shear tests by de Montmollin [1982].

a) b)

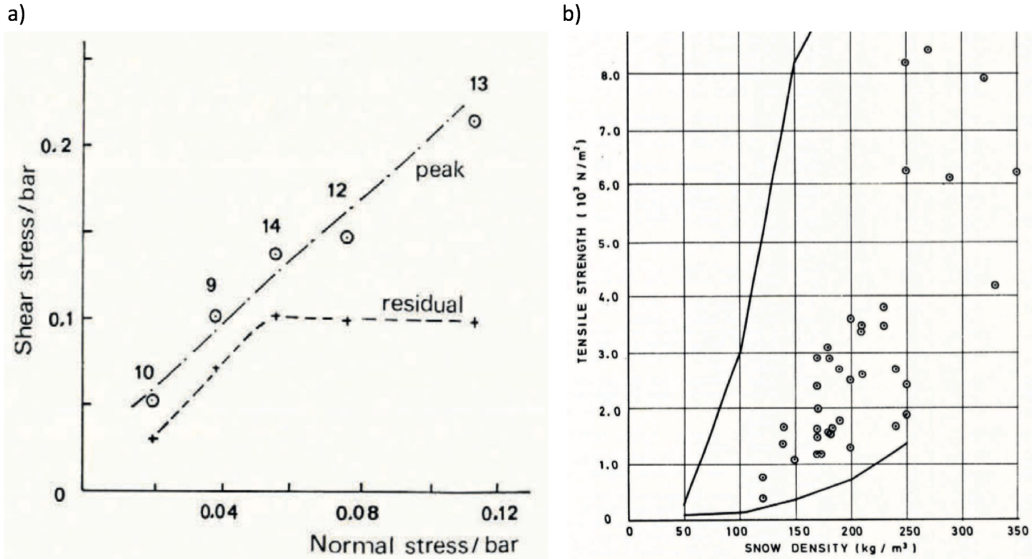

Figure 2.3: a) Dependency of the ultimate shear strength (peak force) and residual stress of similar snow samples to the applied normal stress [McClung, 1977]. b) Dependency of the ultimate tensile strength of snow samples to density [McClung, 1979a].

Effect of density: The most important easily measurable parameter to relate to tensile strength of snow is snow density [Sommerfeld, 1973]. Multiple independent laboratory measurement campaigns performed by Narita [1984], McClung [1979a] and Upadhyay et al. [2007] have recorded a clear dependency of the tensile strength of snow to density, but with a very large scatter. The amount of scatter suggests that snow density is an important, but not sufficient descriptor of snow structure to predict the ultimate tensile strength (Fig.2.3.b).

Effect of microstructure: It is considered that the strength of snow does not only depend on its density but also on its structure, i.e., diameter, length , orientation and number of ice bonds connecting the snow grains [Narita, 1984]. The significance of microstructure in controlling the mechanical properties of snow was also recognized by Mellor [1974] and Shapiro et al. [1997], who reviewed the most important experimental results of snow mechanics. Keeler and Weeks [1968] showed that two snow samples with the same density and different microstuructures may have strengths differing by as much as a factor of four. Narita [1984] concluded that the snow microstructure is likely to have a predominant effect on the strength of snow rather than density itself. The majority of experimental results however only list the density of the measured snow samples, without any additional information on the snow microstructure. A very small number of experimental studies also characterize the tested snow in terms of the international classification of snow types [Fierz, 2009], but it has not yet been established whether that is sufficient information to predict its ultimate strength. It has been suggested that crucial information on snow microstructure, namely the grain bonding system is missing from this description [Köchle and Schneebeli, 2014; Hagenmuller, 2014].

Post-peak behaviour of snow

McClung [1977], de Montmollin [1982] and Schweizer [1998] observed gradual strain softening after the shear stress peak for slow loading rates and a brittle failure for faster loading rates. While brittle failure represents the failure regime, relevant for slab avalanche release, not much is known on the immediate post-brittle failure behaviour of snow. From the fact that snow is a structure of sintered ice grains, one can speculate that a portion of this structure disintegrates into a cohesionless assembly of grains, which should follow the physical laws that govern the mechanical response of granular materials. Indeed McClung reports a near-linear correlation between residual stress after brittle fracture and the normal load (Fig. 2.3.a). The residual shear stress curve however levels off at a certain value of normal stress, which could be attributed to breakage of snow grains at a sufficiently high normal pressure.

2.1.2 Slab-weak layer system response

Experimental campaigns on snow samples which include a weak layer are of particular interest as their mechanical behaviour is considered analogous to that of a slab overlying a weak layer on a mountain slope. The experimental data on the response of such snow samples to shear and normal loading is scarce due to the difficulties of running systematic experiments on such a fragile structure. There are however several experimental measurements done in situ as well as in laboratory conditions.

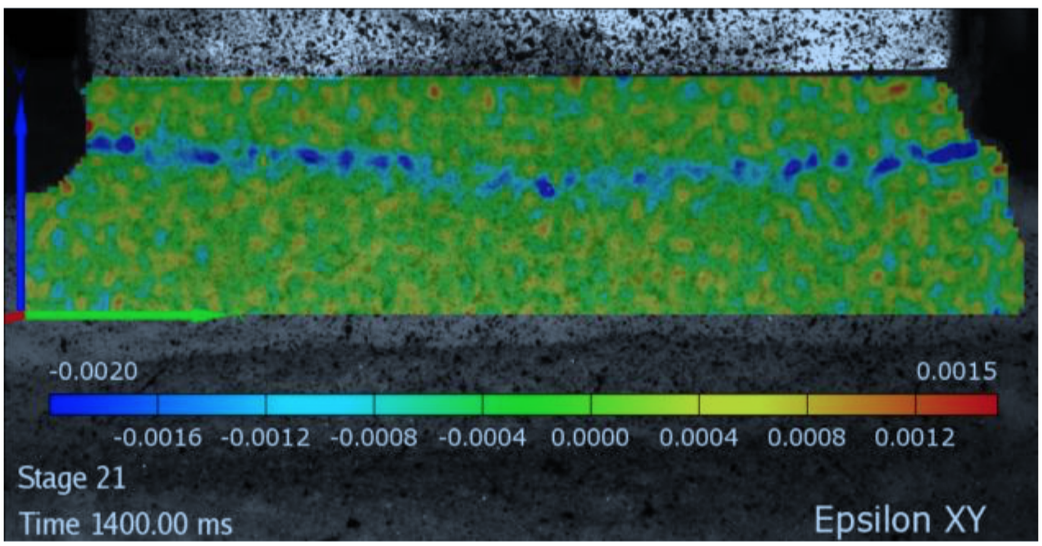

Figure 2.4: Strain concentration in the weak layer of the snow sample exposed to shear loading [Walters and Adams, 2012].

Walters et al. [2010]; Walters and Adams [2012], performed displacement controlled shear tests on samples containing a weak layer of faceted crystals in laboratory conditions and used an optical strain measuring system to show that the strain in the specimen is highly concentrated in the weak layer, which is also where the subsequent fracture occurs. Reiweger and Schweizer [2013], who performed load controlled laboratory shear experiments on snow samples with a faceted or depth hoar weak layer, confirmed this claim by utilizing particle image velocimetry (PIV). Thus, the response of a snow specimen containing a weak layer to shearing or a combination of normal and shear loading, is governed by the properties of the weak layer, where the prevailing portion of the strain is concentrated where the final failure occurs.

Fukuzawa and Narita [1992] performed simple shear tests on snow samples with a layer of laboratory created depth hoar at varying strain rates. Similarly to homogeneous snow, the response of snow samples with weak layer exhibited ductile deformation at low strain rates and brittle failure at high strain rates. Ductile deformation was marked by gradual strain hardening, followed by strain softening, while brittle regime featured a quasi-elastic phase, followed by abrupt rupture. The transition from ductile to fragile regime was found at $\dot{\gamma} \approx 2 \cdot 10^{-4}$ s^{-1}, which is very similar to transition strain rate found for homogeneous snow [Narita, 1984; Schweizer, 1998].

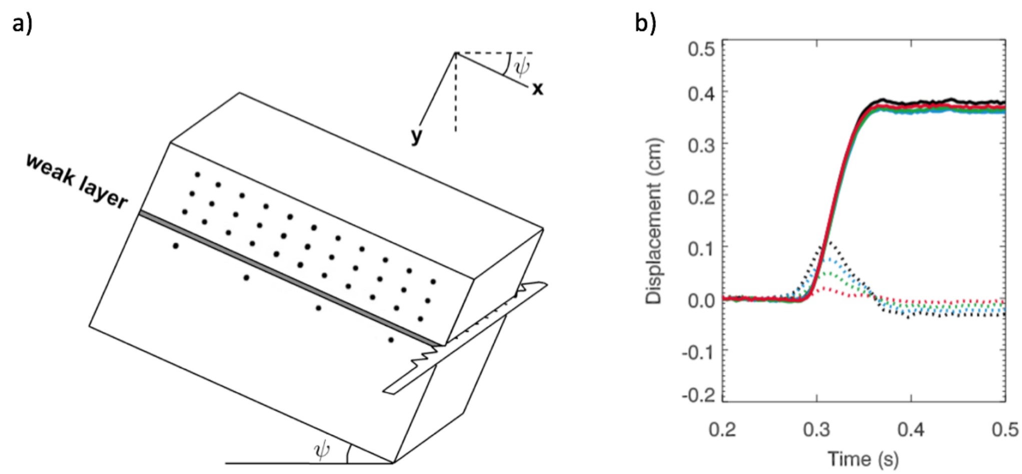

Figure 2.5: a) Propagation saw experiment, where the markers used for PIV are indicated. b) Slope-normal (solid lines) and slope-parallel (dashed lines) displacement of markers with the same slope-parallel position [Van Herwijnen et al., 2010].

While several authors provided evidence of a volumetric collapse during the failure of buried weak layers [Duclos, 1999; Jamieson and Schweizer, 2000], it has not been directly measured until relatively recently [Johnson et al., 2004] by seismic measurements. In recent years new insights into the interaction between the weak layer collapse and slab release has been been provided by combining PIV and the propagation saw test (PST), where a block of snow on a slope containing a weak layer is isolated and the weak layer is progressively destroyed with a saw until the overlying slab is released [Van Herwijnen et al., 2010; Gaume et al., 2015]. Normal collapse has been proven to have an important effect on the bending and fracture of the slab [Gaume et al., 2017b].

A number of authors that performed shear and mixed-mode loading experiments on snow samples with a weak layer [Fukuzawa and Narita, 1992; Joshi et al., 2006; Walters and Adams, 2012] reported a substantially lower shear strength in comparison with normal strength. Following a long-lasting debate in the snow science community whether it is the shear or compressive failure in the weak layer that triggers the response of a snow avalanche [Bucher, 1956; Perla and LaChapelle, 1970; Bradley et al., 1977; Schweizer, 1999], Joshi et al. [2006] believe that the relative difference between the shear and normal strength resolves this dilemma and proves that the failure in a weak layer is first induced in shear and subsequently leads to normal collapse of the layer and release of the snow avalanche. Walters and Adams [2012] attribute this difference between the shear and normal strength of the radiation recrystallized faceted weak layers to the quantitatively expressed microstructural anisotropy. This anisotropy is measured by the contact tensor [Shertzer and Adams, 2011], representing the probability of finding a bond oriented in the associated coordinate direction. Walters and Adams found a strong correlation between the magnitude of contact tensor coefficients and the strength of snow in the associated direction.

In the recent years, two experimental campaigns have gone beyond the qualitative observation of ultimate strength anisotropy of weak layers and systematically explored the ratio between shear and normal force at failure.

Chandel et al. [2014a] utilized the shear frame to explore failure envelopes of different snow types under mixed-mode loading in situ. Shear frame is a specially designed experimental tool for performing simple shear tests on a granular material by applying and measuring gradually increasing shear force at a constant normal load until the sample fails [Föhn et al., 1998; Jamieson and Johnston, 2001]. The experiments were performed in the brittle failure regime, with a typical duration $< 1s$. Chandel et al. outlined an important qualitative difference in the mechanical response of snow samples with weak layers with respect to homogeneous snow samples. The homogeneus samples of snow exhibited a near-linear (Mohr-Coulomb) positive relation between the shear and normal stress at failure, much like most other granular materials. The snow samples containing a weak layer of faceted snow however featured closed failure envelopes of elliptical shape in the domain of compressive normal stresses (Fig. 2.6.a).

Up to date, the most comprehensive experimental study of weak layers and their failure envelopes has been performed in laboratory conditions by Reiweger et al. [2010], who designed a shear testing apparatus where a sample of snow can be loaded with a combination of normal and shear stress by tilting. The failure of snow was observed with the help of force and displacement sensors, as well as particle image velocimetry (PIV) and acoustic emissions (EM). Experiments were performed at different loading rates, where brittle failure was observed for loading rates between 10 Pa s^{-1} and 444 Pa s^{-1}, resulting in test durations between 5 s and 30 s. The failure in loaded snow samples containing a persistent weak layer of either faceted crystal, depth hoar or buried surface hoar was analyzed and Reiweger et al. [2015] described the failure envelope by Mohr-Coulomb criterion with a cap model (Fig. 2.6.b). In experiments conducted with a 'fast' loading rate ($\approx$ 20 Pa s^{-1}) the fitted tensile strength was 0.4 kPa and the cohesion 0.17 kPa.

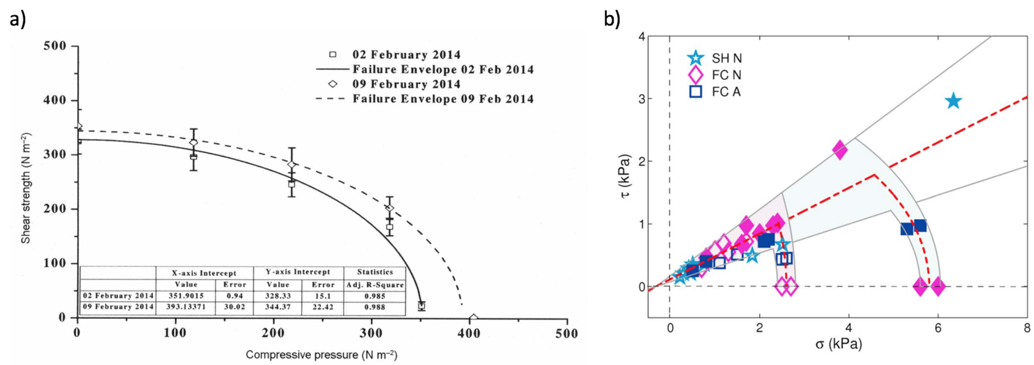

Figure 2.6: a)The eliptical failure envelope measured on snow samples featuring a weak layer of near-surface faceted particles (FCsf) by Chandel et al. [2014b]. b) The modified Mohr-Coulomb failure criterion was fitted to the results of shear experiments on snow [Reiweger et al., 2015].

While the failure envelopes obtained by Chandel et al. [2014a] and Reiweger et al. [2015] seem qualitatively different, it should be noted that Chandel et al. only performed mixed-mode loading tests in the positive normal stress domain, consistently with the shear frame limitations [Jamieson and Johnston, 2001]. Effectively only the cap of the failure envelope is observed, which is not entirely different from what was observed by Reiweger et al. The obvious difference is however the shift between the failure envelopes from the two experimental campaigns - while the failure envelopes obtained by Chandel et al. feature diminishing shear stresses in the entire positive normal stress domain, failure envelopes obtained by Reiweger et al. feature a Mohr-Coulomb phase which extends far into the positive normal stress domain, before the cap of the failure envelope takes place. This could be related to the difference in the experimental devices used to produce the results which could potentially induce different distributions of shear stresses within the snow samples. Additionally, a difference in the loading rates between the two experiments should be noted. Although Reiweger et al. claim the experiments were performed in the brittle regime, the typical test duration was roughly an order of magnitude longer than those performed by Chandel et al. and it is possible that grain sintering influenced the results.

Regardless of the differences between the results, obtained by the two experimental campaigns, all the tested snow samples with a weak layer feature closed failure envelopes. This closed shape, marking shear failure stresses that diminish to zero at sufficiently high normal stresses, is a consequence of the collapsible nature of weak layers and their ability to fail under pure normal stress.

2.2 Numerical modelling approaches

2.2.1 Constitutive mechanical behaviour of snow

Elastic modulus of snow

Young's modulus E of snow can be derived from finite element (FEM) calculations applied to X-ray derived microstructure. A mesh is applied the binary image of the ice phase of snow microstructure and by applying constitutive properties of ice, Young's modulus of snow can be calculated. The method is frequently used as it is reasonably simple, fast and accurate. Schneebeli [2004] calculated E for the same sample of snow during 4 stages of metamorphism. Effectively the four images of snow had the same density and different microstructure. As a consequence, the Young's modulus at density of 243 kg m^{-3} varied between 62 MPa and 226 MPa, underlining the effect of the microstructure on the stiffness of snow.

Srivastava et al. [2016] investigated the relationship between microstructure and anisotropic elastic properties of snow and concluded that along with the volume fraction, fabric descriptors are a key ingredient for the prediction of elastic properties of snow.

Köchle and Schneebeli [2014] applied the combination of FEM and X-ray microtomography to 32 samples of weak layers. Although they found clear correlation between Young's modulus E and density, this correlation is lower than for denser types of snow. The authors suggest that the lower correlation of E with lower densities is due to greater influence of microstructure. Wautier et al. [2015] however suggested that the scatter is linked to questionable size of the utilized boundary conditions and related need for larger snow samples in order to satisfy the representative elementary volume (REV) condition. Interestingly enough, Köchle and Schneebeli [2014] observed no dependence of E on snow type. As already mentioned, this points to the fact that crucial information for determining the mechanical properties of snow, namely the grain bonding system, is missing from the snow type description [Hagenmuller, 2014].

Wautier et al. [2015] applied the FEM approach and obtained Young's modulus for a large number of snow samples for varying snow types and densities. Summarizing the results of previous FEM studies, they proposed power laws to link the Young's and shear moduli to the density. The power law prediction captures the general trend of Young's modulus with respect to snow density, but the scatter around the power law suggests that microstructure is non-negligible (Fig. 2.7).

Recently, Gerling et al. [2017b] performed the first direct comparison of Young's modulus values, obtained by the combination of FEM and X-ray microtomography, to experimentally obtained values by means of P-wave propagation and reported good agreement.

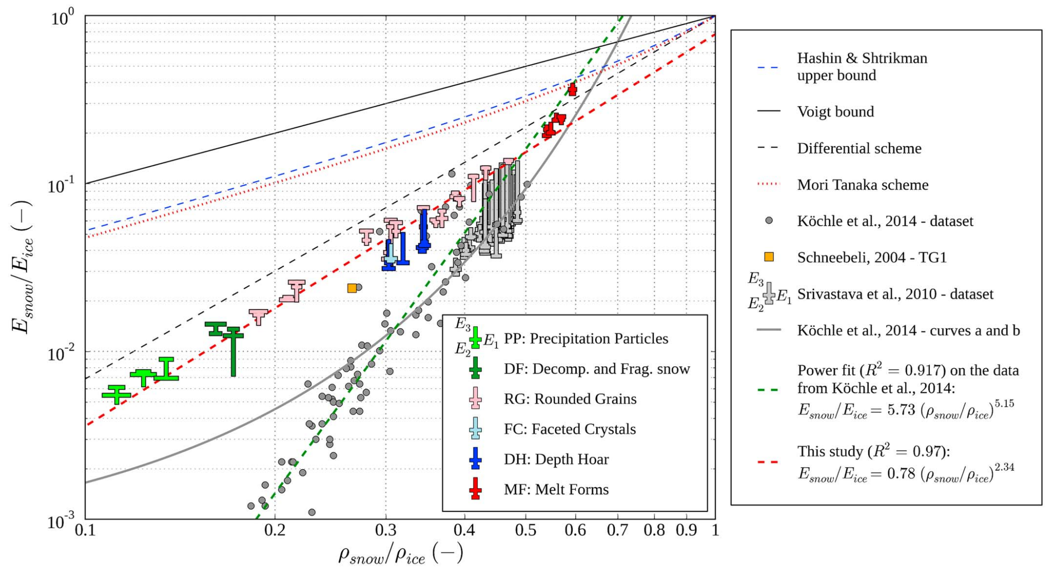

Figure 2.7: The Young's modulus of snow from different measurements as summarized by Wautier et al. [2015].

Large strain behaviour of snow

The FEM approach to modelling the snow response limits the domain of strains that can be explored as it doesn't allow grain rearrangement to be taken into account. There have been several attempts to overcome this limitation and explore large strain response of snow to loading using numerical modelling.

The problem of changing topology due to creation of new contacts is inherently resolved in the discrete element method (DEM). Johnson and Hopkins [2005] were the first authors to employ DEM to model the mechanical response of snow. They attempted to resolve the problem of snow creep densification process by modelling snow as an assembly of cylindrical grains with hemispherical ends, accounting for the anisotropy of the grains within the DEM framework. The model is temperature- and rate-dependent and enables the creation of new intergranular bonds dues to sintering. The authors noted that the dominant micromechanical deformation process at densities below 420 kg m^{-3} were particle rearrangements. However they were unable to run simulations at realistic particle stiffness values due to excessive calculation times.

While the DEM model of Johnson and Hopkins [2005] featured somewhat arbitrary choice of idealized snow grain shapes and a random spatial distribution of grains, Hagenmuller et al. [2015] conceived a DEM model of snow compression, where microstructure was directly accounted for. X-ray tomographical image of snow (Fig. 2.8.a) is taken as input information and the method is built on the assumption that a majority of damage under mechanical loading will take place in the neck regions of the snow matrix, where individual grains are sintered. The X-ray image of snow is therefore segmented into pore space and a continuous ice matrix [Hagenmuller et al., 2013]. The ice structure is then segmented into individual grains by detecting potential weak points based on local geometrical criteria [Hagenmuller et al., 2014b] (Fig. 2.8.b). Authors explored the domain of large deformations and relatively high compaction rates, where snow deformation is believed to be dominated by grain rearrangement [Alley, 1987; Arnaud et al., 1998; Johnson and Hopkins, 2005], allowing them to model individual snow grains as unbreakable. The shape of the grains is approximated with a large number of smaller spherical discrete elements (DEs), distributed along the grain boundaries and connected into a rigid clump (Fig. 2.8.c). These clumps that represent snow grains, are then connected with the neighbouring grains by cohesive bonds at the points, identified as grain boundaries by the segmentation algorithm. The developed model is capable of reproducing the large strain behaviour of snow, involving gradual snow matrix collapse and rearrangement of grains. Hagenmuller et al. used the model to perform confined compression simulations on images of different snow samples, including weak layers. Although the simulations showed that the compressive behaviour of snow is mainly controlled by density of the samples, a non-negligible effect of the microstructure has been demonstrated.

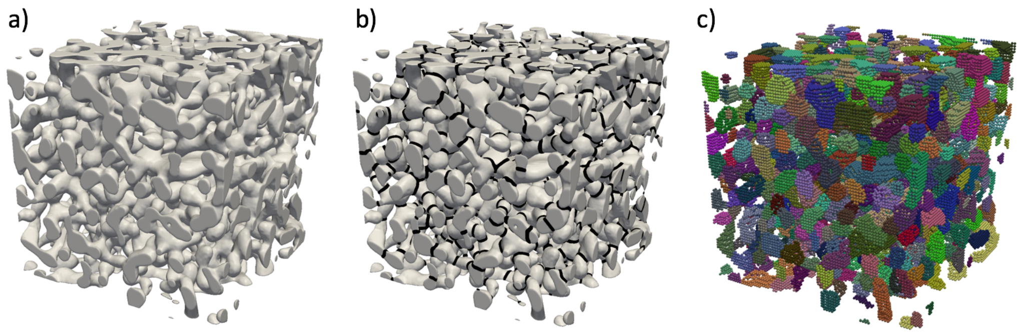

Figure 2.8: Granular description of the ice matrix: a) binary image, b) individual grains separated by grain bonds (in black) and c) grains represented by sphere-clump approximations [Hagenmuller, 2014].

The approach employed by Hagenmuller et al. relied on the precise microstructure of the snow samples to investigate the mechanical response of weak layers, which resulted in a considerable numerical cost. Gaume et al. [2017a] have recently outlined an alternative way of accounting for the microstructure. They performed DEM simulations of confined snow compression with initial configurations drawn from Baxter's sticky hard sphere (SHS) ensemble [Watts et al., 1971]. The two most prominent microstructural properties of granular materials are particle volume and coordination number [Gaume et al., 2017a]. While these two parameters are interrelated for dense, non-cohesive granular assemblies, their influences can decouple in the case of cohesive assemblies such as snow, that can exist in a stable configuration at very small volume fractions. The authors therefore employed the SHS model to generate assemblies of spherical DEs with identical volume fractions but different coordination numbers, offering two independent controls on the contact density as the key quantity. Confined compression simulations were carried out on these initial states which resulted in mechanical responses which can be generalized in the following phases: (i) a quasi-elastic stress build-up, where almost no bond-breaking takes place: (ii) a plastic consolidation regime and (iii) a packing regime corresponding to jamming transition. The authors focused their observations on the initial phases of the simulations and reported a power law dependency of the Young's modulus and compressive failure strength on the contact density of the initial configuration. The plasticity index, characterizing the plastic consolidation curve after failure, was however found to be independent of the initial conditions.

2.2.2 Slab-weak layer system response

Gaume et al. [2015, 2017b] have attempted to build a simplified 2D model of a slab-weak layer system in order to explore the influence of weak layer failure and mechanical properties of the slab on fracture arrest propensity. The method enabled them to observe crack propagation in the weak layer as well as crack formation in the overlying slab. The method is based on using the discrete element method (DEM) in order to construct an idealized geometric constellation of particles, mimicking the properties of a weak snow layer. Circular DEs are distributed in a triangular zig-zag pattern and bounded by cohesion (Fig. 2.9(b)). The pattern resembles depth hoar crystal shapes and results in a vertical collapse under a sufficiently large shear or normal loading. This weak layer is underlying a slab layer, represented by a dense grid of cohesively bounded circular discrete elements (Fig. 2.9(a)). Gravity is applied under a certain angle in order to simulate the slope angle. Propagation saw test (PST) is simulated by imposing the progressive failure of the weak layer. At a certain critical crack length, the crack spontaneously propagates. The loss of support in the weak layer results in tensile, shear and bending forces on the slab which in term lead to a crown crack in the slab, signifying the onset on an avalanche. Gaume et al. showed that the crack propagation distance and speed obtained by a properly calibrated model are in good agreement with measurements, obtained by PST experiments. The numerical model enabled them to perform a parametric analysis and show that crack propagation speed increases with Young's modulus of the slab, slab depth, slab density and slope angle, but decreases with weak layer strength. The crack propagation distance on the other hand decreases with increasing Young's modulus of the slab, slab density and weak layer thickness, but increases with increasing slab tensile strength, slab depth, weak layer strength and slope angle. Besides the fact that the study has shown the crack propagation to depend on the weak layer strength, it should also be noted that the results of the study inherently depend on the post-failure response of the weak layer.

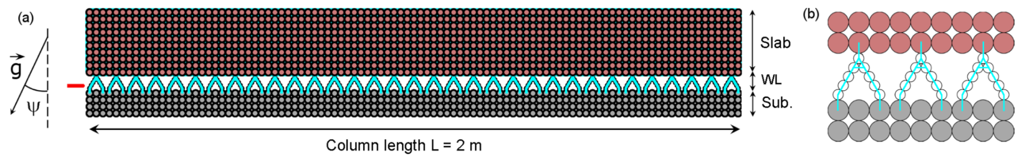

Figure 2.9: The DEM approach to model propagation saw test, employed by Gaume et al. [2015]. a) The weak layer, consisting of circular elements distributed in a triangular manner and an overlying slab layer. b) Cohesive bonds between DEs in the modelled weak layer.

2.3 Scientific questions and approach

Dry snow slab avalanches have been shown to be triggered by failure in a weak layer of the snow cover, underlying a cohesive slab. On a slope, this layer of snow is loaded in combined shear and compression, the so-called mixed-mode loading, by the weight of the overlying snow and potential additional perturbations (skiers, animals etc.). If the strength of the weak layer is locally exceeded, a localized failure occurs. Once the initial failure reaches a critical size, it starts propagating along the slope, gradually diminishing the support to the overlying slab. Consequently, the tensile and bending stresses within the slab increase, which can eventually lead to a slab rupture along a crown fracture, causing the release of an avalanche. A thorough knowledge of the mechanical response of snow to mixed-mode loading is thus recognized as the key ingredient for modelling and ultimately predicting snow avalanches. However, given the present state of knowledge, our understanding of snow response to mixed-mode loading, particularly in failure and post-failure, remains limited. Hence, investigation of failure and post-failure response of snow under mixed-mode loading is identified as the main objective of this thesis.

Failure of homogeneous samples of 'strong' snow has been observed to follow a Mohr-Coulomb criterion [McClung, 1977], where the slope of the failure line seems to be strongly influenced by snow density [Sommerfeld, 1973] as well as other microstructural attributes [Narita, 1984; Mellor, 1974; Shapiro et al., 1997]. Failure of weak layers on the other hand seems to follow closed failure envelopes [Chandel et al., 2014a; Reiweger et al., 2015]. Whether the failure envelopes of different weak layers are qualitatively similar and how these failure envelopes relate to snow microstructure is not clear due to very scarce experimental data. It is however clear that the closed shape of failure envelopes is related to normal failure and the well documented collapse of weak layers [Johnson et al., 2004; Van Herwijnen et al., 2010], which has been proven to have an important effect on the bending and fracture of the slab [Gaume et al., 2017b]. The conditions under which a collapse occurs, the relation between shear failure and collapse and the softening curve of homogeneous samples as well as weak layers however remain largely unexplored. Gaume et al. [2018] recently underlined the importance of systematic observations of failure and post-failure response of snow to mechanical loading for the development of a constitutive law of snow that could be used for large scale simulations of snow avalanche release.

The extremely low strength of snow, particularly if it includes a weak layer, and its sensitivity to environmental conditions render systematic experimental exploration difficult and complicate observation at the microscopic level. The ever-increasing computing power, development of numerical computational tools and modern measurement systems have on the other hand resulted in development of alternative, numerical approaches for obtaining mechanical response of snow. The exact microstructure of snow can now be obtained by X-ray tomography, and different approaches are being developed, which attempt to predict the mechanical response of snow directly from the microstructure [Theile et al., 2011; Hagenmuller et al., 2015; Gaume et al., 2017a]. In the scope of this thesis, we will adopt the latter approach and extract the mechanical response of snow from numerical simulations, thus avoiding the difficulties related to experimental exploration.

The focus of this thesis can be summarized in the following scientific questions:

- How to accurately model the response of snow to mixed-mode loading? The scarce experimental data prevents us from developing a constitutive model based on macroscopic observations. An alternative approach must hence be adopted, where the macroscopic mechanical response of snow is calculated from the interactions of snow grains, constituting the snow matrix which is now accessible by X-ray microtomography. Via the multi-scale approach, complexity of the macroscopic response can be captured as an up-scaling effect of the changing microstructure topology rather than complex constitutive relations.

- What is the large-strain macroscopic response of snow to mixed-mode loading? Focus will be on failure and immediate post-failure response as well as identification of the main deformational mechanisms governing different stages of the shear response of snow.

- Which are the micromechanical mechanisms leading to the failure of snow under mixed-mode loading? A deeper understanding of the process of failure will be sought as well as micromechanical descriptors that anticipate snow failure.

- How does microstructure influence failure and post-failure response of snow under mixed-mode loading? The simulated response of different snow samples, including weak layers, will be compared in order to investigate the existence of qualitative differences in their mechanical response.

2.4 Structure of the thesis

This thesis is a collection of articles which are either already published, submitted or under preparation, with the exception of chapters 3 and 5. Consequently each chapter can be read read independently, but due to self-contained content of each chapter, the manuscript inevitably contains some repetitions. The thesis is organized as follows:

Chapter 3: Discrete element method was identified as the most appropriate numerical tool for simulating large strain response of snow under mixed-mode loading. The general concept of the numerical method is thus presented and the computing procedure of the open-source solver YADE, which is to be used for performing simulations, is presented. Collision detection is briefly reviewed, while more emphasis is given on the contact force evaluation and motion integration as the understanding of the latter two steps is considered important for the subsequent numerical modelling. Finally some considerations regarding computational stability and numerical cost are discussed.

Chapter 4: A numerical model of snow was developed that enables large-strain simulation of snow response to mechanical loading. The model takes X-ray microtomographical images of snow as input information and builds on the assumption that snow behaves as a cohesive granular material. Since the model is designed to explore the failure and immediate post-failure response of snow, which is governed by inter-granular interactions, the individual grains can be modelled as unbreakable entities, connected into the snow matrix by cohesion with the neighbouring grains. This allows us to identify individual grains, by applying a segmentation algorithm to the binary image of snow matrix, and use DEM framework to resolve the interactions between the grains. An original method for approximating arbitrary grain shapes by a collection of spheres is developed, which allows us to directly account for grain shapes in DEM at a reasonable computational cost. An extensive sensitivity analysis is performed in order to assess the influence of grain representation precision on the geometrical descriptors of approximated grains. These results are then put into perspective by performing oedometric compression simulations of a snow sample, approximated with different levels of precision. The introduced geometrical descriptors have been shown to correlate strongly with the precision of mechanical simulations, suggesting they can be used as a tool to determine the necessary level or grain approximation precision that will result in a certain level of mechanical simulation precision.

This work has been published as *Mede, T., G. Chambon, P. Hagenmuller, and F. Nicot (2018), A medial axis based method for irregular grain shape representation in dem simulations, Granular Matter, 20(1), 16.*

Chapter 5: Before the developed model of snow can be applied to mixed-mode loading scenario, simulation parameter values that would insure the validity of simulations need to be determined. A meticulous procedure was applied in order to determine the optimal values for stiffness and density of the grains, shearing velocity, loading rate and timestep of the simulation. A sensitivity analysis of the mechanical simulation results with respect to grain approximation precision was repeated for mixed-mode loading. The results of the sensitivity analysis were consistent with those from the oedometric compression: the same level of approximation precision was identified as the optimal and a similar correlation between geometric descriptors and mechanical simulation precision was observed.

Chapter 6: Mixed-mode loading programs were applied to three samples of snow, one of which was a persistent weak layer sample. Macroscopic response to shearing was observed under different values of normal stress and qualitatively consistent behaviour was observed for all three tested samples. Three distinct modes of failure were observed with respect to the level of applied normal stress. If the normal stress is sufficiently high, the failure is marked by a rapid volumetric collapse of the sample, that was shown to be a dynamic event, which, once started, evolves independently of shearing. Samples feature closed failure envelopes, which deviate from the Mohr-Coulomb criterion at high normal stresses and diminish to zero as a consequence of their collapsible nature.

This work is under minor revision for publication as *Mede, T., G. Chambon, P. Hagenmuller, and F. Nicot (n.d.), Snow failure modes under mixed loading, Geophisical Research Letters.*

Chapter 7: Simulated failure of snow under mixed-mode loading was analysed on the microscopic level in order to explore the mechanism of the volumetric collapse. Force chain network was identified in a loaded snow sample in order to study the response of the load carrying fraction of the material. While force chains were shown to align with the principal stress angle, their average lifespans were observed to reflect the stability of the snow sample. Pronounced force chain buckling was observed to anticipate the volumetric sample collapse. Furthermore, by analysing the contacts between the force chain members and the surrounding grains, it was shown that in the loading scenarios that lead to a volumetric collapse of the sample, a considerable fraction of these contacts are very close to failing, when the sample becomes unstable. The mechanism of volumetric collapse is thus described by pronounced force chain buckling, which is made possible by the failure of the grain contacts that insure the lateral support to the force chains.

This work is under preparation for publication in the International Journal of Solids and Structures.

Chapter 8: The last chapter summarizes the main results obtained during the thesis and opens perspectives for future research.

Chapter 3

Discrete element method

Abstract Basic notions of discrete element method (DEM) are established and a general computational scheme is presented. Open-source DEM solver YADE is introduced and its specific computational procedure is explained. Certain aspects of the computational procedure are crucial for the understanding of the work done in this thesis and are therefore thoroughly described in this chapter. Other aspects are less important for understanding of the undertaken work and are therefore only briefly introduced. General aspects of collision detection are hence presented, a detailed account of contact force calculation is described and the basic notions of motion integration are reviewed. Additionally, some computational aspects are discussed.

Contents

Discrete element method (DEM) is a family of numerical methods for motion computation of a large number of particles. It is closely related to the more known molecular dynamics method, but also accounts for rotational degrees of freedom of individual particles and complex particle shapes (such as polyhedra). The method relies on a explicit integration scheme, where the system state at the following timestep is calculated directly from the state at the given timestep. The solution at each timestep consists of the following calculations:

- **Collision detection:** based on the position and shapes of all the particles, contacts between individual particles are identified.
- **Contact force evaluation:** based on the kinematic variables of contact and material properties, a contact force is calculated for each pair of contacting particles according to the defined constitutive law.
- **Motion integration:** the contact force is used to calculate the position of each individual particle in the next timestep.

YADE [Šmilauer et al., 2010], an open-source DEM solver developed at the university Grenoble-Alpes, is used to perform the simulations presented in this manuscript. In the following section, YADE computing methodology is briefly explained.

3.1 YADE computing procedure

3.1.1 Collision detection

Exact collision computation of a set of particles is a numerically expensive procedure, particularly if particles are of complex shapes. Collision detection is therefore computed in two steps:

- **Fast collision detection:** YADE utilizes the Sweep and Prune algorithm, where a rectangular axis-aligned bounding box is assigned to each particle and overlap between these bounding boxes is sought.
- **Exact collision detection:** Having filtered out the impossible collisions in the first step, a second more expensive collision detection step is run on the remaining possible collisions. Particular shapes of particles have to be taken into consideration.

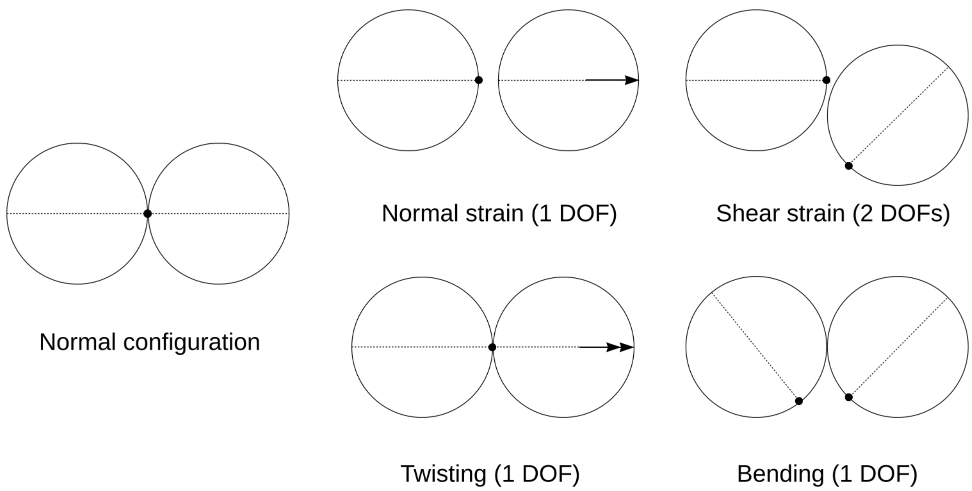

Figure 3.1: Schematical representation of the four different types of strain [Šmilauer et al., 2010].

3.1.2 Strain evaluation

In general, a mutual configuration of two particles with 6 degrees of freedom each, also has 6 degrees of freedom. Kinematics of grain contact result in 5 different types of strain[1]. Normal strain is caused by the difference in the linear velocity of the particles along the interaction axis $\vec{n}$. The shear strain originates from the difference in the linear particle velocities tangential to the contact plane and the sum of the angular velocities of both particles $\vec{\omega}_1 + \vec{\omega}_2$, perpendicular to the interaction axis $\vec{n}$. Twisting is caused by the part of $\vec{\omega}_1 - \vec{\omega}_2$ parallel to $\vec{n}$ and bending by the part of $\vec{\omega}_1 - \vec{\omega}_2$ perpendicular to $\vec{n}$.

Normal strain

When two spheres with centers $\vec{C}_1$ and $\vec{C}_2$ and radii r_1 and r_2 come into contact (image 3.1) the following quantities are calculated:

[1] Yade terminology was adopted here. Forces applied to discrete elements are sometimes referred to as stresses and displacements as strains.

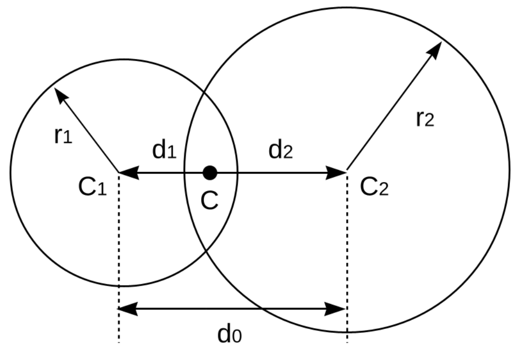

Figure 3.2: Two spheres in the initial contact position. For the sake of generality, spheres on the image are already overlapping in the initial position (which can be the case in the beginning of the simulation) [Šmilauer et al., 2010].

$$d_0 = \|\vec{C}_1 - \vec{C}_2\| \tag{3.1}$$

$$d_1 = r_1 + \frac{d_0 - r_1 - r_2}{2} \tag{3.2}$$

$$d_2 = d_0 - d_1, \tag{3.3}$$

where $d_0 = d_1 + d_2$ is the reference distance. All of these quantities are calculated only once, when the spheres come into contact, and serve as reference values. The reference distance d_0 is used to convert absolute displacements into relative strain and also as the neutral distance, where the spheres are neither in tension nor in compression.

As spheres undergo motion, the following variables are updated:

$$\vec{n} = \frac{\vec{C}_2^\circ - \vec{C}_1^\circ}{\|\vec{C}_2^\circ - \vec{C}_1^\circ\|} \equiv \widehat{\vec{C}_2^\circ - \vec{C}_1^\circ} \tag{3.4}$$

$$\vec{C}^\circ = \vec{C}_1^\circ + \left(d_1 - \frac{d_0 - \|\vec{C}_2^\circ - \vec{C}_1^\circ\|}{2}\right)\vec{n} \tag{3.5}$$

The contact point $\vec{C}^\circ$ is always in the middle of the spheres' overlap zone (in case the overlap is negative, this is in the middle of the empty space between the spheres). Contact plane is always perpendicular to the contact

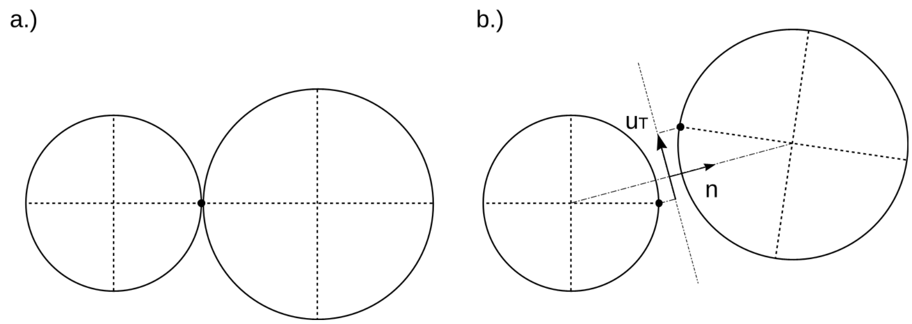

Figure 3.3: Two spheres in a.) initial contact position and b.) shear strain [Šmilauer et al., 2010].

plane normal $\vec{n}$ and passes through the point $\vec{C}^{\circ}$. Penetration depth u_N and normal strain ε_N can now be defined as:

$$u_N = \|\vec{C}_2^{\circ} - \vec{C}_1^{\circ}\| - d_0 \tag{3.6}$$

$$\varepsilon_N = \frac{u_N}{d_0} = \frac{\|\vec{C}_2^{\circ} - \vec{C}_1^{\circ}\|}{d_0} - 1. \tag{3.7}$$

Shear strain

Yade implements a classical incremental algorithm to calculate the shear strain. Shear displacement is updated every step through the calculation of the relative velocity $\vec{v}_{12}$ of the two spheres in contact. Relative velocity can be calculated as:

$$\vec{v}_{12} = \vec{v}_2 - \vec{v}_1 + \vec{\omega}_2 \times (\vec{C}_2^{\circ} - \vec{C}^{\circ}) - \vec{\omega}_1 \times (\vec{C}_1^{\circ} - \vec{C}^{\circ}). \tag{3.8}$$

The above relation for the relative velocity must be consistent and needs to remain zero in case of reference frame rotation or if the particles arbitrarily move through space without changing their mutual position. For the equation 3.8, the objectivity can be demonstrated in the following manner [**?**]: the angular velocity $\vec{\omega}_0 = \vec{\omega}_0^n + \vec{\omega}_0^t$ has the tangential in-plane component:

$$\vec{\omega}_0^t = \frac{\vec{n} \times (\vec{v}_2 - \vec{v}_1)}{\|\vec{C}_2^{\circ} - \vec{C}^{\circ}\| + \|\vec{C}_1^{\circ} - \vec{C}^{\circ}\|}, \tag{3.9}$$

which is related to the relative velocity $\vec{v}_{12}$, while the normal component is not. Inserting $\vec{\omega}_1 = \vec{\omega}_2 = \vec{\omega_0^t}$ results in zero relative velocity and thus proves the objectivity of the above relation.
However, relative velocity, based on the equation 3.8 can result in numerical granular ratcheting. Granular ratcheting is a well known effect in granular materials under cyclic loading, where a certain amount of permanent deformation is accumulated each cycle [?]. One can imagine numerical ratcheting resulting from the equations 3.8 and 3.13 by considering the following elastic cycle between two grains: keeping the position of the grain 1 fixed, grain 2 translates in the normal direction toward grain 1 for the distance $\dot{\text{x}}$, rotates for the angle α translates for the distance $-\dot{\text{x}}$ in the normal direction away form grain 1 (back into the initial position) and rotates for the angle $-\alpha$ (back into the initial orientation). From the equations 3.8, 3.13, 3.25, 3.12 and 3.32, as a consequence of shear force being proportional to the diminished radius d_2, the given scenario results in a finite force, which is in complete contradiction with the elastic nature of the problem. This force naturally produces an inconsistent loss of energy. Since DEM simulations tend to generate oscillations around the equilibrium positions, numerical granular ratcheting problem can have a significant impact on the evolution of packings and produce a slow creep. In order to avoid numerical ratcheting, an alternative way to calculate the relative shear velocity is coded into Yade. Should the option to avoid the granular ratcheting be chosen, the following procedure is utilized to calculate the relative shear velocity:

$$\vec{v}_{12} = \alpha(\vec{v}_2 - \vec{v}_1) + \vec{\omega}_2 \times (r_2\vec{n}_2) - \vec{\omega}_1 \times (r_1\vec{n}_1), \tag{3.10}$$

where

$$\alpha = \frac{r_1 + r_2}{r_1 + r_2 - u_N}. \tag{3.11}$$

If the part of the shear velocity is denoted shear relative velocity v_{12S}, it can be calculated from equation 3.8 or 3.10 by applying:

$$v_{12S} = \vec{v}_{12S} \cdot \vec{n}. \tag{3.12}$$

The shear increment Δu_T is then:

$$\Delta u_T = v_{12S}\Delta t. \tag{3.13}$$

Twisting

In case the incremental formulation is not used (default), the relative rotation $\vec{\varphi}_{rTW}$ due to twisting is obtained directly in an non-incremental way from the difference between the current and the initial position of the spheres. Since DE orientations is Yade are are represented with quaternions, the $\mathbf{\Delta}$ quaternion, which represents the difference in rotation between the first and the second sphere, can be obtained by applying:

$$\mathbf{\Delta} = (\boldsymbol{O}_1\overline{\boldsymbol{O}}_1^{init})(\boldsymbol{O}_2^{init}\overline{\boldsymbol{O}}_2), \tag{3.14}$$

where $\boldsymbol{O}_1$, $\overline{\boldsymbol{O}}_1^{init}$, $\boldsymbol{O}_2^{init}$ and $\overline{\boldsymbol{O}}_2$ are the current orientation quaternion of sphere 1, conjugated orientation quaternion of sphere 1 in the initial contact position, initial orientation quaternion of sphere 2 and conjugated current orientation quaternion of sphere 2 in the initial contact position respectively. In the first part of the equation, the current and the conjugated initial orientation are multiplied, which results in a quaternion, describing the rotation of sphere one from the initial orientation into the current one. The second part of the equation gives this value for the second sphere, but due to shifted order, in the inverse direction. Multiplying the two parts results in the $\mathbf{\Delta}$ quaternion, describing the difference in rotation of the two spheres through the duration of the contact.

The $\mathbf{\Delta}$ quaternion consists of the rotation axis $\vec{a} = (a_1, a_2, a_3)$ and the rotation angle δ around this axis:

$$\mathbf{\Delta} = (\delta, a_1, a_2, a_3), \tag{3.15}$$

which can be utilized to obtain the twisting angle between the two spheres:

$$\vec{\varphi}_{rTW} = \delta(\vec{a}_n \cdot \vec{n}), \tag{3.16}$$

where $\vec{a}_n$ is the normalized rotation axis:

$$\vec{a}_n = \frac{\vec{a}}{\|\vec{a}\|}. \tag{3.17}$$

In case the incremental formulation is used, the relative angular twisting velocity $\vec{\omega}_{rTW}$ is first calculated from the relative angular velocity $\vec{\omega}_r$ between the two spheres:

$$\vec{\omega}_{rTW} = (\vec{\omega}_r \cdot \vec{n})\vec{n}, \tag{3.18}$$

where $\vec{n}$ is the normal of the contact between the two spheres. Relative twisting rotation increment $\Delta\vec{\varphi}_{rTW}$ can then be evaluated using:

$$\Delta\vec{\varphi}_{rTW} = \vec{\omega}_{rTW}\Delta t. \tag{3.19}$$

Bending

In case the incremental formulation is not used (default), the relative rotation $\vec{\varphi}_{rB}$ due to bending is obtained directly in an non-incremental way from the difference between the current and the initial position of the spheres. With respect to equations 3.14, 3.15, 3.28, 3.16, the bending vector is defined as the difference between the relative rotation between spheres in contact and the twisting vector:

$$\vec{\varphi}_{rB} = \delta\vec{a}_n - \vec{\varphi}_{rTW}. \tag{3.20}$$

In case the incremental formulation is used, the relative angular bending velocity $\vec{\omega}_{rB}$ is first calculated form the relative angular velocity $\vec{\omega}_r$ between the two spheres:

$$\vec{\omega}_{rB} = \vec{\omega}_r - (\vec{\omega}_r \cdot \vec{n})\vec{n}, \tag{3.21}$$

where $\vec{n}$ is the normal of the contact between the two spheres. Relative rotation increment $\Delta\vec{\varphi}_{rB}$ due to bending behavior can then be evaluated using:

$$\Delta\vec{\varphi}_{rB} = \vec{\omega}_{rB}\Delta t \tag{3.22}$$

3.1.3 Contact force evaluation

Contact force between two particles is calculated from kinematic variables of interaction i.e. contact strain and material properties, according to relations defined by the contact law. Numerous predefined contact laws are available in YADE, but only the cohesive-frictional contact law[2] will be presented in this section, since it is the contact law that is later applied to the DEM model of snow. The cohesive contact law insures an elastic-brittle contact

[2]In YADE, this contact law is applied by choosing the *CohFrictPhys* setting for the physical properties of interaction.

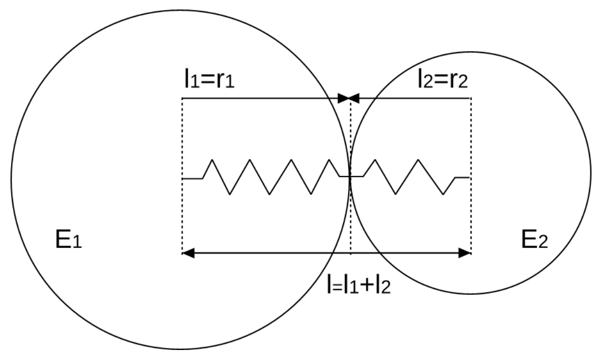

Figure 3.5: Normal stiffness between two spherical discrete elements in contact [Šmilauer et al., 2010].

force under normal tension and an elastic-brittle contact force with residual friction under shear loading.

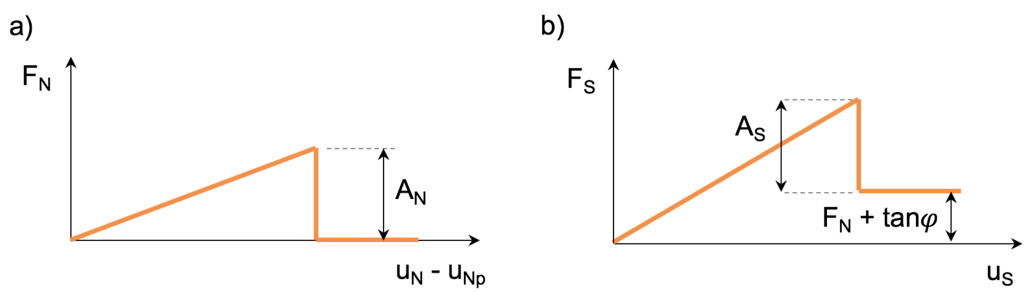

Figure 3.4: a) Normal contact force dependence on normal particle displacement. b.) Shear contact force dependence on shear particle displacement.

Basic DEM interaction is defined by two stiffnesses: normal stiffness K_N and shear stiffness K_T. While the normal stiffness is usually governed by the Young's modulus E of the material, the shear stiffness is calculated as a fraction of the normal stiffness. The macroscopic Poisson ratio ν is determined as the ratio K_T/K_N.

The normal stiffness of a contact in Yade is calculated in the following manner: if the initial distance between the two spheres in contact is denoted as $l = l_1+l_2$, where l_i is the radius of the sphere i, than the change of distance $\Delta l = \Delta l_1+\Delta l_2$ is distributed between the two spheres proportionally to their compliances. Displacement change Δl_i generates a normal force $F_i = K_i \Delta l_i$, where the stiffness K_i is proportional to the Young's modulus E_i and some distance $\tilde{l}_i$ which is proportional to r_i [3].

$$
\begin{aligned}
\Delta l &= \Delta l_1 + \Delta l_2 \\
K_i &= E_i \tilde{l}_i \\
K_N \Delta l &= F = F_1 = F_2 \\
K_N(\Delta l_1 + \Delta l_2) &= F \\
K_N(\frac{F}{K_1} + \frac{F}{K_2}) &= F \\
K_1^{-1} + K_2^{-1} &= K_N \\
K_N &= \frac{K_1 K_2}{K_1 + K_2} && (3.23) \\
K_N &= \frac{E_1 \tilde{l}_1 E_2 \tilde{l}_2}{E_1 \tilde{l}_1 + E_2 \tilde{l}_2} && (3.24)
\end{aligned}
$$

The shear stiffness K_T can then be calculated using the Poisson ratio:

$$K_T = \nu K_N. \tag{3.25}$$

Based on contact geometry and stiffnesses, forces between two particles in cohesive frictional contact can now be calculated.

Normal force

The normal force is calculated by applying:

$$F_N = K_N(u_N - u_{Np}), \tag{3.26}$$

where u_N is the penetration depth and u_{NP} the plastic penetration depth, which will be further defined in the following.

If the contact is modeled as fragile, the cohesion between two particles will exist as long as the tensile normal force F_N remains below the value of the normal adhesion A_N:

[3] Although there are also material models in Yade that use a different definition, for the cohesive frictional material, the most common definition $\tilde{l}_i = 2r_i$ is used.

$$F_{Nmax} = A_N \tag{3.27}$$

, where the normal adhesion is the normal cohesion C_N of the weaker particle in contact, multiplied by the square area around the smaller sphere in contact:

$$A_N = min(C_{N1}, C_{N2})min(r_1, r_2)^2. \tag{3.28}$$

If the normal tensile force exceeds the normal adhesion, the interaction between the two particles is erased and the contact force is set to zero.

If, however, the contact is modeled as plastic, then the two particles enter a plastic regime after the tensile normal force exceeds the normal adhesion. The tensile normal force is set to the value of normal adhesion:

$$F_N = -A_N \tag{3.29}$$

and the penetration depth u_N is now monitored. The penetration depth can be calculated by $u_N = (r_1+r_2) - \|\vec{u_1} - \vec{u_2}\|$, where r_i and $\vec{u_i}$ are the radius the position of the center of the sphere i. It is clear that in the case under observation , the penetration depth is negative. The plastic penetration depth can be calculated by applying:

$$u_{Np} = u_N + \frac{A_N}{K_N}. \tag{3.30}$$

The two particles will remain in cohesive contact until the plastic penetration depth doesn't exceed the maximal plastic penetration depth value u_{Npmax}:

$$u_{Np} \geq u_{Npmax}. \tag{3.31}$$

In case plastic penetration depth exceeds the maximum value, the interaction in erased and the contact force is set to zero.

Shear force

The trial shear force F_{TS} is calculated as a sum of incremental shear forces F_{Si} and the contribution of the current incremental shear displacement $\Delta\vec{u}_S$ under the assumption that the shear deformation is elastic:

$$\vec{F}_{TS(i+1)} = \vec{F}_{S(i)} - K_S \Delta \vec{u}_{S(i+1)}. \tag{3.32}$$

The maximum shear force F_{Smax} is defined as the sum of shear adhesion

$$A_S = min(C_{S1}, C_{S2}) min(r_1, r_2)^2 \tag{3.33}$$

and the frictional force:

$$F_{Smax} = A_S + F_N tan\varphi, \tag{3.34}$$

unless the *cohesion disables friction* option is used. In this case the maximum shear force is equal to shear adhesion. This option is ignored in case the shear adhesion is set to zero.

If the trial shear force does not exceed the maximum shear force, the trial shear force is adopted as the solution of the shear force:

$$\vec{F}_S = \vec{F}_{TS}. \tag{3.35}$$

If the maximum shear force is exceeded, the contact enters the plastic scenario. A perfect plasticity is assumed and the shear force is at to the value of maximum shear force:

$$\vec{F}_S = F_{Smax} \frac{\vec{F}_S}{\|F_S\|}. \tag{3.36}$$

The energy dissipation is calculated as the dot product of the plastic displacement $\vec{u}_{Sp}$ and the shear force:

$$E_D = \vec{u}_{Sp} \cdot \vec{F}_S = \frac{1}{K_S} (\vec{F}_{TS} - \vec{F}_S) \cdot \vec{F}_S. \tag{3.37}$$

Shear creep can also be followed. If this option is activated, the shear force decreases with time according to:

$$F_S = F_S - K_S \frac{F_S}{\nu_{creep}} \Delta t \tag{3.38}$$

and ν_{creep} is the creep viscosity.

Twisting moment

The twisting moment will be active only until cohesion is broken unless the option *always use moment law* is used - in this case the twisting moment will be applied even if the cohesion is already broken. The *momentRotationLaw* option also needs to be activated in the material definition in order to activate the moment laws.

In case the incremental formulation is not used (default), the relative rotation $\vec{\varphi}_{rTW}$ due to twisting is obtained directly in an non-incremental way from the difference between the current and the initial position of the spheres (3.16) and the twisting moment is calculated by applying:

$$\vec{M}_{TW} = \vec{\varphi}_{rTW} K_{TW}. \tag{3.39}$$

Twist creep can also be activated with the non-incremental formulation. The twisting creeped angle is calculated in the following manner:

$$\varphi_{TW\,creep} = \varphi_{TW} \left(1 - \frac{\Delta t}{\tau} \right), \tag{3.40}$$

where:

$$\tau = \nu_{creep} \frac{min(r_1, r_2)^2}{16} \tag{3.41}$$

and ν_{creep} is the creep viscosity.

In case the incremental formulation is used, the twisting moment increment $\Delta\vec{M}_{TW}$ is defined as the product of the relative twisting rotation increment $\Delta\vec{\varphi}_{rTW}$ (3.19) and the twisting stiffness K_{TW}:

$$\Delta\vec{M}_{TW} = \Delta\vec{\varphi}_{rTW} K_{TW}. \tag{3.42}$$

Finally, the total twisting moment $\vec{M}_{TW}$ can be calculated by summing the twisting moment from the previous step and the the twisting moment increment:

$$\vec{M}_{TW\,(i)} = \vec{M}_{TW\,(i-1)} + \Delta\vec{M}_{TW}. \tag{3.43}$$

If plasticity is used (if the parameter *etaRoll* in the material definition is set to be greater than zero), a limiting twisting moment is set and a perfect plasticity scenario is followed upon the point where the elastic twisting moment exceeds the limiting twisting moment. If the elastic twisting moment from the equation 3.39 (or 3.43 in the case of incremental formulation) exceeds the maximal twisting moment $M_{TW\,max}$, the value of the twisting moment is set to the value of the maximal twisting moment:

$$\vec{M}_{TW} = \frac{\vec{M}_{TW}}{\|\vec{M}_T W\|} M_{TW\,max}. \tag{3.44}$$

Bending moment

Like the twisting moment, the bending moment will be active only until cohesion is broken unless the option *always use moment law* is used - in this case the bending moment will be applied even if the cohesion is already broken. The *momentRotationLaw* option also needs to be activated in the material definition in order to activate the moment laws.

In case the incremental formulation is not used (default), the relative rotation $\vec{\varphi}_{rB}$ due to bending is obtained directly in an non-incremental way from the difference between the current and the initial position of the spheres (3.20) and the bending moment is calculated by applying:

$$\vec{M}_B = \vec{\varphi}_{rB} K_B. \tag{3.45}$$

In case the incremental formulation is used, the relative angular bending velocity is first calculated from the relative angular velocity between the two spheres (3.22) and the bending moment increment $\Delta\vec{M}_B$ as the product of the relative rotation and the bending stiffness K_B:

$$\Delta\vec{M}_B = \Delta\vec{\varphi}_{rB} K_B. \tag{3.46}$$

Finally, the total bending moment $\vec{M}_B$ can be calculated by summing the bending moment from the previous step and the the bending moment increment:

$$\vec{M}_{B\,(i)} = \vec{M}_{B\,(i-1)} + \Delta\vec{M}_B. \tag{3.47}$$

If plasticity is used (if the parameter *etaRoll* in the material definition is set to be greater than zero), a limiting bending moment is set and a perfect plasticity scenario is followed upon the point where the elastic bending moment exceeds the limiting bending moment. The maximal bending moment M_{Bmax} is calculated by applying:

$$M_{Bmax} = min(etaRoll\, r_1, etaRoll\, r_2)F_N. \tag{3.48}$$

If the elastic bending moment from the equation 3.45 (or 3.47 in the case of incremental formulation) exceeds the maximal bending moment, the value of the bending moment is set to the value of the maximal bending moment:

$$\vec{M}_B = \frac{\vec{M}_B}{\|\vec{M}_B\|} M_{Bmax}. \tag{3.49}$$

3.1.4 Motion integration

Each particle accumulates forces and torques from the contacts in which participates. The sums of these forces and torques are then used to integrate the equations of motion for each particle separately.

The motion integration is performed by applying the leapfrog algorithm, with some adjustments for the rotation of aspherical particles, as explained below. Consistently with the leapfrog algorithm, even derivatives are of positions and orientations are known at on-step points, whereas odd derivatives are know at mid-step points. Indexes $-$, $\circ$ and $+$ will be used to denote the previous, current and next timestep respectively, whereas $\ominus$ and $\oplus$ will be used to denote the previous and the next mid-step values.

Position

In order to calculate the particle position $\vec{u}^+$ in the next timestep, second Newton's law is first applied to calculate particle acceleration $\ddot{\vec{u}}^\circ$ in the current timestep:

$$\ddot{\vec{u}}^\circ = \vec{F}/m, \tag{3.50}$$

where $\vec{F}$ is the sum of all the contact forces acting on the particle and m is the mass of the particle. Second order finite difference with timestep Δt can then be applied to obtain:

$$\ddot{\vec{u}}^\circ \cong \frac{\vec{u}^- - 2\vec{u}^\circ + \vec{u}^+}{\Delta t^2}, \tag{3.51}$$

where $\vec{u}^-$ is the particle position in the previous timestep and $\vec{u}^\circ$ is the particle position in this timestep. The particle position in the next timestep can thus be expressed as:

$$2\vec{u}^\circ - \vec{u}^- + \ddot{\vec{u}}^\circ \Delta t^2 = \vec{u}^\circ + \Delta t \left(\frac{\vec{u}^\circ - \vec{u}^-}{\Delta t} + \ddot{\vec{u}}^\circ \Delta t \right), \tag{3.52}$$

By applying the first order finite difference with timestep Δt, average particle velocity of the previous timestep can be expressed as:

$$\dot{\vec{u}}^\ominus = \frac{\vec{u}^\circ - \vec{u}^-}{\Delta t} \tag{3.53}$$

and Eq. 3.52 can be rewritten as:

$$\vec{u}^+ = \vec{u}^\circ + \Delta t \big(\dot{\vec{u}}^\ominus + \ddot{\vec{u}}^\circ \Delta t \big). \tag{3.54}$$

The next mid-step velocity is then stored to be used in the next timestep calculation:

$$\dot{\vec{u}}^\oplus = \dot{\vec{u}}^\ominus + \ddot{\vec{u}}^\circ \Delta t \tag{3.55}$$

Orientation of spherical particles

Current angular acceleration $\ddot{\vec{\phi}}^\circ$ can be calculated from current sum of torques $\vec{T}^\circ$ and particle inertia tensor $\mathbf{I}$, which is diagonal in any orientation ($I_{11} = I_{22} = I_{33}$), since the particle is spherical. Current angular acceleration thus equals:

$$\ddot{\phi}^\circ{}_i = T_i / I_{11} \tag{3.56}$$

and the particle orientation in the following timestep $\vec{\phi}^+$ can be calculated in an analogous way to particle positions:

$$\vec{\phi}^+ = \vec{\phi}^\circ + \Delta t \left(\dot{\vec{\phi}}^\ominus + \ddot{\vec{\phi}}^\circ \Delta t \right), \tag{3.57}$$

where the next mid-step angular velocity $\dot{\vec{\phi}}^\oplus$ needs to be stored for the next timestep calculation:

$$\dot{\vec{\phi}}^\oplus = \dot{\vec{\phi}}^\ominus + \ddot{\vec{\phi}}^\circ \Delta t \tag{3.58}$$

Orientation of aspherical particles

Integrating the rotation of aspherical particles is considerably more complicated, because their local reference frame is not inertial. Rotation of a rigid body in a local frame, where the inertia matrix is diagonal, is described in continuous form by Euler's equations:

$$T_i = I_{ii}\ddot{\phi}_i + (I_{kk} - I_{jj})\dot{\phi}_j\dot{\phi}_k,\ i \in \{1, 2, 3\}. \tag{3.59}$$

Due to the fact that the first and second derivative of particle orientation appear simultaneously in Euler's equations, they can not be solved by the standard leapfrog algorithm. Instead YADE utilizes an algorithm, developed by Fincham [Allen and Tildesley, 2017] for molecular dynamics, where the leapfrog algorithm is extended, by estimating the missing on-step quantities from the known half-step quantities and vice-versa. In every timestep, the current angular momentum $\vec{L}^{\circ}$ is first calculated from the current torque and the angular momentum of the previous mid-step $\vec{L}^{\ominus}$:

$$\vec{L}^{\circ} = \vec{L}^{\ominus} + \vec{T}^{\circ}\frac{\Delta t}{2}. \tag{3.60}$$

In an analogous way, the angular momentum of the next mid-step $\vec{L}^{\oplus}$ is determined:

$$\vec{L}^{\oplus} = \vec{L}^{\ominus} + \vec{T}^{\circ}\Delta t. \tag{3.61}$$

The rotation matrix $\mathbf{A}$ is used to converge the angular momentums into their local inertial reference frame (the sign $\sim$ will henceforth be used to denote vectors in the local coordinate systems):

$$\widetilde{\vec{L}^{\circ}} = \mathbf{A}\vec{L}^{\circ} \tag{3.62}$$

$$\widetilde{\vec{L}^{\oplus}} = \mathbf{A}\vec{L}^{\oplus} \tag{3.63}$$

The angular velocities of the current timestep and next mid-step can be evaluated in the local inertial reference frame by applying:

$$\widetilde{\dot{\vec{\phi}}^{\circ}} = \widetilde{\vec{I}^{\circ-1}}\widetilde{\vec{L}^{\circ}} \tag{3.64}$$

$$\widetilde{\dot{\vec{\phi}}^{\oplus}} = \widetilde{\vec{I}^{\circ-1}}\widetilde{\vec{L}^{\oplus}} \tag{3.65}$$

Angular velocities are converted back to the global coordinate system:

$$\dot{\vec{\phi}}^{\oplus} = \mathbf{A}^{-1} \widetilde{\dot{\vec{\phi}}^{\oplus}} \tag{3.66}$$

and the orientation in the next timestep is calculated by applying:

$$\vec{\phi}^{+} = \vec{\phi}^{\circ} + \dot{\vec{\phi}}^{\oplus} \Delta t \tag{3.67}$$

Clumps

DEM simulations often make use of rigid aggregates of particles called clumps [Price et al., 2007] to model complex shapes. Dynamic properties are computed from the properties of its members.

For clumps that consist of non-overlapping particles, the clump mass m_c is computed by summing the masses m_i of all the constituting particles:

$$m_c = \sum_i m_i. \tag{3.68}$$

The inertia tensor is computed using the parallel axis theorem:

$$\mathbf{I}_c = \sum_i (m_I d_i^2 + I_i), \tag{3.69}$$

where d_i is the distance from the center of clump member i to clumps centroid and I_i is the inertia tensor of the clump member.

Mass of clumps that consist of overlapping particles on the other hand, is summed over cells, using a regular grid spacing inside axis-aligned bounding box of the clump. The inertia tensor is computed using the parallel axis theorem:

$$\mathbf{I}_c = \sum_j (m_I d_j^2 + I_j), \tag{3.70}$$

where m_j is the mass of cell j, d_j is the distance from cell center to clump's centroid and I_j is the inertia tensor of the cell j.

In YADE, clump members are treated as stand-alone particles in the stages of contact detection and contact force evaluation, except that they have no contacts created among themselves inside the clump. However in the stage of motion integration, the clumps is treated as a single entity, to which the member forces $\vec{F}_i$ and torques $\vec{T}_i$ are applied according to:

$$\vec{F}_c = \sum_i \vec{F}_i \tag{3.71}$$

$$\vec{T}_c = \sum_i \vec{r}_i \times \vec{F}_i + \vec{T}_i, \tag{3.72}$$

where r_i is the vector between the centres of masses of clump member and clump. Motion of the clump is the integrated using aspherical rotation integration.

3.2 Computational considerations

DEM computations are performed using an explicit integration scheme, which is inherently only conditionally stable, providing that the simulation timestep Δt is sufficiently small. The critical timestep Δt_{CR} for continuum equations is based on the sonic speed: the elastic wave must not propagate farther than the minimum distance of integration points during one timestep. For a system of spherical discrete elements, the critical timestep can be expressed as [Zhao, 2017]:

$$\Delta t_{CR}^{DEM} = min\left(\sqrt{\frac{m_i}{K_i}}\right), \tag{3.73}$$

where m_i and K_i are the mass and stiffness of discrete element i.

The numerical cost of a simulation is inversely proportional to the timestep and since the critical timestep directly depends on the particle masses and contact stiffnesses, the choice of these parameter values has a crucial effect on the computational time.

- **Contact stiffness:** In DEM simulations, particle overlap is used as a penalty parameter to evaluate contact force, based on the contact stiffness (Eq. 3.26). However, the validity of the simulations is conditioned by the rigid grain limit [Cundall and Strack, 1979; Da Cruz et al., 2005], i.e. sufficiently large contact stiffness to insure these overlaps are negligibly small with respect to particle sizes. In YADE, contact stiffness is determined by the value of the radii and Young's moduli of the two particles in contact (Eq. 3.24). Increasing Young's modulus thus increases the computational accuracy, but reduces the critical timestep (Eq. 3.73) and a balance is sought between the computational accuracy and numerical cost.

- **Particle masses:** Particle masses are computed from the material density and particle volumes. Although material density should correspond to the properties of the simulated material, it can be increased in order to increase the critical timestep (Eq. 3.73) and decrease the computational cost. The approach is valid, providing the system remains in a quasi-static regime during the entire duration of the simulation [Sheng et al., 2004; Hagenmuller et al., 2015].

Chapter 4

A medial axis based method for irregular grain shape representation in DEM simulations

Abstract This paper describes a novel method for representing arbitrary grain shapes in Discrete Element Method (DEM) simulations. The method takes advantage of the efficient sphere contact treatment in DEM and approximates the overall grain shape by combining a number of overlapping spheres. The method is based on the medial axis transformation, which defines the set of spheres needed for total grain reconstruction. This number of spheres is then further diminished by selecting only a subset of reconstructing spheres and opting for a grain approximation rather than a full grain reconstruction. The effects of the grain approximating parameters on the key geometrical features of the grains and the overall mechanical response of the granular medium are monitored by an extensive sensitivity analysis. The results of DEM quasi-static oedometric compression on a granular sample of approximated grains exhibit a high level of accuracy even for a small number of spheres.

Contents

4.1 Introduction

The microstructure of a granular material, i.e. the relative arrangement and orientation of these grains, can have a crucial effect on its mechanical response [Kochmanová and Tanaka, 2010; Zhao et al., 2016]. In turn, microstructure can be strongly affected by the shape of grains [Szarf et al., 2009; Albaba et al., 2015; Markou, 2016]. Nowadays the 3D shape of grains and microstructure can be directly accessed with techniques such as X-ray tomography [Andò et al., 2012; Hagenmuller et al., 2013; Schleef et al., 2014]. In this study, we will consider the case of a specific material, namely snow, for which we expect a particularly strong effect of microstructure on the macroscopic behaviour [Schweizer and Jamieson, 2001; Schweizer et al., 2003]. Snow consists of a highly porous continous ice matrix (void ratio up to 9) that, in fast deformation regime, can be regarded as a cohesive granular material. In this regime, which is typical of snow avalanche initiation [Gaume et al., 2015, 2017b], macroscopic deformations are primarily caused by rearrangements of grains [Hagenmuller et al., 2014b] that can come in a large variety of shapes, from rounded to faceted or elongated [Fierz, 2009]. The objective of this work is to devise an efficient method to investigate the mechanical behaviour of this material through DEM simulations.

In Discrete Element Method (DEM) [Cundall and Strack, 1979; Radjai and Dubois, 2011], granular materials are usually modelled as collections of spherical particles. The deviation of the particle shape from a sphere can be taken into account indirectly through parameters such as rolling friction that simulate grain interlocking [Ai et al., 2011]. However, a priori estimating the rolling friction parameter that could capture the effect of the grain shapes on the mechanical response of the granular assembly remains problematic [Wensrich and Katterfeld, 2012]. Alternatively, the exact 3D shape of grains can also be explicitly modelled in the DEM. However, assigning the shape of the grains to the discrete elements (DEs) themselves, by modelling them as polyhedron [Hart et al., 1988; Hogue, 1998; Lee et al., 2009], turns out to be very computationally expensive due to complex contact detection and contact forces calculation. A more efficient way of modelling an arbitrary grain shape in DEM is by utilising a multitude of spheres in order to capture the geometry of the grain [Kruggel-Emden et al., 2008]. A grain is thus represented by a clump of spheres that behaves as a single rigid body. This way the efficiency of the DEM in handling contacts between spheres can be preserved. The downside of the method is, since every grain is represented by a multitude of spheres, a large number of elements for contact detection, which renders the DEM simulations slow. This makes the efficiency of the grain approximating method, in terms of the number of utilized spheres, of primary importance.

Regarding the sphere-based representations of grains, a straight-forward approach was adopted by Hagenmuller et al. [2015], who modelled grains by arranging a set of smaller spherical discrete elements on an orthogonal grid along the grain boundary. This approach produces a very fine grain shape discretization, but results in a very large number of discrete elements, rendering simulations very slow. Multiple authors have instead chosen the overlapping sphere approach, where the grain is represented by a set of larger spheres allowed to overlap that fill the volume of the grain. Most of the studies that adopted this approach [Price et al., 2007; Ferellec and McDowell, 2010; Amberger et al., 2012; Gao et al., 2012] are based on first populating the grain shape with a large number of spheres, and then applying a secondary algorithm that discards certain spheres in accordance with a predefined criterion in order to achieve a grain approximation at a moderate number of spheres. The original population of spheres in these methods can however involve redundant information [Coeurjolly et al., 2008]. In addition, some of these methods [Price et al., 2007; Ferellec and McDowell, 2010] involve a certain level of randomness in the initiation of the process. In this study, in search of an optimal grain mapping with a reduced number of spheres, we propose a method for reducing the redundancy while objectively calculating sphere positions.

Similarly to the above presented sphere overlapping methods, the approach developed here is based on first creating an initial set of sphere candidates, and then filtering this set in order to obtain a final grain approximation. However, the redundancy of the initial set of spheres is significantly reduced by applying the medial axis transformation before applying the filtering. Thus, the initial set of spheres is diminished while still including all the spheres needed for a complete grain approximation. Although medial axis is a commonly used tool for shape approximation in computer graphics and computer vision [Bradshaw and O'Sullivan, 2004; Stolpner et al., 2012], to our knowledge it has not yet been applied in the field of granular mechanics. In the second step, this set of spheres is then filtered in order to obtain a grain approximation at a moderate number of spheres. Compared to [Bradshaw and O'Sullivan, 2004; Stolpner et al., 2012], we employ here a simple and robust filtering criterion that allows a variety of different grain approximations depending on the choice of two approximating parameters.

The paper is organized as follows: The developed method for grain approximation is presented in section 4.2 and the tools for geometrical evaluation of approximated grain shapes are described in section 4.3. The functioning of the method is demonstrated in section 4.4, by applying it to a sample of snow. X-ray-tomography-derived shapes of snow grains are approximated with the developed method and the key geometrical features of the grains are studied with respect to the values of approximating parameters. Finally these results are put into perspective by simulating and studying the mechanical response of the snow sample in quasi-static oedometric compression with respect to these grain approximating parameters.

4.2 A medial axis based grain approximating method

The input data utilized by the method is a discrete binary image of the grain assembly (in our particular case, the grains are derived by segmentation from tomographical 3D images of snow microstructure [Hagenmuller et al., 2013]). The first stage of the grain approximating process consists of performing a medial axis transformation on the grain image. This results in a set of points that represent the centres of a set of spheres necessary for a complete grain reconstruction.

4.2.1 The medial axis transformation

The medial axis (MA) [Blum, 1976] is a classical tool for shape recognition. It consists of all the points having more than one nearest point on the object's boundary, thus forming the topological skeleton of the object. By combining the MA with the distance transformation (DT), which bears the information on the Euclidian distance of each object point to the closest surface point, the information on object shape is highly reduced, yet sufficient for a complete object shape reconstruction. The object is reconstructed with a minimal necessary number of spheres by placing spheres of appropriate radii on each point of the MA (Fig. 4.1).

If however, one applies the MA transformation to a discrete image, the discrete medial axis (DMA) thus produced contains a number of redundant

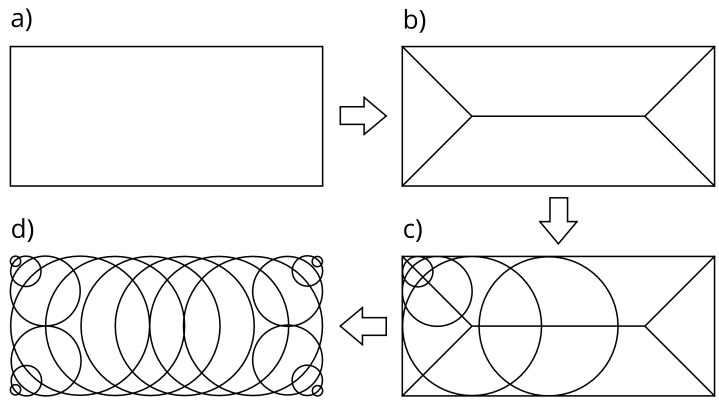

Figure 4.1: Four stages of a 2D object reconstruction: a) binary image of the object, b) the medial axis of the object, c) population of the medial axis with disks, d) reconstructed image.

pixels/voxels. These pixels/voxels represent the centers of spheres that contribute no information to the grain topology as they are completely covered by the neighbouring spheres due to their discretization. Optimally reducing the medial axis, i.e. finding the minimal medial axis, has been proven to be NP-hard [Coeurjolly et al., 2008].

Our algorithm to compute a reduced medial axis consists of the following steps. The discrete medial axis is defined as a 3D binary image $DMA = DMA_{ijk}$ (Fig. 4.2(c)), obtained by filtering the local minima points from the $DT = DT_{ijk}$ (Fig. 4.2(b)) of the binary grain image P (Fig. 4.2(a)). This filtering is performed by applying the following condition to the interior of P:

$$\begin{aligned} \text{if} \quad DT_{ijk} > DT_{lmn} - D(P_{ijk}, P_{lmn}) : \quad & DMA_{ijk} = 1 \\ \text{else} : \quad & DMA_{ijk} = 0 \end{aligned} \tag{4.1}$$

where the point P_{lmn} is a neighbouring discrete image point of P_{ijk}, (a neighbouring voxel in this case is defined as a voxel that shares a face, an edge or a vertice with the reference voxel) and $D(P_{ijk}, P_{lmn})$ is the Euclidian distance between the two points. The inequality condition in eq. (4.1) verifies whether the sphere associated to a certain point P_{ijk} is completely covered by any of the discrete spheres associated with the neighbouring points P_{lmn}. We then define the enriched medial axis EMA (Fig. 4.2(d)) as:

$$EMA_{ijk} = DMA_{ijk} DT_{ijk} \tag{4.2}$$

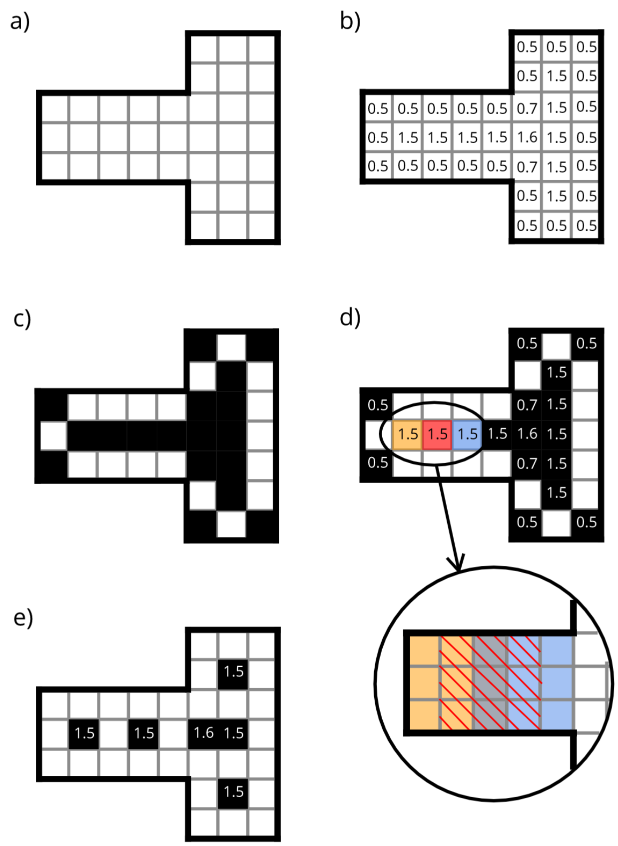

Figure 4.2: Five stages of a 2D discrete object reconstruction: a) binary image P of the object, b) distance transformation DT, c) the discrete medial axis DMA, d) enriched medial axis EMA, e) reduced enriched medial axis $REMA$. Three voxels (orange, red and blue) from the image d) are chosen in order to demonstrate the redundancy of information in EMA. The provided zoom shows generated discrete disks (which appear square at this resolution) for the three chosen voxels. The hatched red disk (pertaining to the red voxel) is completely covered by the neighbouring orange and blue disks (pertaining to the orange and blue voxels) and is therefore redundant.

In order to remove the redundant points of the EMA and obtain a reduced enriched medial axis $REMA$ (Fig. 4.2(e)), all the points representing spheres that are completely covered by the union of the other reconstructing spheres (Fig. 4.2(d)) are removed. The process is carried out point by point, from lowest to highest EMA values (representing the radii of the reconstructing spheres), which effectively promotes the use of larger spheres for reconstruction. At this stage $REMA$ contains all the necessary information for a complete reconstruction of the discrete image.

4.2.2 The grain approximating process

For the purpose of DEM simulations on a granular material, a full reconstruction of grain shapes might not be necessary - an issue which will be further analyzed in the following sections. Instead, a balance between the number of constituting spheres and the level of grain shape approximation is sought. Hence, in order to reduce the number of utilized spheres, only a subset of all the reconstructing spheres is selected for grain approximation, resulting in varying degrees of approximation, depending on the choice of two grain approximating parameters defined below: the delete ratio D and the minimal sphere radius R_{min}.

The approximating process (Fig. 4.3) is carried out by iteratively selecting the largest radius value r in $REMA$ and deleting all the other $REMA$ points at a distance less than Dr from the considered sphere center. The process is stopped once the value of the selected point is smaller than the value of R_{min} parameter. The remaining points constitute the grain approximating map, where each point represents the centerpoint of an approximating sphere with a radius that equals the value of that point.

Effectively the delete ratio D sets the density of the spheres forming the approximated grain surface - the larger the parameter value, the larger the artificial grain roughness that emerges as a consequence of approximating an originally smooth surface with a set of spheres, as shown in the right column of Fig. 4.4. The minimal sphere radius R_{min}, on the other hand, smooths out the sharp edges of the grain as well as the details on grain surface with a characteristic size smaller than R_{min}, as shown in the left column of Fig. 4.4. Hence the delete ratio D can be interpreted as the parameter that controls the artificial grain roughness, and minimal sphere radius R_{min} as the parameter of grain detail resolution.

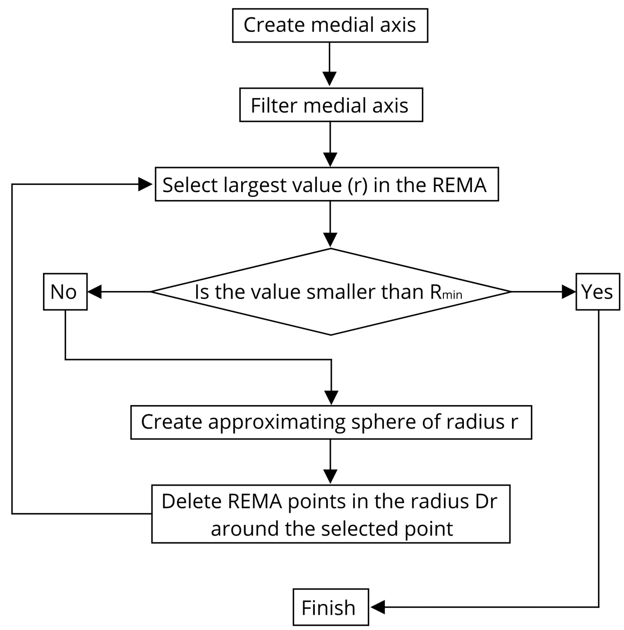

Figure 4.3: Process chart of the developed grain approximating method.

4.3 Geometrical evaluation of grain approximation

In this section the quality of grain approximation is quantified by means of three geometric shape descriptors that are deemed to have a key influence on the mechanical response of a granular material: the volume, the anisotropy and the surface roughness of approximated grains.

In the following, the term original grain image (OGI) will refer to the original binary voxel image of the grain, and the term approximated grain image (AGI) will refer to the binary voxel representation of the approximated grain. However, since the grain approximating algorithm is designed for modelling grains in a DEM simulation, one is mainly interested in the interaction between the grains. In this respect, not all the points on the surface of an approximated grain are attainable to other grains that come into contact with the observed grain. Depending on the radius R of the considered sphere in contact, some concavities on the surface of the observed grain will be out of reach to the grain that comes into contact (Fig. 4.5).

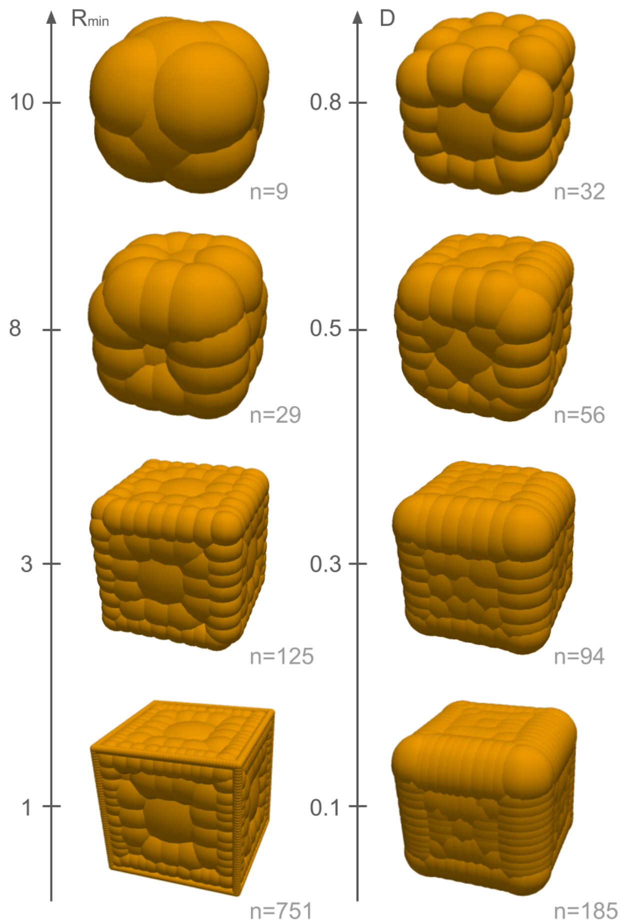

Figure 4.4: The effect of the two grain approximating parameters shown on a cubic grain of dimensions 51x51x51 voxels. The left column represents the effect of varying R_{min} while keeping D fixed; the right column represents the effect of varying D while keeping R_{min} fixed. The resulting number of spheres n is indicated for each approximated cube.

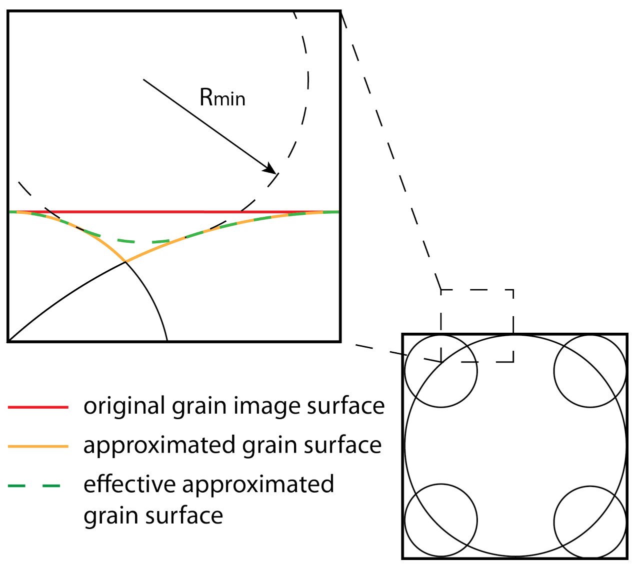

Figure 4.5: A sketch demonstrating the effective approximated surface. In the bottom right corner of the sketch, a square object is approximated by a set of 5 disks. A zoom onto the surface of the object reveals the difference between the original object surface (red line), the approximated object surface (orange line) and the effective approximated object surface(dashed green line).

These concavities will effectively constitute a part of the observed grain: this expanded volume will henceforth be referred to as the effective approximated grain image ($EAGI(R)$), which is a function of R (Fig. 4.6(a)). The larger the radius R, the smoother the grain will appear. The $EAGI(R)$ can be calculated by applying the binary closing operation ($\bullet$) by a sphere (S) with a radius R on AGI:

$$EAGI(R) = AGI \bullet S(R). \tag{4.3}$$

The binary closing operation is defined as dilation followed by erosion using the same structuring element for both operations - sphere in this case. Effectively the resulting binary image $EAGI(R)$ is the volume of AGI which is unattainable to a sphere of radius R. Similarly, the effective original grain image $EOGI(R)$ can be defined as:

$$EOGI(R) = OGI \bullet S(R). \tag{4.4}$$

The three geometric shape descriptors considered in this study can now be defined as follows. The *volumetric error* E_V of an approximated grain is computed as the volumetric difference between the effective original and the effective approximated image of the grain, divided by the total volume of the effective original grain image:

$$E_V = \frac{\sum_{ijk} (EOGI(R_{min})_{ijk} - EAGI(R_{min})_{ijk})}{\sum_{ijk} EOGI(R_{min})_{ijk}} \tag{4.5}$$

and represents the error of approximation in terms of relative volume. $EAGI$ (as well as $EOGI$) in eq. (4.5) is calculated for the radius value of R_{min} (Fig. 4.5), as this represents a set of points which constitute a part of the approximated grain volume independently of the actual size of sphere in contact. The volumetric error can take up values $0 < E_V < 1$, where $E_V = 0$ represents a perfectly reconstructed grain. Since the approximating spheres are by definition always inside OGI, E_V is never negative.

The *anisotropical error* E_A is defined as the ratio between the anisotropy of the effective approximated grain and the anisotropy of the effective original grain image, where the anisotropy is computed as the ratio between the maximal (M_{max}) and the minimal moment of inertia (M_{min}) of an individual grain:

$$E_A = \frac{M_{max}(EAGI)/M_{min}(EAGI)}{M_{max}(EOGI)/M_{min}(EOGI)} - 1. \tag{4.6}$$

It is noteworthy that the moments of inertia are calculated on binary images. As such, the anisotropical error does not take into account the mass distribution of overlapping approximating spheres, but rather the combined shape of the union of spheres. The anisotropy value errors are shifted by one in order to be centered around 0. An approximated grain with the same anisotropy as the original grain will produce the anisotropical error $E_A = 0$. Values of $E_A < 0$ indicate an approximated grain with a diminished anisotropy, while vice-versa is true for values $E_A > 0$.

The last descriptor, *surface roughness error* E_R, quantifies surface roughness of the approximated grain relative to surface roughness of the original grain. The emphasis is put on the artificial roughness that appears as an artefact of the approximating process, due to a plane surface being approximated by a set of spheres. Surface of the approximated grain will appear rougher for a smaller particle in contact(Fig. 4.6(b)) which is consistent with the fact that surface roughness is usually considered a scale-dependent parameter [Fardin et al., 2001]. As we are foremost interested in the interaction of the grain surface with the spheres constituting the other grains in contact, binary closing with a sphere was chosen as a topological tool to characterize the surface roughness. Essentially, this topological tool mimics the contact of a spherical element with the grain surface. We thus base the E_R parameter on the evolution of the volume of $EAGI(R)$ with respect to radius R:

$$vol(EAGI)(R) = \sum_{ijk}(AGI \bullet S(R)), \tag{4.7}$$

where the R values are here taken as all integers in the interval between the minimum (R_{min}) and maximum values of sphere radii used for grain approximation. The same process is repeated for the $EOGI(R)$:

$$vol(EOGI)(R) = \sum_{ijk}(OGI \bullet S(R)). \tag{4.8}$$

Plotting the values of $vol(EOGI)$ and $vol(EAGI)$ against R (Fig. 4.6(b)) reveals a near-linear dependence. A least squares method is used in order to obtain linear approximations of the two discrete functions:

$$vol(EAGI)(R) \approx a_1 R + b_1 \tag{4.9}$$

$$vol(EOGI)(R) \approx a_2 R + b_2. \tag{4.10}$$

Finally the ratio between the slopes of the two curves is taken as a measure of the ratio of roughnesses of the approximated and the original grain image. The surface roughness error is then defined by diminishing this ratio by one in order to center the shape descriptor around zero:

$$E_R = a_1/a_2 - 1. \tag{4.11}$$

The volume of two images with the same surface roughness will grow at the same rate with respect to the closing radius, resulting in the value of grain surface roughness error $E_R = 0$. As the grain approximation becomes coarser and effectively produces a rougher surface, the volume of the approximated grain image will grow at a faster rate than the original grain image (with respect to the closing radius), resulting in a grain surface error $E_R > 0$.

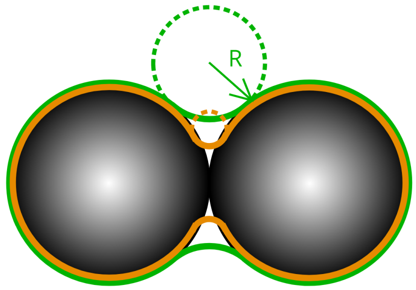

(a) The radius R of the closing sphere influences the EAGI volume.

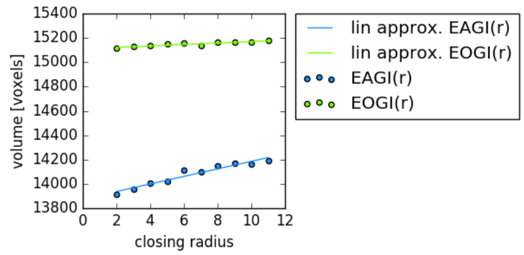

(b) The volumes of $EOGI$ and $EAGI$ are plotted against the closing sphere radius R and a linear approximation is computed via least squares method.

Figure 4.6: The computational process of roughness error E_R.

4.4 Application of the developed grain approximating algorithm to a granular material

In this section, the developed grain approximating algorithm is applied to a real granular material in order to demonstrate the capabilities of the method. First, a sensitivity analysis of the geometric shape descriptors of the approximated medium is performed with respect to the two grain approximating parameters. In a second stage, the mechanical response of the approximated granular material is investigated by performing a series of quasi-static oedometric compression DEM simulations with different values of grain approximating parameters.

The material chosen for these numerical tests is snow of type rounded grain [Fierz, 2009]. A tomographical X-ray image (Fig. 4.7(a)) serves as the input information on the microstructure of the material [Flin et al., 2004]. The sample is cubic with a sidelength of 4.9 mm and a void ratio of 2.79. The assumption that snow behaves as a cohesive granular material is adopted, and the tomographical image is segmented (Fig. 4.7(b)) into individual grains by detecting the weak mechanical points, i.e. neck regions in the snow matrix, using a segmentation algorithm developed in [Hagenmuller et al., 2014b,a]. The final segmented image contains 1510 grains, which are then approxi-

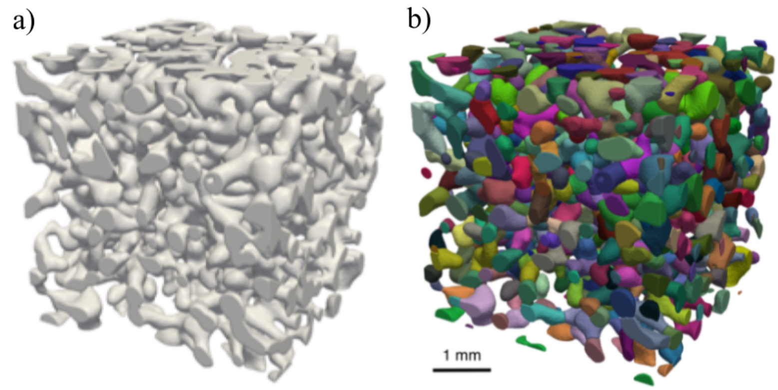

Figure 4.7: Sample of rounded grain snow used for the evaluation of the developed grain approximated algorithm: a) tomographical binary x-ray image of the snow b) identification of individual grains in the image.

mated with the approach described above.

4.4.1 Geometrical sensitivity analysis

A sensitivity analysis of the three shape descriptors with respect to the two grain approximating parameters (and the number of utilized spheres) is performed on a subset of 10 grains (Fig. 4.8) of the considered snow sample.

Evolution of the number of spheres needed for approximation of the set of grains with respect to the ranging values of the two approximating parameters is shown in Fig. 4.9. As expected, low values of parameters D and R_{min} result in a large number of approximating spheres due to placing spheres close together and using a large spectrum of sphere radii values. This choice of parameters however also results in a minimum volumetric error, as shown in Fig. 4.10. Choosing a large value of the two grain approximating parameters, on the other hand, results in a small number of approximating spheres and a large volumetric error. In fact Fig. 4.9 and Fig. 4.10 exhibit nearly mirrored evolutions of the number of spheres and volumetric errors. Evidently, there is a trade-off between the number of approximating spheres and the accuracy of grain approximation.

Fig. 4.11 shows the influence of the two grain approximating parameters on the average anisotropy error of the set of observed grains. Again, low values of the two grain approximating parameters result in a fine approxima-

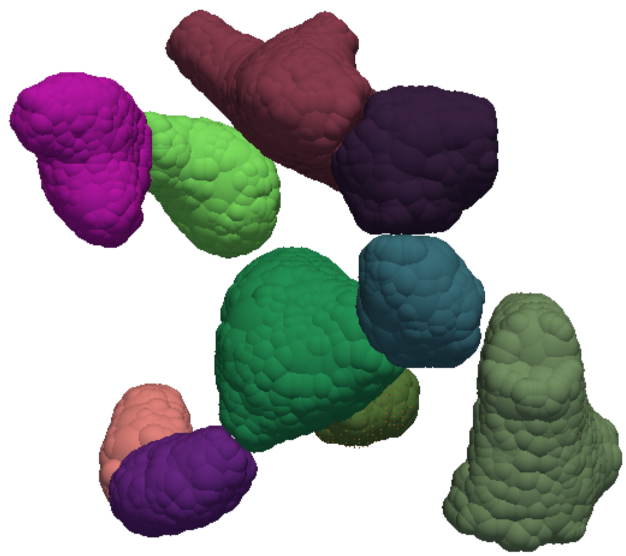

Figure 4.8: Set of 10 grains of rounded grain snow, upon which the sensitivity analysis has been conducted.

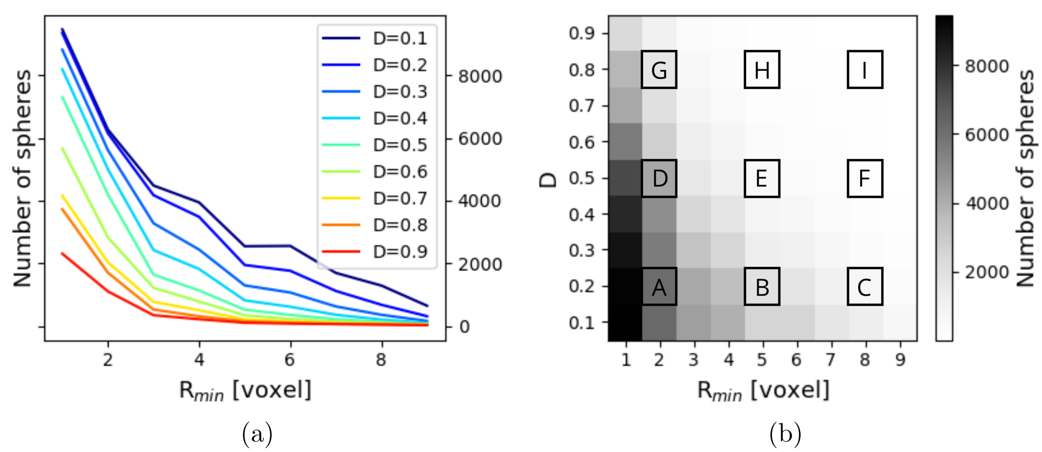

Figure 4.9: Influence of the two grain approximating parameters on the number of spheres needed to represent the observed set of 10 grains. Letters A-I on figure (b) mark the 9 grain approximating parameter combinations that are later chosen for the mechanical simulations.

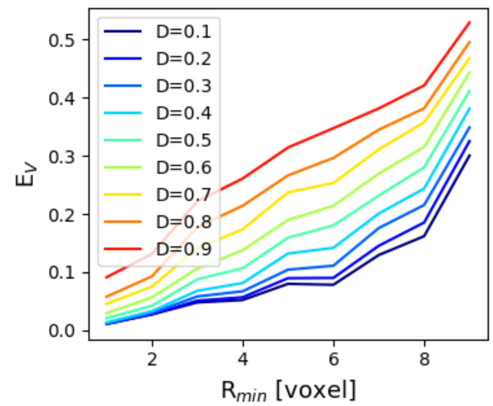

Figure 4.10: Influence of the two grain approximating parameters on the volumetric error E_V, produced by the approximation of the observed set of 10 grains.

tion of the grain shapes and consequently a low anisotropy error. However, high values of the two parameters do not necessarily produce a larger error in terms of anisotropy, but they do seem to result in a larger variability of the anisotropy error. One can also note that at low values of D, increasing the value of the R_{min} results in a gradual decrease of the anisotropy error into the negative region, indicating that the anisotropy of the approximated grains is smaller than the anisotropy of the reference grains. This is a result of approximating grains becoming gradually more "spherical" as R_{min} is increased. At a threshold of $R_{min} \approx 7$, the anisotropy error starts rapidly increasing due to the fact that R_{min} reaches the characteristic size of grains and some of the elongated grains get split into two unconnected parts.

The influence of the two grain approximating parameters on the average surface roughness error of the approximated set of grains is shown in Fig. 4.12. Again, the minimal values of the two grain approximating parameters produce a near unchanged grain surface roughness of the approximated grains with respect to the original grain images ($E_R \approx 0$). Increasing parameter D increases the size of concavities between the spheres forming the object surface, which results in an increase of E_R. It can also be observed that the approximated grain surface obtained by the combination of the minimum value of D and the maximum value of R_{min} is smoother than that of the original grain image ($E_R < 0$) due to small concavities and large spheres.

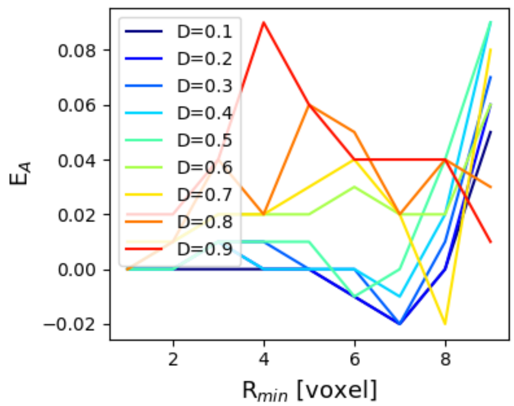

Figure 4.11: Influence of the two grain approximating parameters on the anisotropy error E_A, produced by the approximation of the observed set of 10 grains.

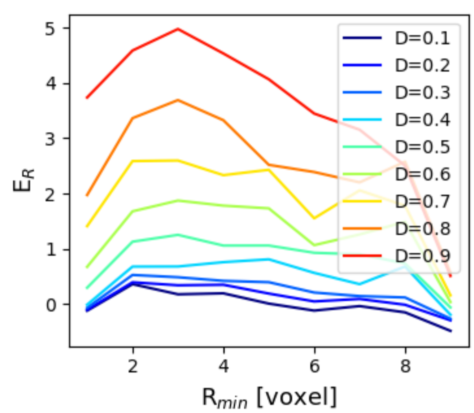

Figure 4.12: Influence of the two grain approximating parameters on the surface roughness error E_R, produced by the approximation of the observed set of 10 grains.

This sensitivity analysis provides an insight into the correlation between the number of approximating spheres and the shape of approximated grains. While the quality of grain approximation in terms of volume seems to be roughly proportional to the number of utilized spheres, this is not the case for grain approximation quality in terms of anisotropy and surface roughness. Effectively a more accurate approximation in terms of volume will result in an increase of the sphere number, while a more accurate approximation in terms of anisotropy and surface roughness might be achieved without a substantial sphere number increase. In order to examine which of these shape descriptors have a key influence on the mechanical behaviour of the granular material, a mechanical investigation is then performed.

4.4.2 The effect of grain approximation on the mechanical behaviour of the granular material

A series of mechanical loading simulations is performed on the sample of rounded grain snow in order to study the effect of the two grain approximating parameters - and consequently the effect of shape descriptors - on the mechanical response of the granular material. The loading path chosen for this sensitivity analysis is a simple oedometric path (Fig. 4.13).

Simulations are performed with DEM solver YADE [Šmilauer et al., 2010]. Snow grains, approximated with the developed method, are modelled as rigid unbreakable clumps of spheres. These clumps are connected by elastic-brittle cohesive bonds with other grains with which they are in contact in the original image. Cohesion between the grains is imposed by first estimating, from the original image, the area of the contact surface between each pair of grains in contact. Each pixel on the contact surface of a grain is then assigned to the nearest approximating sphere. Afterwards, for each pair of pixels in contact, a cohesive bond is created between the two pertaining approximating spheres. If more than one pair of pixels in contact corresponds to the same pair of approximating spheres, the magnitude of the cohesive bond is multiplied accordingly. The sum of magnitudes of all the cohesive bonds between a pair of grains is thus proportional to the contact surface between the two grains, while cohesion is distributed between all the spheres that form the contact surface.

Simulation parameters are chosen as follows: a Young's modulus (that

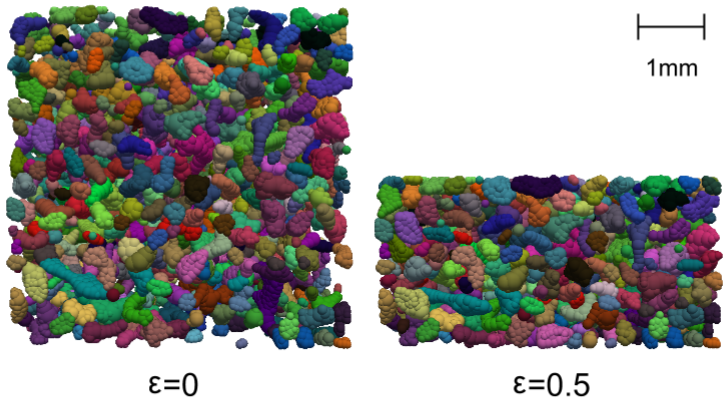

Figure 4.13: The snow sample of 1510 grains prior to mechanical loading ($\varepsilon = 0$) and at the vertical strain of $\varepsilon = 0.5$.

defines contact stiffness) $E = 10^8$ Pa, a grain density $\rho = 970 \cdot 10^3$ kg m^{-3}, a contact friction coefficient $\mu = 0.02$, and a Cundall's non viscous damping coefficient 0.02. Cohesion is modelled with a brittle elastic law with a strength of $C = 10^6$ Pa. The sample is compressed with a velocity $v = 1$ cm s^{-1}, which is sufficiently slow for the test to remain in the quasi-static regime. Note that the value of grain density has been strongly increased, and the Young's modulus decreased, with respect to those of ice in order to make the calculation times reasonable. A sensitivity analysis has been performed in order to make sure that the change in the values of these material parameters has a negligible effect on the results, and that the simulations are performed in the rigid grain limit [Cundall and Strack, 1979; Da Cruz et al., 2005].

Nine combinations of grain approximating parameters have been chosen for performing the mechanical simulations (Fig. 4.9(b)). The combination A ($D = 0.2, R_{min} = 2$) represents the control combination, offering a near-complete reconstruction of grains in terms of all the shape descriptors. The volumetric error of grain approximation in this case is on the same order as the volumetric variation of the input tomographical X-ray image [Hagenmuller et al., 2016] due to the choice of image processing parameters. The other parameter combinations B-I produce a variety of results allowing for a thorough study of not only the effect of grain approximating parameters, but also of the shape descriptors on the mechanical properties of the granular material.

The stress-strain response of the sample in the simulated oedometric

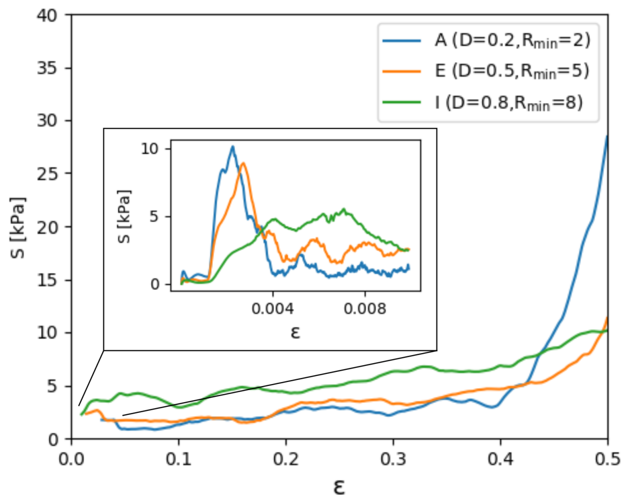

Figure 4.14: The simulated stress-strain response of the sample, where ε denotes the vertical strain of the sample and S denotes the vertical stress produced by compacting the sample. Figure shows the response of approximations A (reference approximation), E (best choice approximation) and I. A close-up into the initial phase of sample loading is also provided.

compression is shown in Fig. 4.14. For clarity, only the response of parameter combinations A (control approximation), E (later chosen as the best choice approximation) and I (a relatively inaccurate mechanical response) are shown. Several distinct phases of compression can be observed on the reference response: Deformation starts with an initial quasi-elastic stress build-up followed by a subsequent strain softening phase (Fig. 4.14 inset). The strain softening is linked to the damage taking place in the specimen in form of broken cohesive bonds between the grains. This damage then continues during the following phase of progressive grain rearrangements, which takes place between strains of $0.01 < \varepsilon < 0.4$ and occurs at a near-constant stress. Beyond the strain of $\varepsilon = 0.4$, a sharp increase in stress takes place, which is mostly linked to the elastic compaction of grains. At this point the specimen is almost completely decomposed into an assembly of cohesionless grains, and grain rearrangement can no longer account for the compaction. This last phase of the simulation is of no particular interest to the present investigation, due the fact that the assumption of rigid unbreakable grains is challenged. The response obtained with approximation E displays similar features as the reference response, except for the final stage of compression due

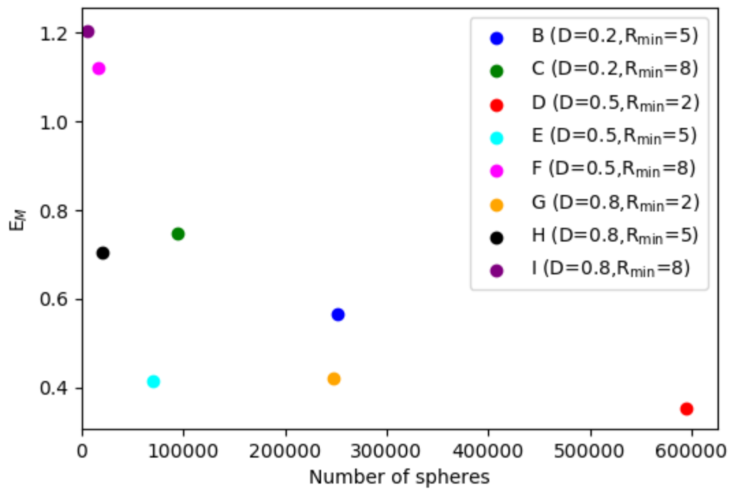

Figure 4.15: Mechanical error E_M of the stress-strain curves produced by differrent parameter combinations (B-I) with respect to the number of spheres needed for approximation.

probably to volumetric difference between the two approximated samples. On the contrary, approximation I results in a significantly altered response, both in the initial quasi-elastic phase and during the following stress plateau.

As a quantitative measure of accuracy of the simulated mechanical response, the normalized root mean square error (with respect to curve A) has been calculated for curves B-I in the range of $0 < \varepsilon < 0.4$. This root mean square error will henceforth be referred to as the mechanical error E_M. Fig. 4.15 depicts the dependency of E_M produced by different parameter combinations on the number of spheres used for approximation. The trend in the figure clearly exhibits a negative relation between the number of spheres and E_M. However since the observed decay is fast, a relatively small E_M can be obtained with a relatively small number of spheres. Parameter combination E can thus be regarded as the best-choice approximation, delivering relatively good mechanical results at a relatively small computational price.

Mechanical error E_M obtained with different approximation parameter combinations, were also compared to the three shape descriptors in order to reveal the influence of grain shape on the mechanical properties of the studied granular material. A regression analysis was performed between E_M and the values of shape descriptors (E_V,E_A and E_R). The high p-values for anisotropy

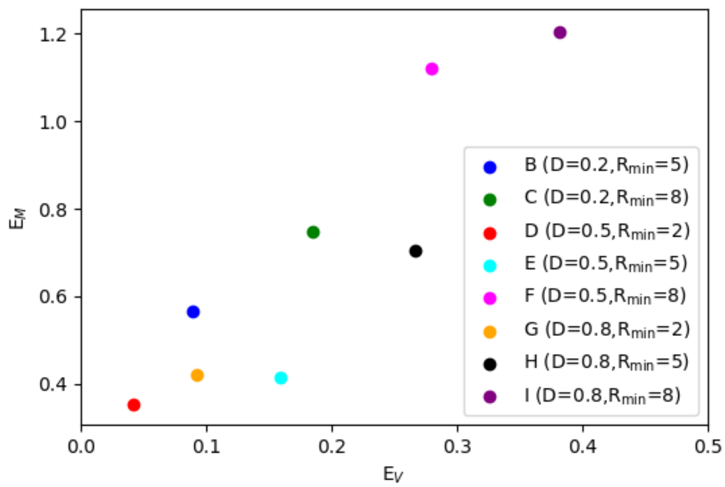

Figure 4.16: Mechanical error E_M of the stress-strain curves produced by differrent parameter combinations (B-I) with respect to the volumetric error E_V.

$p(E_A) = 0.10$ and surface roughness $p(E_R) = 0.95$ indicate that there is no statistically significant correlation between these two shape descriptors and the oedometric stress response of the studied granular material. On the other hand, the p-value for the volumetric error $p(E_V) = 0.002$ rejects the null hypothesis and indicates a strong correlation between this shape descriptor and the E_M of the stress response (Fig. 4.16).

As an indication, the simulations, presented in Fig. 4.14, were carried out on a single core Intel(R) Xeon(R) 2.20GHz processor. Calculation time varied between 1 hour (parameter combination I) and 338 hours (parameter combination A), whereas the simulation time of the best-choice parameter combination (E) was 17 hours.

4.5 Conclusions

In the present paper we have introduced a novel, efficient overlapping sphere approach to account for irregular grain shapes in a DEM model. The effectiveness of the method is examined by first performing an extensive geometrical sensitivity analysis of three geometrical descriptors of grains (volume, anisotropy and surface roughness) with respect to the two grain approximating parameters. Different combinations of grain approximating parameters were then also evaluated by simulating a quasi-static compressive loading on a granular sample. An approach to modelling large-strain response of a fragile porous assembly of sintered grains is presented and the results are analyzed with respect to the three grain shape descriptors.

The mechanical sensitivity analysis showed that by increasing the number of spheres used for grain approximation, the error of the mechanical response progressively diminishes. For the studied material, the dependency of accuracy of the mechanical response on the number of utilized spheres exhibited a fast decay, which provides a way to accurately simulate the compressive response with a relatively small number of spheres (resulting in a low simulation cost). The results of mechanical simulations also indicate that the compressive response of the studied material is mostly governed by the volumetric error.

Compared to alternative methods for sphere-based approximation of grains in DEM simulations [Price et al., 2007; Ferellec and McDowell, 2010; Amberger et al., 2012; Gao et al., 2012], the presented method features an objective refinement of potential sphere candidates by means of medial axis transformation, a tool more commonly used in computer science [Bradshaw and O'Sullivan, 2004; Stolpner et al., 2012]. The presented approach also features a simple and robust elimination of redundant spheres and a separate approximating algorithm. Due to the fact that the approximating process is defined by two parameters, different aspects of approximated objects (volume, anisotropy and surface roughness) can be controlled independently. This enabled us to study the effects of different grain shape characteristics on the mechanical response of the granular material and present a thorough study on the effect of grain approximation on simulation quality.

It can be concluded that the developed grain approximating method exhibits the capability of accurately accounting for arbitrary grain shapes in DEM simulations at a reasonable computational cost. The problem that is yet to be solved is how to define a priori the values of grain approximating parameters (that will result in accurate mechanical simulations), without performing the computationally expensive mechanical sensitivity analysis. For the moment, the volumetric error of grain approximation seems a promising indicator of quality of the simulated mechanical response of a granular material. It is however important to note that in oedometric tests on a granular material with a relatively low friction, shearing is not the prevailing deformational mechanism and the mechanical response is mostly associated to bond breakage and densification. Thus, whether volumetric error could indeed be used as an indicator of quality of the simulated mechanical response for different loading paths, needs to be further investigated.

Appendix

4.A Modelling grain contacts

This appendix provides a detailed insight into the methodology used to model the grain contacts between individual snow grains with particular emphasis on the initial cohesive contacts.

Cohesive-frictional contact law, described in section 3.1.3 is used to evaluate contact forces, where bending and twisting were not taken into account, by setting the bending and twisting stiffnesses to zero:

$$K_{TW} = 0 \tag{4.12}$$

$$K_B = 0 \tag{4.13}$$

Cohesion is only modelled between the grains that are in contact in the initial phase of the simulation. Due to the fact that grains are approximated by clumps of overlapping spheres, a particular approach needed to be developed in order to model the elastic brittle contact between individual grains.

Since contact forces are evaluated between individual discrete elements, the cohesive contact between two grains is modelled by creating a set of contacts of appropriate stiffnesses and adhesions between pairs of constituting spheres from the two respective clumps. In order to assure a homogeneous distribution of cohesive forces along the grain contact surface, pairs of contact spheres and contact properties are determined as follows. The discrete binary images of snow (Fig. 4.17.a) are detected from the tomographical image of snow matrix by the segmentation algorithm [Hagenmuller et al., 2014b]. Each of the two adjacent grains is approximated by a set of overlapping spheres, as described in section 4.2.2 (Fig. 4.17.b). Each voxel on the boundary of the respective grain is associated with the closest approximating sphere, i.e. the sphere with the smallest distance between its surface and the voxel in question (Fig. 4.17.c). For each pair of voxels on the boundary between two grains, a contact is created between the two associated spherical discrete elements 4.17.d).

Although contact stiffness and adhesion are automatically determined in YADE (Eqs. 3.24, 3.25, 3.28 and 3.33), these values are overridden in order to insure contact properties that reflect the grain contact surface that the particular sphere contact represents, rather than the size of the two contacting spheres.

Normal contact stiffness of an initial cohesive contact is determined by:

$$K_N = n_i S_{voxel}^2 E, \tag{4.14}$$

where n_i is the number of surface voxel pairs that corresponds to the respective pair of spheres (Fig. 4.17.c) and S_{voxel} is the side length of a voxel with respect to the size of the snow sample. Shear stiffness is related to normal stiffness by Poisson's ratio:

$$K_S = \nu K_N. \tag{4.15}$$

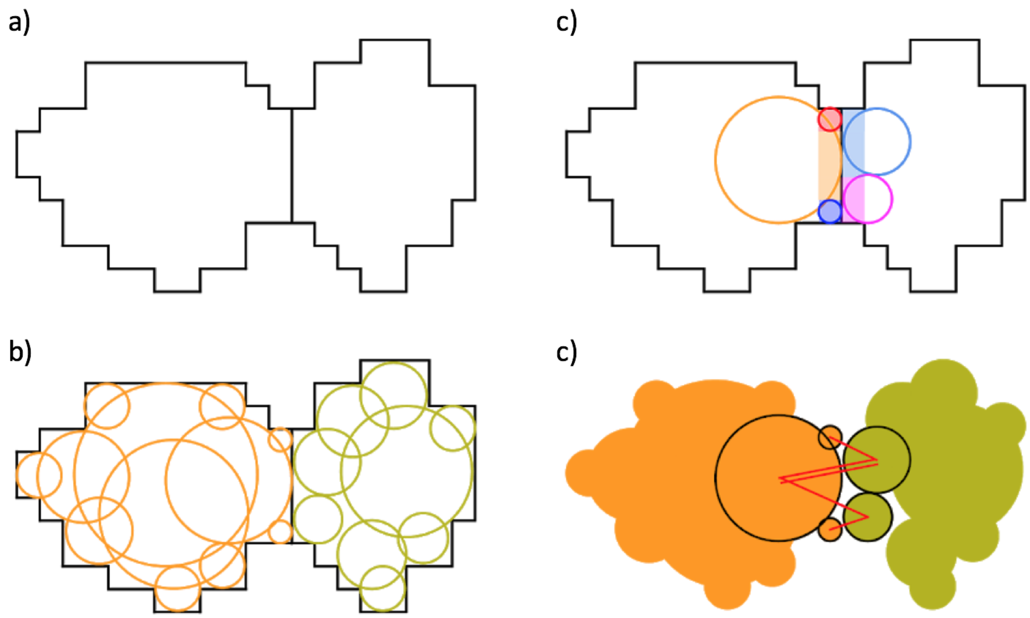

Figure 4.17: The methodology of modelling intergranular cohesion. a) Binary images of two adjacent grains. b) Sphere-based approximation of the two grains. c) Each voxel on the cohesive boundary of the grain is associated with the closest approximating sphere. d) For each pair of voxels on the boundary between two grains, a contact is created between the two associated spherical discrete elements. If more than one pair of voxels in contact corresponds to the same pair of discrete elements, the magnitude of adhesion and stiffness are multiplied accordingly.

Equal normal and shear cohesion is considered. The magnitude of adhesion A_{voxel}, attributed to a pair of voxels in contact is determined by considering the tensile strength of ice ($C_{ICE} = 10^6$ MPa) and voxel side length:

$$A_{voxel} = C_{ICE} S_{voxel}^2. \tag{4.16}$$

If more than one pair of voxels in contact corresponds to the same pair of discrete elements, the magnitude of adhesion is multiplied accordingly (Fig. 4.17.d). Adhesion A_i of a pair of discrete elements i is hence computed in the following manner:

$$A_i = n_i A_{voxel}, \tag{4.17}$$

Due to the nature of the grain approximating process, it is possible that the spherical discrete elements between which the adhesion needs to be applied are not in contact. This needs to be taken into account in order to insure the correct contact force between the two respective discrete elements. By manually setting the value of plastic penetration depth of an adhesive contact to the initial distance between the two discrete elements, equilibrium state is enforced on the initial position of discrete elements.

A directional analysis was performed in order to observe the influence of the loading angle as well as grain approximating parameters on the evolution of the force, needed to break the intergranular cohesion. A simple contact between two half-spherical grains with a planar contact surface (Fig. 4.18.a) was considered and a directional analysis was performed for different realizations of grain approximation. Namely, delete ratio was of particular interest as it controls the density of approximating sphere distribution and with it, the number and direction of cohesive bonds. The grain contact was loaded under different angles, from 0° (pure shear) to 90° (pure tension). The force magnitude is marked by F, the peak force of each individual loading case by F_{max} and the maximum peak force by F_{MAX}. The evolution of normalized force F/F_{MAX} with respect to the second invariant of strain $J_2(\varepsilon)$ is shown in Fig. 4.18.b, and it can be observed that the elastic-brittle behaviour of grain contact is relatively well captured under all loading angles. Figure 4.18.c displays the dependence of the normalized peak force F_{max}/F_{MAX} on the loading angle for three different values of D and a relatively low variation of the normalized peak force insures consistent cohesive contact response under different loading scenarios and approximating realizations.

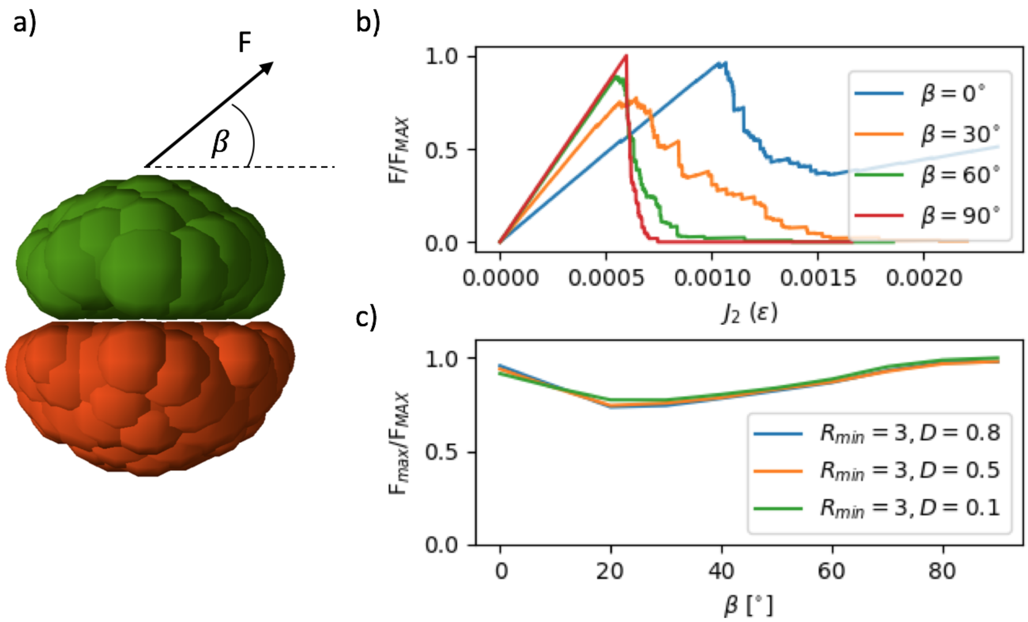

Figure 4.18: a) The directional analysis is performed on the contact between two half-spherical grains. b) Relative force magnitude evolution with respect to the second invariant of the strain tensor. c) Dependency of the relative peak force with respect to the loading angle.

Chapter 5

Mixed-mode loading simulation of snow

Abstract Mixed-mode loading under periodic boundary conditions is applied to the developed DEM model of snow and the three snow samples analysed in the following chapters of this thesis are introduced. The response of a sample of rounded grains (sample s-RG1) is analysed for varying simulation parameter values in order to determine the values of stiffness and density of the grains, shearing velocity, loading rate and timestep, that will insure the validity of the calculated results at a reasonable computational cost for all three snow samples. A sensitivity analysis of the mechanical simulation results with respect to grain approximation parameters is repeated for mixed-mode loading of sample s-RG1. The results of the sensitivity analysis are consistent with those from the oedometric compression: the same values of grain approximation parameters are identified as the optimal and a high correlation between volumetric error of grain approximation and mechanical error of the loading simulation is observed. Volumetric error is thus used in order to predict the mechanical error, and such values of grain approximating parameters are chosen for the two other samples (s-RG2 and s-FCDH), which result in a certain value of volumetric error and will presumably result in a corresponding mechanical precision.

Contents

5.1 Samples

Three samples of snow are considered in this thesis: sample s-RG1 (rounded grain snow, density= 250 kg m^{-3}), sample s-RG2 (rounded grain snow, density= 180 kg m^{-3}) and sample s-FCDH (faceted snow mixed with depth hoar, density= 180 kg m^{-3}) (Fig. 5.1). The snow samples are of cubical shape with a side length of approximately 5 mm.

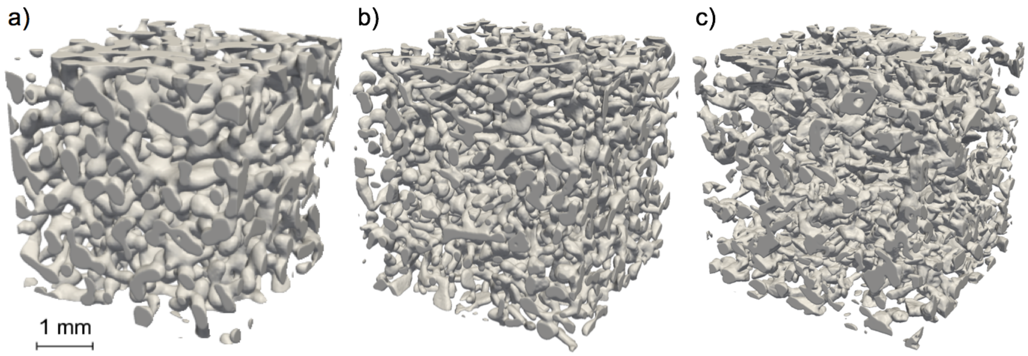

Figure 5.1: Binary segmented X-ray microtomography images of snow samples: a) sample s-RG1, b) sample s-RG2 and c) sample s-FCDH.

5.2 Boundary conditions and loading

Mixed-mode loading is applied to the developed DEM model of snow. A rigid boundary condition is applied to the bottom face and periodic boundary conditions are applied to all four side-faces (Fig. 5.2). The samples are loaded by a combination of a constant shearing velocity v and constant normal stress p applied to the top surface, where the normal stress is applied first and sample is allowed to settle before shearing is applied. The loading on the top surface as well as the rigid boundary condition on the bottom surface are applied by surface DEs of square shape that cover the top and bottom surface of the sample. The rigid boundary condition and the loading are applied directly to the bottom and top surface DEs respectively. In order to insure the transmission of shear loading to the sample, all the grains that form the top surface of the sample are rigidly bound to the top surface DE and the grains that form the bottom surface to the bottom surface DE.

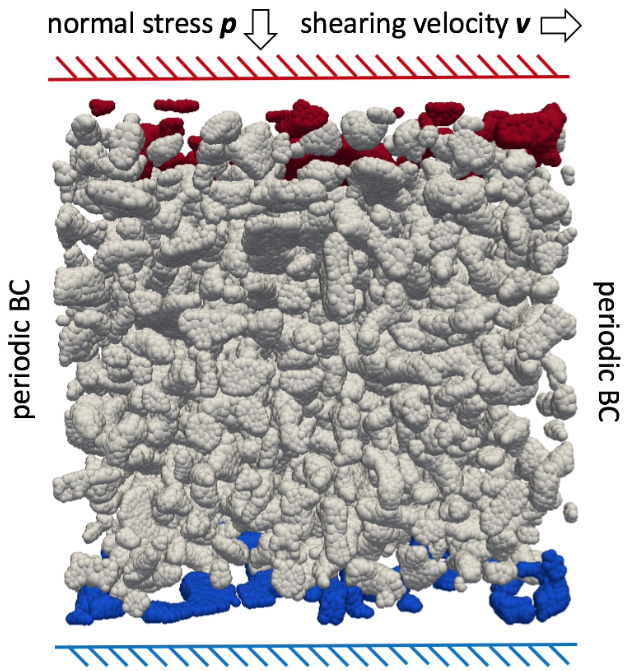

Figure 5.2: Sample of snow and a schematic representation of the boundary conditions. The red coloured grains are fixed to the surface discrete element covering the top surface of the sample, while the blue coloured grains are fixed to the surface discrete element covering the bottom surface of the sample.

The normal stress p is applied with a ramp function in order to avoid inertial effects. Duration of the ramp function Δt_P is defined with respect to the critical timestep of the simulation:

$$\Delta t_P = \alpha \Delta t_{CR}, \tag{5.1}$$

where α is the loading factor and Δt_{CR} is the critical timestep (Eq. 5.5). A sensitivity analysis was performed in order to determine the value of the loading factor that will insure a quasi-static application of normal stress. Mixed-mode loading simulations on sample s-RG1 were performed for five different values of α, while the remaining simulation parameters were kept constant: $v = 10^{-2} ms^{-1}$, $E = 10^8$ MPa, $\rho = 970$ kg m^{-3}, $\lambda = 0.8$, $D = 0.5$ and $R_{min} = 5$ (D and R_{min} refer to grain approximating parameters presented in section 4.2.2). No significant influence of the loading factor on the shear stress response of the snow sample was observed (Fig. 5.3.a). Similarly as in section 4.4.2, Mechanical error E_M of the simulation is introduced as a quantitative measure of accuracy of the simulated mechanical response, by calculating the normalized root mean square error of the simulated shear stress response in question with respect to the reference simulated response. E_M remained very low (Fig. 5.3.b: $E_M < 0.17$) through the entire explored range of loading factor values and the value $\alpha = 100$ has been chosen for the mixed-mode simulations.

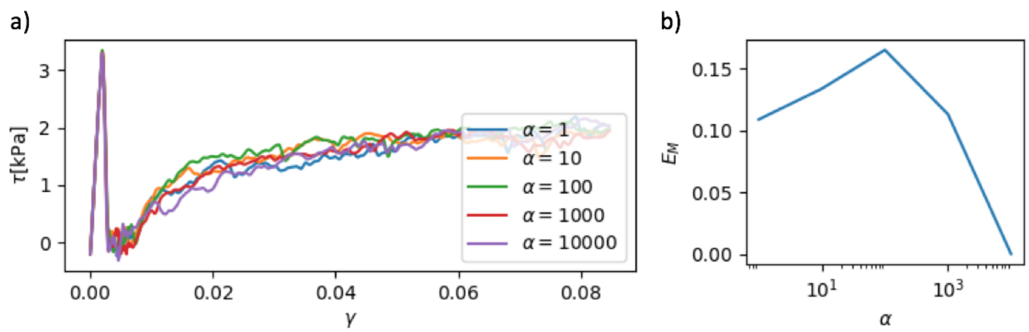

Figure 5.3: a) Shear stress-strain response of mixed-mode loading simulations for the five tested values of α. b) Mechanical error E_M for the five tested values of α.

After the application of normal stress, the sample is allowed to settle and any kinetic energy to die out ($E_K < 10^{-7}$ J), before a constant shearing velocity v is applied to the top surface of the sample. A sensitivity analysis has been performed in order to insure a quasi-static shearing regime i.e. that the stress-strain response is independent of v. Mixed-mode simulations were performed on the snow sample s-RG1 for three different values of shearing velocity: $v = 10^{-3} ms^{-1}$, $v = 5 \cdot 10^{-3} ms^{-1}$ and $v = 10^{-2} ms^{-1}$ (Fig. 5.4.a), while the remaining simulation parameters remained constant: $E = 10^8$ MPa, $\rho = 970$ kg m^{-3}, $\alpha = 100$, $\lambda = 0.8$, $D = 0.5$ and $R_{min} = 5$. E_M was calculated for the performed set of simulations, where result of the simulation with the slowest shearing velocity $v = 10^{-3} ms^{-1}$ was taken as the reference result (Fig. 5.4.b).

The shear stress responses appear highly similar (Fig. 5.4.a) and the mechanical error remains sufficiently low (Fig. 5.4.b: $E_M < 0.3$) in the explored range of shearing velocities. The highest tested shearing velocity $v = 10^{-2} ms^{-1}$ was hence adopted for the mixed-mode simulations.

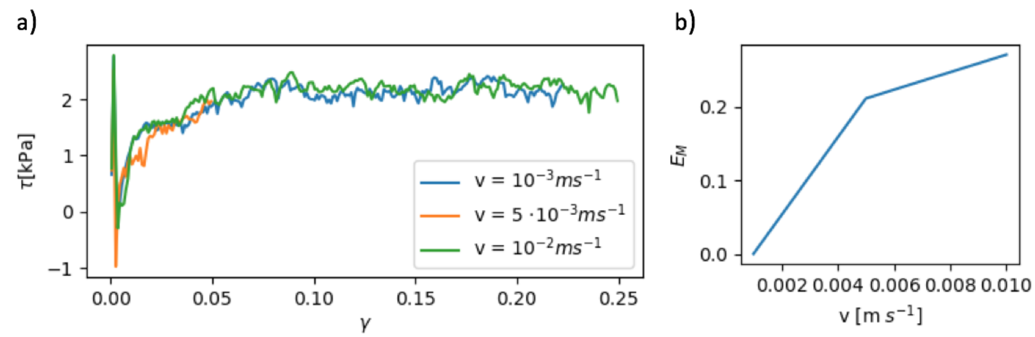

Figure 5.4: a) Shear stress-strain response of mixed-mode loading simulations for the three tested values of v. b) Mechanical error E_M for the three tested values of v.

5.3 Material parameters

5.3.1 Density

The constitutive material of grains in the case of snow is ice, density of which is $\rho_{ICE} = 970$ kg m^{-3}. It was however verified whether the material density can be scaled in order to reduce the computing time of simulations. The approach is valid if the system remains in a quasi-static regime during the course of the simulation (section 3.2). The latter can be evaluated by computing the evolution of the inertial number I Combe and Roux [2009]. Inertial number is a dimensionless parameter that quantifies the significance of dynamic effects in a granular material, by measuring the ratio of inertial forces of grains to imposed forces. Small values ($I < 10^{-3}$) correspond to a quasi-static regime, moderate values ($10^{-3} < I < 10^{-1}$) signify a dense flow and high values ($I > 10^{-1}$) mark a collisional flow. The evolution of I was hence computed for the mixed-mode loading simulation of sample s-RG1 for the following values of simulation parameters: $v = 10^{-2}ms^{-1}$, $E = 10^8$ MPa, $\rho = 970$ kg m^{-3}, $\alpha = 100$, $\lambda = 0.8$, $D = 0.5$ and $R_{min} = 5$. It was observed that the simulated system doesn't persist in a quasi-static state through the entire duration of the simulation due to a dynamic event in the early stage of the simulation (Fig. 5.5), which is further analysed in chapter 5. Consequently, the material density could not be scaled in order to increase critical timestep and the density of ice has to be used to determine the mass of grains in the mixed-mode simulation of snow.

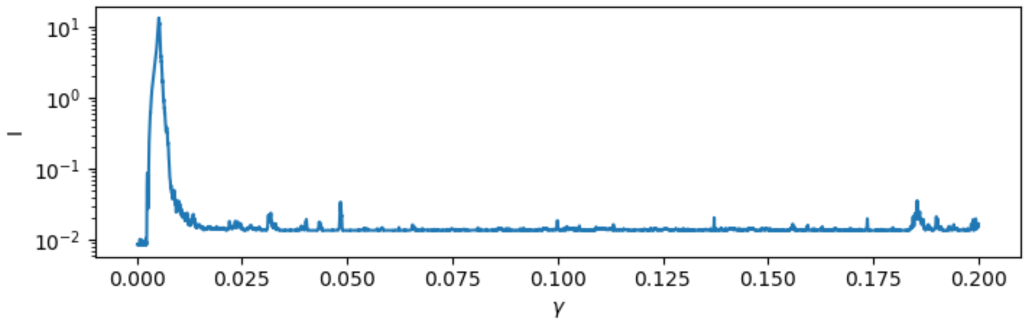

Figure 5.5: Evolution of the inertial number with respect to shear strain during the mixed-mode loading simulation.

5.3.2 Young's modulus

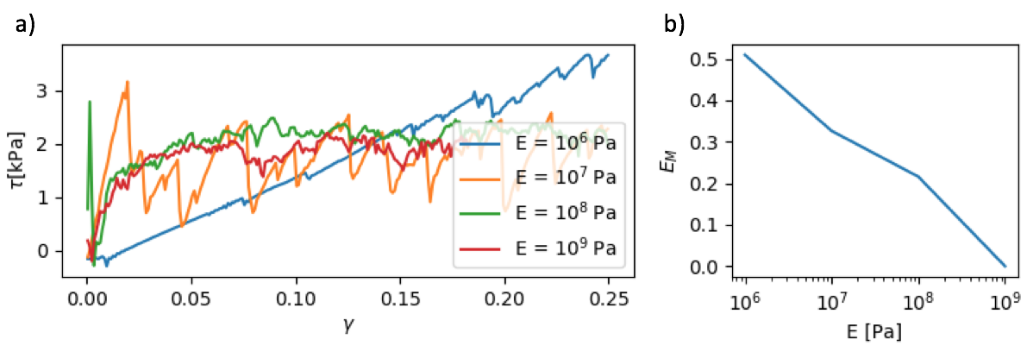

Figure 5.6: a) Shear stress-strain response of sample s-RG1 to simulated mixed-mode loading for the four tested values of E. b) Mechanical error E_M for the four tested values of E.

A sensitivity analysis has been performed in order to observe the influence of Young's modulus on the shear stress response of snow under mixed-mode loading (Fig. 5.6.a). Four different values of Young's modulus were used to perform mixed-mode loading simulations of sample s-RG1, while the remaining parameters of the simulations remained constant: $v = 10^{-2} ms^{-1}$, $\rho = 970$ kg m^{-3}, $\alpha = 100$, $\lambda = 0.8$, $D = 0.5$ and $R_{min} = 5$. Mechanical error of performed simulations has been calculated, where the simulation result for the highest value of Young's modulus $E = 10^9$ MPa was taken as the reference result (Fig. 5.6.b). While the shear stress response for the two lowest values of E differs significantly from the reference simulation, the response at $E = 10^8$ MPa, relatively accurately reproduces the reference stress curve (Fig. 5.6.a). A power law dependence was observed between the E_M and applied E (Fig. 5.6.b). Young's modulus $E = 10^8$ MPa was identified as the optimal value, where the mechanical error is sufficiently reduced to insure sufficient simulation accuracy (Fig. 5.6.a).

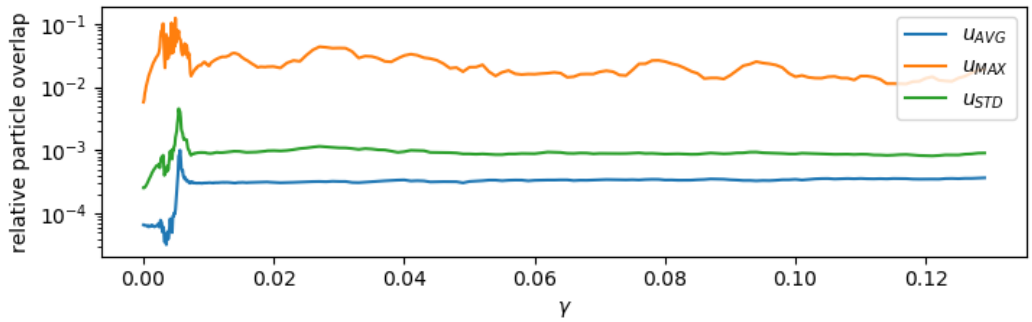

Figure 5.7: Evolution of the average relative particle overlap U_{AVG}, maximum relative particle overlap U_{MAX} and the standard deviation of relative particle overlaps U_{STD} with respect to shear strain.

Particle overlaps were monitored during the simulation, conducted for the value of Young's modulus $E = 10^8$ MPa, in order to verify whether the simulation is performed in the rigid grain limit. Relative particle overlap is defined as the overlap between two discrete elements in contact, divided by the radius of the smaller discrete element of the two. Average relative particle overlap U_{AVG}, maximum relative particle overlap U_{MAX} and the standard deviation of relative particle overlaps U_{STD} were calculated for each timestep of the simulation and are shown in Fig. 5.7. The highest recorded value of U_{MAX} is 0.12, while U_{AVG} stays below $5 \cdot 10^{-3}$ and U_{STD} below 10^{-3}, showcasing that the rigid grain limit is respected.

5.4 Timestep

Critical timestep of DEM simulations is normally calculated by applying Eq. 3.73. The developed DEM model of snow is however based on representing individual grains as clumps, where the dynamic properties of each clump member are computed from the motion of the clump (section 3.1.4). Hence, Eq. 3.73 must be applied to clumps rather than spherical discrete elements. Since the same Young's modulus is applied to all the discrete elements, the equation of contact stiffness Eq. 3.24 simplifies to:

$$K = \frac{Er_1 r_2}{r_1 + r_2}. \tag{5.2}$$

Contact stiffness hence depends on the radii of the two spherical discrete elements in contact. In order for the critical timestep calculations to remain on the safe side, the highest possible contact stiffness for each clump due to potential collisions with other clumps $K_i^{max}(collisions)$ is calculated by considering contact of the largest spherical discrete element in the clump r_i^{max} with the largest spherical discrete element in the simulation R^{max}:

$$K_i^{max}(collisions) = \frac{Er_i^{max} R^{max}}{r_i^{max} + R^{max}}. \tag{5.3}$$

Initial contacts are however not considered in Eq. 5.3. Since the stiffness of the initial contacts has been manually overridden in order to insure an equal effective stiffness of all cohesive contacts (Eq. 4.14), this must be accounted for in the critical timestep calculation. The initial contact with the highest stiffness is identified for each clump and marked $K_i^{max}(initial)$. Finally the highest possible contact stiffness of clump i can be defined as:

$$K_i^{max} = max(K_i^{max}(collisions), K_i^{max}(initial)). \tag{5.4}$$

Equation 3.73, can thus be rewritten in the following form in order to calculate the critical timestep Δt_{CR} of the developed model:

$$\Delta t_{CR} = min\left(\sqrt{\frac{m_i}{K_i^{max}}}\right). \tag{5.5}$$

The timestep of the calculation is obtained multiplying the critical timestep with a reduction factor λ in order to account for integration errors Zhao [2017]:

$$\Delta t = \lambda \Delta t_{CR}. \tag{5.6}$$

The effect of reduction factor on the shear stress-strain response of snow has been observed by performing a sensitivity analysis. Mixed-mode loading simulation of sample s-RG1 has been performed for five different values of λ, while the remaining simulation parameters remained constant:

$v = 10^{-2} ms^{-1}$, $E = 10^8$ MPa, $\rho = 970$ kg m^{-3}, $\alpha = 100$, $D = 0.5$ and $R_{min} = 5$. Negligible changes between the shear stress curves were observed for different values of λ (Fig. 5.8.a). The mechanical error remained sufficiently low for all the tested values of λ (Fig. 5.8.b: $E_M < 0.2$), justifying the choice of the highest tested value of reduction factor $\lambda = 0.8$.

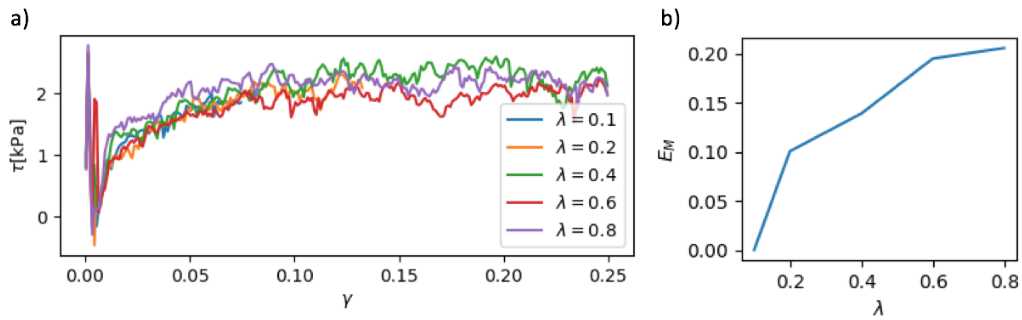

Figure 5.8: a) Shear stress-strain response of mixed-mode loading simulations of sample s-RG1, performed for five different values of reduction factor λ. b) Mechanical error E_M for the five tested values of λ.

5.5 Grain approximation

The choice of grain approximating parameter values has been shown to have a pronounced effect on the accuracy of the mechanical simulation as well as the computation time (section 4.4.2), which increases roughly with a square of the number of spheres used for grain approximation. While the optimal grain approximating parameters have already been determined for the case of oedometric compression of sample s-RG1 (chapter 4), these values of parameters are not necessarily optimal in the case of mixed-mode loading simulation. A sensitivity analysis is therefore performed in order to observe the effect of delete ratio D and minimal sphere radius R_{min} on the shear stress-strain response of sample s-RG1. Simulations were performed for nine different approximating parameter combinations (Table 5.1) while the remaining simulation parameters were kept constant: $v = 10^{-2} ms^{-1}$, $E = 10^8$ MPa, $\rho = 970$ kg m^{-3}, $\alpha = 100$ and $\lambda = 0.8$. The parameter combination A represents the control combination, offering a near-complete reconstruction of grains in terms of all the shape descriptors (section 4.4.1). The volumetric error of grain approximation in this case is of the same order as the volumetric variation of the input tomographical X-ray image Hagenmuller et al. [2016] due to the choice of image processing parameters. Result of the simulation, performed for parameter combination A is hence taken as the reference response.

Parameter combination	D	R_{min}
A	0.2	2
B	0.2	5
C	0.2	8
D	0.5	2
E	0.5	5
F	0.5	8
G	0.8	2
H	0.8	5
I	0.8	8

Table 5.1: Nine approximation parameter combinations, used for the sensitivity analysis of the mixed-mode loading response of sample s-RG1 with respect to grain approximation.

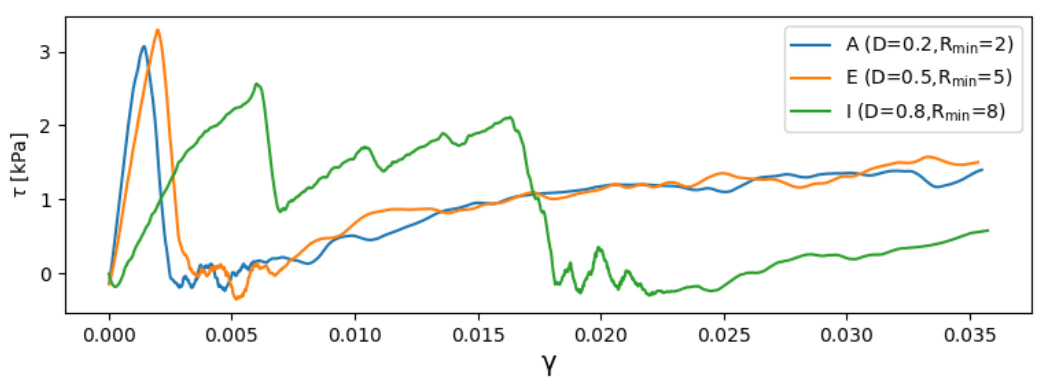

Figure 5.9: Shear stress-strain response of the sample s-RG1 for three different combinations of grain approximating parameters: A ($D = 0.2$ and $R_{min} = 2$), E ($D = 0.5$ and $R_{min} = 5$) and I ($D = 0.8$ and $R_{min} = 8$).

The shear stress-strain response of sample s-RG1 to mixed-mode loading for three different combinations of grain approximating parameters: A ($D = 0.2$ and $R_{min} = 2$), E ($D = 0.5$ and $R_{min} = 5$) and I ($D = 0.8$ and $R_{min} = 8$) is shown in Fig. 5.9. While the mechanical response produced by parameter combination I is far from accurate, the parameter combination E results in a good approximation of the reference result. Figure 5.10.b displays mechanical error of mixed-mode simulations produced by different combinations of grain approximating parameters as a function of the number of spheres used for grain approximation. Similarly as in the case of oedometric compression, a very fast decay of E_M with the number of approximating spheres is observed, enabling a relatively low E_M to be obtained by a reasonably small number of approximating spheres. Equally as in the case of oedometric compression, parameter combination E ($D = 0.5$ and $R_{min} = 5$) was identified as the optimal, delivering relatively accurate mechanical results at an acceptable computational cost.

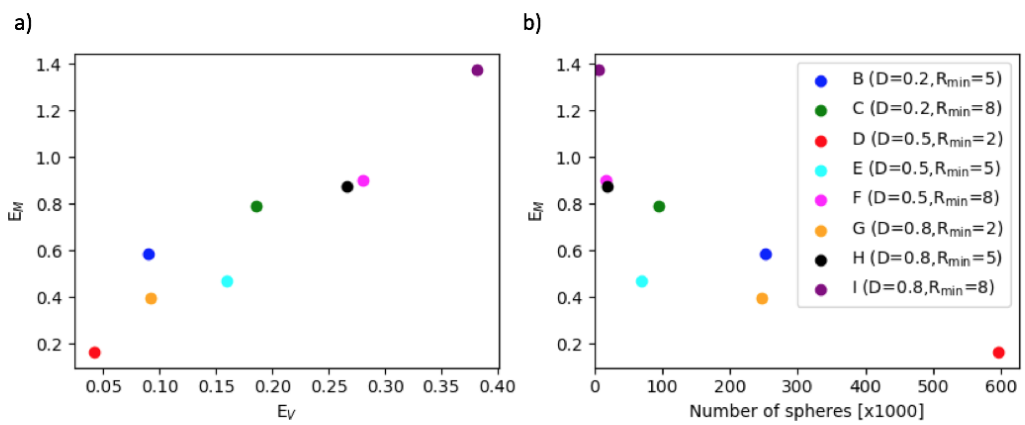

Figure 5.10: a) Mechanical error of the simulated mixed-mode loading responses of sample s-RG1 produced by different combinations of grain approximating parameters with respect to volumetric error. b) Mechanical error of the simulated mixed-mode loading responses of sample s-RG1 produced by different combinations of grain approximating parameters as a function of the utilized number of approximating spheres.

Moreover, similarly as for oedometric compression simulations, a near linear correlation is observed between mechanical error of the mixed-mode simulations and volumetric error due to approximation E_V (Fig. 5.10.a). A regression analysis was performed between E_M and the values of shape descriptors E_V, E_A and E_R (Eqs. 4.5, 4.6 and 4.11). The high p-values for anisotropy $p(E_A) = 0.07$ and surface roughness $p(E_R) = 0.72$ indicate that there is no statistically significant correlation between these two shape descriptors and the mixed-mode loading stress response of the snow sample s-RG1. On the other hand, the p-value for the volumetric error $p(E_V) = 2.5 \cdot 10^{-4}$ rejects the null hypothesis and indicates a strong correlation between this shape descriptor and the mechanical error of the simulation.

Since E_M of oedometric as well as mixed-mode loading simulations was shown to be strongly correlated to E_V in the case of snow sample s-RG1, E_V was used as a tool to determine the optimal values of grain approximating parameters for snow samples s-RG2 and s-FCDH, without performing the time-consuming mechanical sensitivity analysis. The approximating parameters that produce the same value of E_V are presumed to result in the same level of mechanical accuracy.

The values of grain approximating parameters for samples s-RG2 and s-FCDH were hence determined in the following manner. A subset of 10 grains was taken from the respective snow sample and used in order to calculate E_V (Figs. 5.11.a and 5.12.a). Since $E_V = 0.15$ was identified as the volumetric error of the optimal approximation in the case of sample s-RG1, approximating parameters were sought to reproduce this value of E_V for the respective sample. Among the multiple combinations of D and R_{min}, that result in $E_V = 0.15$, the parameter combination that results in the minimum number of approximating spheres (Figs. 5.11.b and 5.12.b) was chosen as the optimal one. In the case of sample s-RG2, the combination $D = 0.4$, $R_{min} = 5$ was identified as the optimal and resulting in 79947 spheres, while in the case of sample s-FCDH, the chosen parameter values were $D = 0.4$, $R_{min} = 4$ which result in 272587 approximating spheres.

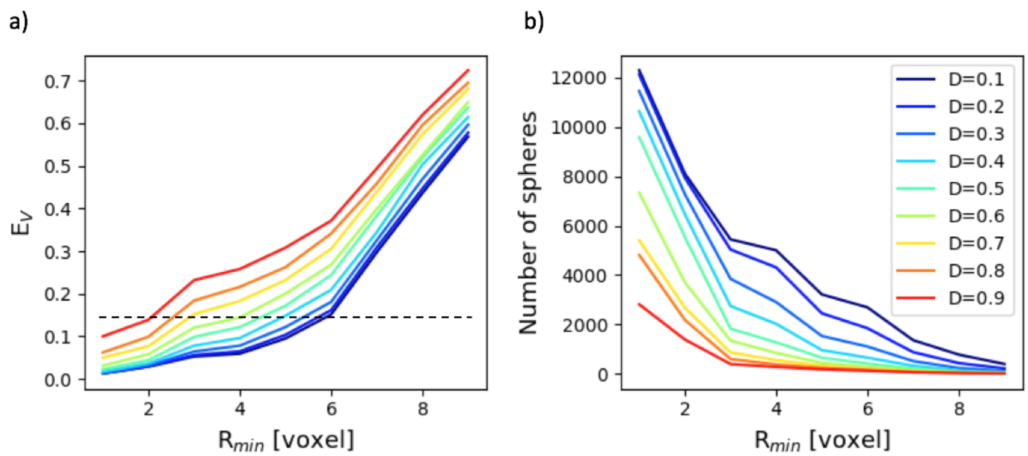

Figure 5.11: a) Volumetric error of a subset of 10 grains, obtained from snow sample s-RG2, with respect to the values of the two grain approximating parameters. Dashed line marks the value of E_V used to determine the optimal values of D and R_{max}. b) Number of spheres used for approximation of a sub-sample of 10 grains, obtained from snow sample s-RG2, with respect to the values of the two grain approximating parameters.

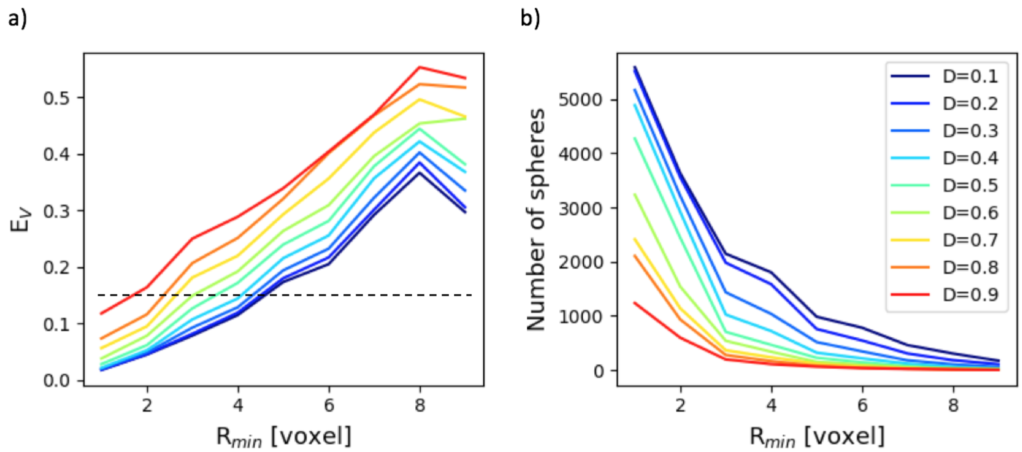

Figure 5.12: a) Volumetric error of a subset of 10 grains, obtained from snow sample s-FCDH, with respect to the values of the two grain approximating parameters. Dashed line marks the value of E_V used to determine the optimal values of D and R_{max}. b) Number of spheres used for approximation of a sub-sample of 10 grains, obtained from snow sample s-FCDH, with respect to the values of the two grain approximating parameters.

5.6 Conclusions

Mixed-mode loading under periodic boundary conditions was applied to the developed DEM model of snow. A meticulous procedure was applied in order to determine the simulation parameter values that will insure stable simulations and accurate results at a reasonable computational price. The latter is particularly important as the resulting computational time on an Intel(R) Xeon(R) 2.20GHz processor for the chosen values of parameters varies between 1 day for the sample s-RG1 and several weeks for the sample s-FCDH. With the exception of grain approximating parameters, all the simulation parameters were determined on the basis of sensitivity analyses performed on sample s-RG1 and then applied for all three samples. Finally, the values of parameters, that are to be used in the mixed-mode simulations are summarized for each sample separately in Table 5.2.

It is also important to note that the performed sensitivity analysis of the mechanical error of mixed-mode loading simulations with respect to grain approximating parameters is consistent with the observations from section 4.4.2. A low correlation has been observed between grain anisotropy error and grain surface error respectively and mechanical error of the simulation. The latter was shown to be highly correlated to volumetric grain error, indicating that volumetric grain error could be used to predict the mechanical error of the simulation. While this assumption was shown to be valid under oedometric as well as mixed-mode loading for sample s-RG1, it is yet to be validated on different samples, before its generality can be assumed. Nevertheless, the given assumption was used in order to determine the grain approximating parameters for samples s-RG2 and s-FCDH.

Parameter	sample s-RG1	sample s-RG2	sample s-FCDH
α	100	100	100
v	10^{-2} m s^{-1}	10^{-2} m s^{-1}	10^{-2} m s^{-1}
ρ	970 kg m^{-3}	970 kg m^{-3}	970 kg m^{-3}
E	10^8 MPa	10^8 MPa	10^8 MPa
λ	0.8	0.8	0.8
D	0.5	0.4	0.4
R_{min}	5	5	4

Table 5.2: Mixed-mode loading simulation parameters for all three snow samples.

Chapter 6

Snow failure modes under mixed loading

Abstract The mechanical response of snow to mixed-mode shear and normal loading is the key ingredient for snow avalanche modelling, and strongly depends on microstructural characteristics. A discrete element numerical model was developed, that enables the simulation of large-strain response of snow samples directly described by their full microstructure obtained through X-ray microtomography. The model offers new insights into the failure mechanism as well as post-failure response of snow in mixed-mode loading. Three distinct failure modes are identified, depending on the value of applied normal stress. Above a certain threshold normal stress, the failure is characterized by a structural collapse that decomposes the snow sample into a set of cohesionless grains. It is shown that the collapse is a dynamic process which, once initiated, develops independently of shearing. This behaviour was consistently observed for different snow types, including faceted crystals typically composing weak layers.

Contents

6.1 Introduction

Dry snow slab avalanches represent a severe natural hazard in mountainous regions and are very difficult to predict. They are released by a failure in a mechanically weaker layer of snow, underlying a cohesive slab [Schweizer et al., 2003]. The weak layer consists of particular snow types, such as precipitation particles, faceted crystals, depth hoar and surface hoar [Jamieson and Johnston, 1992], often characterized by very low strengths. On a slope, this layer of snow is loaded in combined shear and compression, the so-called mixed-mode loading, by the weight of the overlying snow and potential additional perturbations (skiers, animals etc.). If the loading locally exceeds the weak layer strength, a failure occurs and can propagate along the slope as an anticrack [Heierli et al., 2008; Gaume et al., 2017b]. The loss of basal support results in an increase in tensile stresses within the slab and can eventually lead to a crown fracture and the release of a snow avalanche. Both the propagation of the anticrack in the weak layer and the release of the slab avalanche crucially depend on snow failure and collapse characteristics under mixed-mode loading [Gaume et al., 2018], which however remain poorly understood [Schweizer et al., 2016].

In the pre-failure stage, the elastic properties of snow have been subject to numerous experimental investigations [Mellor, 1974; Narita, 1980; Gerling et al., 2017b], and were shown to be controlled by density as well as microstructural anisotropy. Failure of snow is generally considered to be governed by the Mohr-Coulomb criterion [McClung, 1977; Fyffe and Zaiser, 2007; Chiaia et al., 2008; Gaume et al., 2014], where the shear strength increases linearly with the normal load. However the application of this failure criterion to weak layers is questionable. Recent experimental campaigns have shown that weak layers feature closed failure envelopes [Chandel et al., 2014a; Reiweger et al., 2015], which deviate from Mohr-Coulomb linear model at high levels of normal stresses and account for failure in pure compression. On the other hand, the post-failure mechanical behaviour of snow, including strain softening and progressive transition towards residual stress remains largely unexplored [McClung, 1977; Fyffe and Zaiser, 2007]. In addition, the mechanical response of weak layers is generally thought to be qualitatively different from that of other snow types, with a significant collapse at failure [Van Herwijnen et al., 2010]. This normal collapse has been proven to have an important effect on the bending and fracture of the slab [Gaume et al., 2017b]. The conditions under which this collapse occurs, as well as its relation to failure and strain softening, remain open issues [Reuter and Schweizer, 2018].

The extremely low strength of weak layers and their sensitivity to environmental conditions render systematic experimental exploration difficult and complicate observation at the microscopic level. As an alternative to experiments, numerical approaches have been developed in the recent years to model snow mechanical response by accounting for microstructure [Hagenmuller et al., 2015; Wautier et al., 2015; Srivastava et al., 2016; Gaume et al., 2017a; Gerling et al., 2017b]. These approaches enable the simulation of the macroscopic response of snow to mechanical loading from simple constitutive relations between snow particles at the microscopic scale. These approaches also offer the capacity to perform multiple loading simulations on the same sample, along with the perfect control over boundary conditions and access to all relevant descriptors.

The objective of the present study is to gain a deeper understanding of the mechanical response of snow to mixed-mode loading, using a microstructure-based numerical approach. Development of a specific discrete element model allows us to perform systematic large-strain shearing simulations on different snow types. We consider a regime in which snow deformation is dominated by inter-granular damage and grain rearrangement and therefore model snow grains as unbreakable entities [Johnson and Hopkins, 2005; Hagenmuller et al., 2015]. This regime is typical of the relatively high deformation rates involved in the release of snow avalanches, which are well above the rate of transition from ductile to brittle behaviour of snow [$\dot{\gamma} > 10^{-4}$ s^{-1}, Narita, 1980]. Accordingly, viscous effects at contacts and grain sintering are not considered in the model.

6.2 Methods

The present study exploits an original numerical approach, based on the discrete element method (DEM) [Cundall and Strack, 1979], which has been developed in order to simulate the mechanical response of snow samples to external loading [Hagenmuller et al., 2015; Mede et al., 2018a]. The model takes X-ray microtomography images of snow as input information. First the X-ray attenuation images are segmented into pore space and a continuous ice matrix [Hagenmuller et al., 2013]. The ice structure itself is then segmented into individual grains by detecting potential weak points based on local geometrical criteria [Hagenmuller et al., 2014b]. For the sake of computational efficiency, the actual shape of every grain in DEM simulations is modelled by packing the volume of the grain with a set of overlapping spherical discrete elements [Mede et al., 2018a]. There is a trade-off between the grain approximation accuracy (and consequently the mechanical simulation accuracy) and the number of utilized spherical discrete elements (and consequently the numerical cost of the simulation). The optimal level of approximation was determined by a comprehensive sensitivity analysis of the macroscopic simulated response of a snow sample to compressive [Mede et al., 2018a] as well as shear loading. These approximated grains are spatially arranged according to the initial microstructure. Grains are assumed to be unbreakable and are bonded by elastic brittle cohesion with the neighbouring grains at the locations where the image has been segmented (Fig. 6.1).

Considered snow samples are of cubical shape with a side length of approximately 5 mm. A rigid boundary condition is applied to the top and bottom faces, while a periodic boundary condition is applied to all four side-faces (Fig. 6.1). The samples are loaded by applying a constant shearing velocity $v = 1$ cm s^{-1} and constant normal stress p to the top surface, while keeping the bottom surface fixed. The normal stress is applied first with a ramp function. A time delay is then imposed before shearing is applied in order for existing kinetic energy within the sample to dissipate. It has been verified that the applied shear rate is low enough to ensure a quasi-static shearing regime, i.e. that the stress-strain response is independent of v. Series of simulations were performed under different values of normal stress p, ranging from -5 kPa to 10 kPa. The simulations were stopped once the shear strain reached the value $\gamma = 0.05$.

Three different snow samples [Mede, 2018] are considered in this study: sample s-RG1 (rounded grain snow, density= 250 kg m^{-3}), sample s-RG2 (rounded grain snow, density= 180 kg m^{-3}) and sample (faceted snow mixed with depth hoar, density= 180 kg m^{-3}). After the segmentation process, roughly 1500 grains are identified in each sample. The choice of these samples allows us to compare the response obtained with the same snow type and different densities (samples s-RG1 and s-RG2), as well as the response obtained with the same density and different snow types (samples s-RG2 and s-FCDH).

The simulations were performed with DEM solver YADE [Šmilauer et al., 2010]. The initial cohesive frictional grain contacts are modelled using a cohesion $C = 10^6$ Pa and Young's modulus $E = 10^8$ Pa. It has been verified that simulations are performed in the rigid grain limit [Cundall and Strack, 1979; Da Cruz et al., 2005]. The non-cohesive contacts created by grain rearrangement are modelled as elastic frictional with the same stiffness. Contact friction coefficient $\mu = 0.2$ was fixed according to typical ice values [Hagenmuller et al., 2015]. A Cundall's non viscous damping coefficient 0.02 was applied. Gravity is not taken into account as it has a negligible effect on the response of the samples compared to external loading. Lastly, the mass of each grain was derived from the original binary image. Due to volumetric errors induced by grain approximation [Mede et al., 2018a], this results in an effective density typically increased by 15% compared to that of ice.

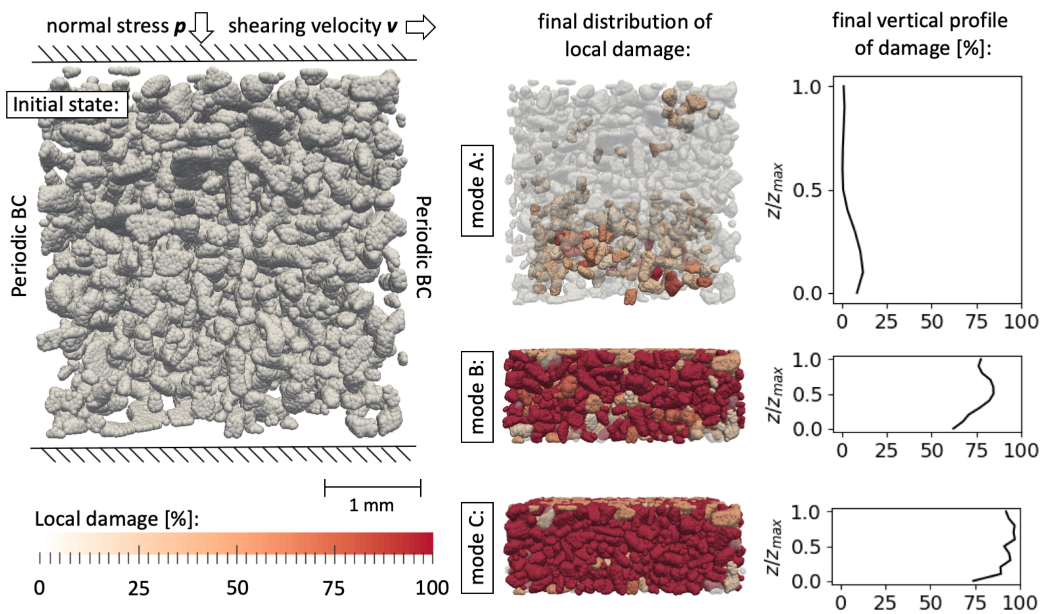

Figure 6.1: Snapshots of mixed-mode loading simulations, applied to sample s-RG1. Image on the left represents the intact sample, along with the boundary conditions. The three rows of images on the right represent the response of the sample under failure modes A ($p = 1$ kPa), B ($p = 4$ kPa) and C ($p = 9.5$ kPa) respectively. Grains with a local damage level below 10% (resp. above 10%) are represented as semi-transparent (resp. with a red colour scale according to the level of damage). The plots on the right represent averaged vertical damage profiles in the three failure modes.

6.3 Results

Snapshots of snow sample s-RG1 submitted to mixed-mode loading under varying normal stresses are presented in Fig. 6.1 and the macroscopic response of the sample is shown in Fig. 6.2. Qualitatively very similar response was observed for samples s-RG2 and s-FCDH. Local damage is defined for each grain as the ratio of broken cohesive bonds with the neighbouring grains, whereas the global damage represents the total ratio of broken cohesive bonds in the sample. In general, three qualitatively different modes of failure can be observed:

Failure mode A: at low normal stresses (for sample s-RG1, $p < 2$ kPa), a quasi-elastic shear stress build-up is followed by a peak (Fig. 6.2.a). The post-peak response is marked by progressive strain softening, which eventually stabilizes at a certain level of residual stress. Concurrently the normal strain remains almost constant (Fig. 6.2.b), although a gradual compaction of the sample can be observed at the highest levels of normal stress in this mode. Failure initiation, marked by the stress peak, appears at a very low level of global damage (typically less that 2%, Fig. 6.2.c). The snow specimen fails along a narrow horizontal band, where all the damage is concentrated (Fig. 6.1), while the rest of the specimen remains largely intact.

Failure mode B: at moderate normal stresses (for sample s-RG1, 2 kPa $\leq p <$ 9 kPa), the peak shear stress is followed by rapidly vanishing shear stress (Fig. 6.2.a). After this abrupt drop, the shear stress slowly increases and eventually stabilizes at the level of residual stress. The vanishing stress is accompanied by a dramatic vertical collapse (Fig. 6.2.b) and a burst of damage (Fig. 6.2.c). During the collapse the snow specimen is almost completely decomposed into a set of cohesionless grains (Fig. 6.1). The onset of normal collapse appears to be progressively delayed with decreasing normal stress, consistently with a prolonged quasi-elastic phase.

Failure mode C: at high normal stresses (for sample s-RG1, $p \geq 9$ kPa), no quasi-elastic response is observed as the sample already fails and collapses during the normal loading phase (Fig. 6.1), resulting in a high level of damage. Upon application of shearing, shear stress gradually increases to residual stress level, whereas the normal strain and damage level remain essentially constant (Fig. 6.2).

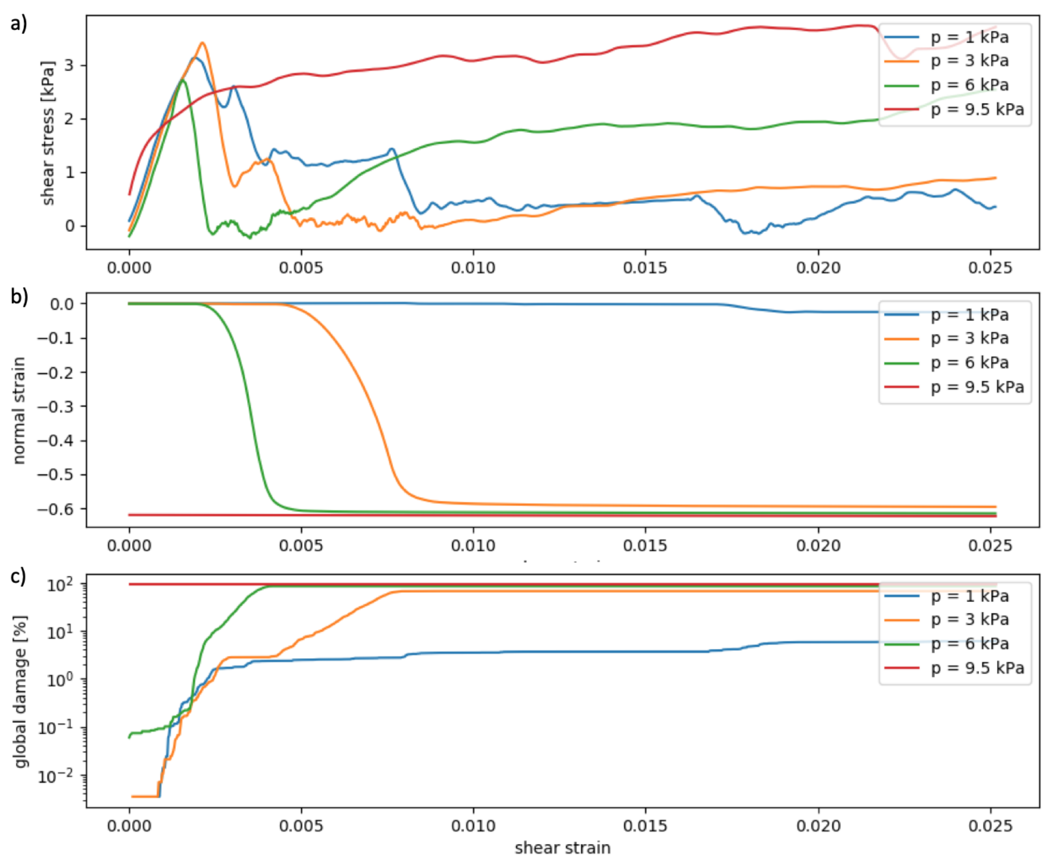

Figure 6.2: a) Shear stress, b) normal strain and c) global damage (in log scale) as a function of shear strain in snow sample s-RG1 during the mixed-mode loading simulations for four different values of normal stress: $p = 1$ kPa, $p = 3$ kPa, $p = 6$ kPa and $p = 9.5$ kPa.

The relation between failure and normal collapse in mode B was additionally explored by separate simulations (Fig. 6.3), in which shear rate was stopped at different values of shear strain and the sample was let to evolve under constant normal stress. The shear rate was stopped with a ramp function to avoid inertial effects caused by the deceleration of the top surface. It was observed that if the shearing is stopped immediately after the shear stress peak, the normal collapse spontaneously develops in the same manner as if the shearing was kept constant (orange curves on Figs. 6.3.b and 6.3.d). At failure the snow specimen enters a dynamic phase, where the collapse is driven by time rather than strain. A steep rise of the kinetic energy takes

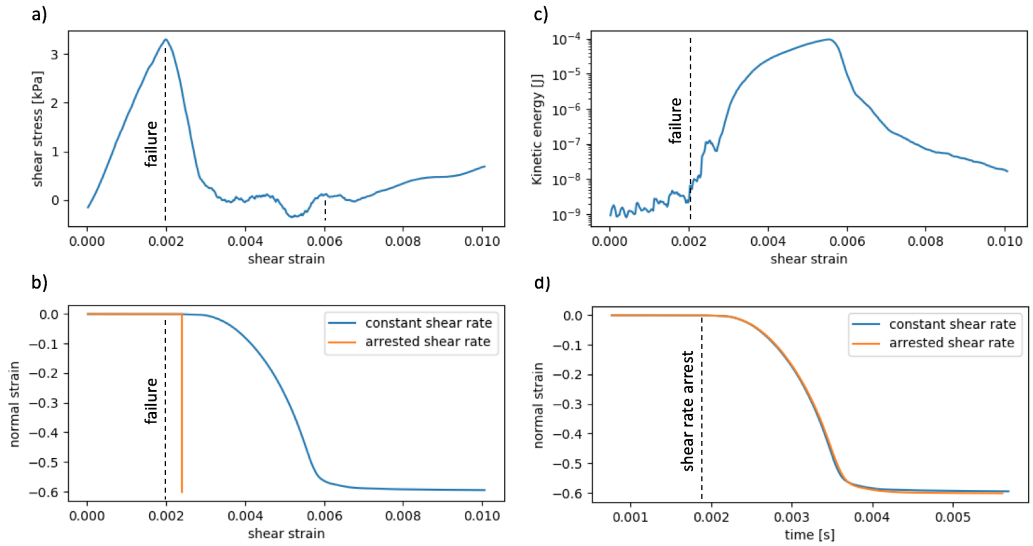

Figure 6.3: Response of the snow sample s-RG1 under mode B failure ($p = 4$ kPa): a) shear stress with respect to shear strain; b) normal strain with respect to shear strain ; c) kinetic energy with respect to shear strain; d) normal strain with respect to time. In c) and d) the blue curve refers to the simulation where the shear rate was constant and the orange curve to the simulation where the shearing was stopped just after the stress peak (see text).

place immediately after the stress peak (Fig. 6.3.c), marking the start of a dynamical processes well before substantial normal strain can be observed.

Figure 6.4 summarizes the response of the three simulated snow samples with respect to the level of applied normal stress. Failure envelopes (Fig. 6.4.a) are defined based on the stress values recorded at the initial shear stress peak. The obtained failure envelopes display similar closed shapes for the three samples, with shear failure stress diminishing to zero at sufficiently low or sufficiently high normal stress. The decrease of failure shear stress at sufficiently large normal stress is a consequence of sample collapse. Note that the maximum of the failure envelopes roughly coincides with the onset of failure mode B and sample collapse (marked by the dotted vertical lines on Fig. 6.4.a). The following linear-elliptic parametrization was found to provide a good fit for the failure envelopes (Fig. 6.4.a):

$$\tau = \begin{cases} \frac{\tau_T}{p_0} p + \left(\tau_T - \frac{\tau_T p_T}{p_0} \right), & \text{if } (p_T - p_0 \leq p \leq p_T) \\ \sqrt{\tau_T^2 - \frac{\tau_T^2}{p_0^2} \left(p - p_T \right)^2}, & \text{if } (p_T < p \leq p_T + p_0) \\ 0, & \text{otherwise,} \end{cases} \tag{6.1}$$

where τ is the shear stress, p is the normal stress and p_0, τ_T and p_T are three parameters. Least square fitting was used to obtain the value of the parameters for each sample (Tab. 6.1).

sample	failure envelope parameters			residual friction
	p_0	τ_T	p_T	
s-RG1	7.00	3.53	1.49	0.49
s-RG2	2.33	1.22	0.19	0.46
s-FCDH	1.45	0.61	0.17	0.59

Table 6.1: Parameter values for the failure envelope parametrization and residual friction coefficients for the three tested samples.

For the three samples, the residual shear stresses appear to follow a common linear trend as a function of normal stress, consistent with a Mohr-Coulomb relation, as expected for a cohesionless granular material. Obtained values of the residual friction coefficients for the three samples vary between 0.49 and 0.59 (Tab. 6.1).

Figure 6.4.b displays the global damage of the three samples at the point of failure. It must be noted that the results are displayed only for failure modes A and B, since failure in mode C is already triggered before shearing is applied. Noteworthy are the extremely low levels of global damage necessary to trigger failure, which remain below 2% for all three samples through the entire range of normal stresses. It also appears that the level of damage at failure is roughly constant throughout the normal stress domain.

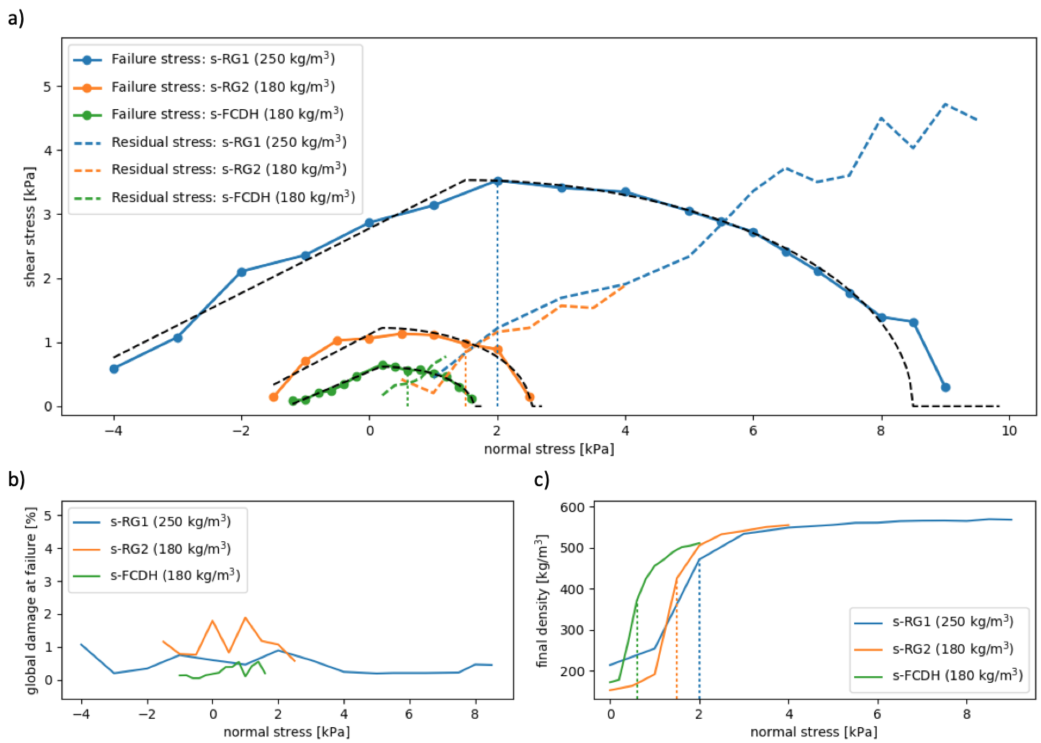

Figure 6.4: a) Failure envelopes and residual stresses for the three different samples: s-RG1, s-RG2 and s-FCDH. Failure envelope parametrizations according to Eq. 6.1 are shown in dashed black lines. b) Damage at failure as function of normal stress for the three samples. c) Final sample density with respect to applied normal stress. The dotted vertical lines in images a) and c) mark the threshold normal stress, above which a collapse is observed (failure mode B).

Figure 6.4.c exhibits the final sample density with respect to the applied normal stress. At low normal stresses, in the absence of collapse, the density of the samples is not substantially changed during shearing and the final density is heavily influenced by the initial microstructure. As the normal stress increases, the final density increases rapidly. Above the collapse threshold stress, the curve slopes start diminishing and all three curves seem to converge towards a unique value independent of normal stress, consistent with the decomposition of the initial microstructure into a cohesionless assembly of grains.

6.4 Discussion and conclusions

DEM simulations conducted in this study offer a unique insight into the failure of snow under mixed-mode shear and normal loading. Three distinct failure modes were identified: a shear failure without normal collapse at low levels of normal stress (mode A); a normal collapse, initiated by shear that takes place at moderate levels of normal stress (mode B); and a normal failure and collapse that take place at high levels of normal stress (mode C). In mode B, sample failure is triggered by extremely low levels of global damage due to combined shear and normal loading. The normal collapse is accompanied by a burst of global damage and nearly completely disintegrates the sample. This normal collapse was shown to be a dynamic event that, once initiated, spontaneously develops independently of shearing. In this mode, apparent post-peak softening of the stress is intimately coupled to sample collapse. Shear stress temporarily drops to zero and the process is time- rather than strain-controlled. In other words, the post-failure behaviour in case of collapse should be seen as the response to a boundary value problem rather than an intrinsic constitutive feature of the material. This may have important consequences for the modelling of collapse wave propagation in slab avalanche release [Gaume et al., 2018].

A consistent macroscopic response was observed for the three tested types of snow, one of which is typical of persistent weak layers (faceted snow). The fact that identical failure modes are observed for all three samples appears to contradict the idea that the mechanical response of weak layers qualitatively differs from other snow types. In particular, according to the performed numerical experiments, the normal collapse, which has hitherto been associated with weak layers [Van Herwijnen et al., 2010], seems to be a general failure characteristic of snow, provided that normal stress is sufficient to activate failure mode B or C.

Due to their collapsible character, the three tested snow samples all feature qualitatively similar, closed failure envelopes. Nevertheless, quantitative discrepancies between the three simulated failure envelopes are observed. On one hand, the differences observed between samples s-RG1 and s-RG2, which correspond to the same snow type with different densities, confirm the well established positive correlation between the snow density and its ultimate strength [McClung, 1977; Narita, 1980]. On the other hand, the differences between the samples s-RG2 and s-FCDH, which have the same density but consist of different snow types, suggests a non-negligible effect of other microstructural characteristics of snow on its ultimate strength. This result is consistent with various experimental investigations, indicating that microstructure plays an important role in determining the mechanical properties of snow [Keeler and Weeks, 1968; Narita, 1980].

Results showed that an extremely low level of damage is sufficient to trigger sample failure, which underlines the extremely fragile character of snow. Furthermore, this damage level seems to be completely independent of the applied normal stress. Note that although small, the sample size considered in this study has been shown to result in a representative mechanical response in the case of simulated large strain compression [Hagenmuller et al., 2015] on samples s-RG1 and s-FCDH. Additionally, the size of these two samples was proven sufficient to estimate the minimum cut density [Hagenmuller et al., 2014a], which is related to the minimal damage needed to break the sample. We can thus argue that this sample size is also sufficient to monitor representative damage evolution under mixed-mode loading.

As a preliminary validation of the model, we can note a good qualitative agreement with the currently available experimental results in several respects: (1) Experimentaly obtained weak layer failure envelopes and typical stregth values (in the range 1-10 kPa) [Chandel et al., 2014a; Reiweger et al., 2015] appear very similar to those presented in this paper. (2) The volumetric collapse at failure observed in this study is well documented in weak layers by in situ [Van Herwijnen et al., 2010] as well as laboratory measurements [Reiweger and Schweizer, 2013]. (3) The derived values of residual friction coefficients are in agreement with those obtained from field tests (between 0.5 and 0.7) [Van Herwijnen and Heierli, 2009]. Finally the extremely low levels of damage observed at peak strength are also consistent with results obtained by Hagenmuller et al. [2014c], using tensile FEM simulations on X-ray microtomography snow images. Hence, the developed numerical model indeed appears to represent a useful tool to investigate failure and post-failure behaviour of snow, including weak layers. Direct quantitative comparisons with experiments are currently not possible since a detailed characterization of the snow microstructure, needed as input for the developed model, is not supplied with available experimental results.

Recent advances in the constitutive modelling of snow and the use of Material Point Method showcase promising perspectives for the simulation of snow avalanche release [Gaume et al., 2018]. The results obtained with the DEM approach proposed here, clearly confirm the assumption of closed failure envelopes made in the latter study. In the future, exciting progress in the multiscale problem of simulating large-scale avalanches from the microstructure, are expected by better connecting the continuum mechanics models to material parameters derived from X-ray tomography images.

Chapter 7

A microstructural investigation of snow failure under mixed-mode loading

Abstract An intimate understanding of snow failure, particularly under mixed-mode shear and normal loading, is a key ingredient for numerical modelling of snow avalanche release. The failure of snow can result in a volumetric collapse, which is possible due to its highly porous structure. The resulting anticrack propagation has been shown to have a key influence on the dry slab snow avalanche release. Despite its importance, snow failure and collapse remain poorly understood, mainly due to the fragile nature of snow, which renders systematic experimental exploration difficult and complicates observation at the microscopic level. A microstructure-based discrete element model of snow has been developed and utilized to study snow failure under mixed-mode loading. Three distinct failure modes are identified and the volumetric collapse is observed to depend on the value of applied normal stress. A deeper understanding of the mechanisms that lead to the volumetric collapse is sought on the microscale. Force chain buckling and collapse within the snow sample are shown to lead to volumetric collapse, while stable force chains result in a localized failure and the absence of a volumetric collapse. It is however the grain contacts between force chains and surrounding material that insure the stability of the force chains. A high ratio of these grain contacts close to failing is identified to have the decisive influence on whether or not the snow failure results in a volumetric collapse.

Contents

7.1 Introduction

The concept of failure is somewhat elusive when it comes to geomaterials, but globally speaking, it could be defined as the state corresponding to an ultimate load, beyond which the system cannot sustain any larger loads [Wan et al., 2017]. Conventionally, the analysis of failure in geomaterials is based on the Mohr-Coulomb criterion which restricts the possible stress states to lie within a plastic limit surface, where unlimited strains can occur under constant stress through a plasticity flow rule [Terzaghi, 1951]. However instances of failure occurring well inside the plastic flow limit have been observed [Lade, 1992].

A more general approach to material failure can be found in Hill's second-order work criterion [Hill, 1958], which indicates the existence of an unstable mechanical state that, under suitable loading conditions, can lead to an effective failure. Recent studies have shown that the second-order work can succesfully detect developing material instabilities characterized by an outburst of kinetic energy [Nicot et al., 2009; Daouadji et al., 2011; Wautier et al., 2017] and is nowadays widely considered a fundamental building block of material failure theory [Wan et al., 2017].

While the second-order work criterion relates the onset of material instability to the evolution of macroscopic stress-strain state, the mechanism of failure can also be observed on the microscale. The overall behaviour of granular materials has been shown to rely on a limited number of grains, organized in linear columns referred to as force chains [Drescher and De Jong, 1972; Radjai et al., 1998; Cambou et al., 2013]. These force chains are transferring forces through the granular assembly [Nicot et al., 2017] and the macroscopic material stability is closely related to the stability of force chains. Tordesillas et al. [2009] have shown macroscopic strain softening is associated to force chain buckling. Recently, it has also been shown that an incremental stress loading leading to the vanishing of the macroscopic second-order work provokes the unjamming of force chains, which results in their bending accompanied by an increase in the kinetic energy [Wautier et al., 2018].

Snow is a somewhat specific geomaterial due to its high porosity and high homologous temperature. Despite it being a key ingredient for numerical modelling of snow avalanche release, our understanding of snow failure remains relatively limited [Schweizer et al., 2003]. Among the different types of snow avalanches, dry slab avalanches are known for their destructive force and complex release mechanism. Generally speaking, they are triggered by a failure in a weak layer of snow, underlying a cohesive slab on a slope [Jamieson and Schweizer, 2000]. This withdraws the support to the overlying slab, increasing the slab tensile forces, which can lead to a tensile crack in the slab and the release of a snow avalanche [McClung, 1987]. Weak layer failure that releases a dry slab avalanche typically occurs under mixed-mode shear and normal loading, provided by the weight of the overlying slab (as well as potential additional perturbations such as skiers, animals etc.) [McClung, 1979b], low temperatures ($T < 0°C$) and relatively high strain rates ($\dot{\varepsilon} > 10^{-4}s^{-1}$) [Schweizer et al., 2003]. Under these conditions snow can be considered a highly porous brittle [Narita, 1984; Schweizer, 1998] cohesive granular material [Hagenmuller et al., 2014c, 2015]. Snow failure under the given conditions is still debated in the scientific community: Mohr-Coulomb criterion [McClung, 1977], Mohr-Coulomb criterion with a cap [Reiweger et al., 2015] as well as elliptical failure envelopes [Gaume et al., 2018] have been proposed to describe the plastic limit surface. In certain cases, snow failure has been observed to be coupled with a volumetric collapse [Jamieson and Schweizer, 2000; Johnson et al., 2004], somewhat resembling compaction bands in porous rocks [Mollema and Antonellini, 1996]. Recently Gaume et al. [2018] have shown that the anticrack propagation is a key feature of dry slab avalanche release and stressed the importance of accurate description of snow mechanics on the material scale.

Despite all the recent advances in snow mechanics not much is known about the micromechanical aspects of snow failure [Schweizer, 2014]. The main reason for this lack of knowledge is the low strength of snow and its sensitivity to environmental conditions which render systematic experimental exploration difficult and complicate observation at the microscopic level. As an alternative to experiments, numerical approaches have been developed with the aim to reproduce the mechanical behaviour of snow, based on the microstructural input data [Hagenmuller et al., 2014c, 2015; Gaume et al., 2017a]. These approaches offer the capacity to perform multiple loading simulations on the same sample, along with the perfect control over boundary conditions and access to microscopic descriptors. A recently developed discrete element (DEM) model of snow [Mede et al., 2018a] is thus used to obtain a deeper understanding of snow failure by studying the microscopic processes that lead to failure on the macroscale.

7.2 Discrete element simulations

Since the scope of research is restricted to failure and immediate post-failure response of snow in the brittle regime, where deformation is dominated by inter-granular damage and grain rearrangement, individual snow grains can be modelled as rigid bodies [Johnson and Hopkins, 2005; Hagenmuller et al., 2015]. The introduced simplification sufficiently diminishes the number of degrees of freedom to render computational times manageable and warrants the use of the discrete element method (DEM) [Cundall and Strack, 1979]. A specific DEM based approach has been developed in the scope of this project in order to simulate the mechanical response of snow under mixed-mode loading [Mede et al., 2018a]. The method utilizes X-ray microtomography derived images of snow as input information on snow microstructure. The grayscale attenuation images are binary segmented into pore space and a continuous ice matrix [Hagenmuller et al., 2013]. The binary image of the ice structure is then segmented into individual grains by detecting potential weak points in the ice matrix based on local geometrical criteria [Hagenmuller et al., 2014b]. In order to fully account for the snow microstructure in DEM, grain shapes are modelled by an original method, where the shape of a grain is captured by packing its volume with a set of overlapping spheres, distributed along the medial axis of the grain [Mede et al., 2018a] and clumped into an unbreakable entity. The method allows for grain shapes to be directly accounted for, while still harvesting the inherent efficiency of DEM in handling spherical contacts. Even though the method enables a perfect reconstruction of the grain shape, an approximation rather than reconstruction of grain shapes was found to produce a good balance between the numerical cost and accuracy of the simulations [Mede et al., 2018a]. The approximation is produced by selecting a subset of all grains needed for a complete grain reconstruction according to two parameters (D and R_{min}).

These approximated grains are spatially arranged according to the initial microstructure of the sample, as shown in Fig. 7.1. Grains themselves are assumed to be rigid and bonded to adjacent grains by elastic brittle cohesive bonds at the locations where grain contacts were identified by the segmentation algorithm. Since each grain consists of a multitude of spheres, the elastic brittle cohesive bonds have to be modelled between the spheres of the two contacting grains (Fig. 7.1). Contact stiffness K and adhesion A between two spheres is set proportionally to the area of the grain contacting surface that they are occupying (S_S):

$$K = S_S E \tag{7.1}$$

$$A = S_S C, \tag{7.2}$$

where E is the Young's modulus and C the tensile strength of the grain constituting material. Each initial cohesive sphere contact exhibits a linear relation between the normal displacement of spheres x_N and the tensile force F_N, where the maximal admissible tensile force is limited by the value of adhesion (Fig. 7.1). The shear force F_S is depends linearly on the shear displacement of spheres x_S, where the maximal admissible tensile force is limited by the sum of adhesion and friction $F_N\mu$ (Fig. 7.1). Once cohesion is broken in tension, it is no longer active in shear and vice-versa. Since the contact force between two grains is a sum of all sphere contact forces between the pair of grains, grain contacts exhibit qualitatively roughly equal rheology as the sphere contacts. Grain contact stiffness is a sum of all sphere contact stiffnesses and grain adhesion is a sum of all sphere contact adhesions. It should also be added that the new sphere contacts that arise due to grain rearrangement are modelled with the same value of E, but as non-cohesive elastic frictional.

In this study, we considered a cubical sample of rounded grain snow with a side length of 5 mm and density 250 kg m^{-3}, which was modelled in the DEM environment with the described method and exposed to mixed-mode loading. A rigid boundary condition is applied to the top and bottom faces, while a periodic boundary condition is applied to all four side-faces (Fig. 7.1). The samples are loaded by applying a constant shearing velocity $v = 1$ cm s^{-1} and constant normal stress p to the top surface, while keeping the bottom surface fixed. The normal stress is applied first with a ramp function of appropriate duration to avoid inertial effects. Shearing is applied once kinetic energy due to the initial compression has vanished. It has been verified that the applied shear rate is low enough to ensure a quasi-static shearing regime, i.e. that the stress-strain response is independent of v. Series of simulations were performed under different values of normal stress p, ranging from -5 kPa in tension to 10 kPa in compression. The simulations were stopped once the macroscopic shear strain reached the value $\gamma = 0.05$.

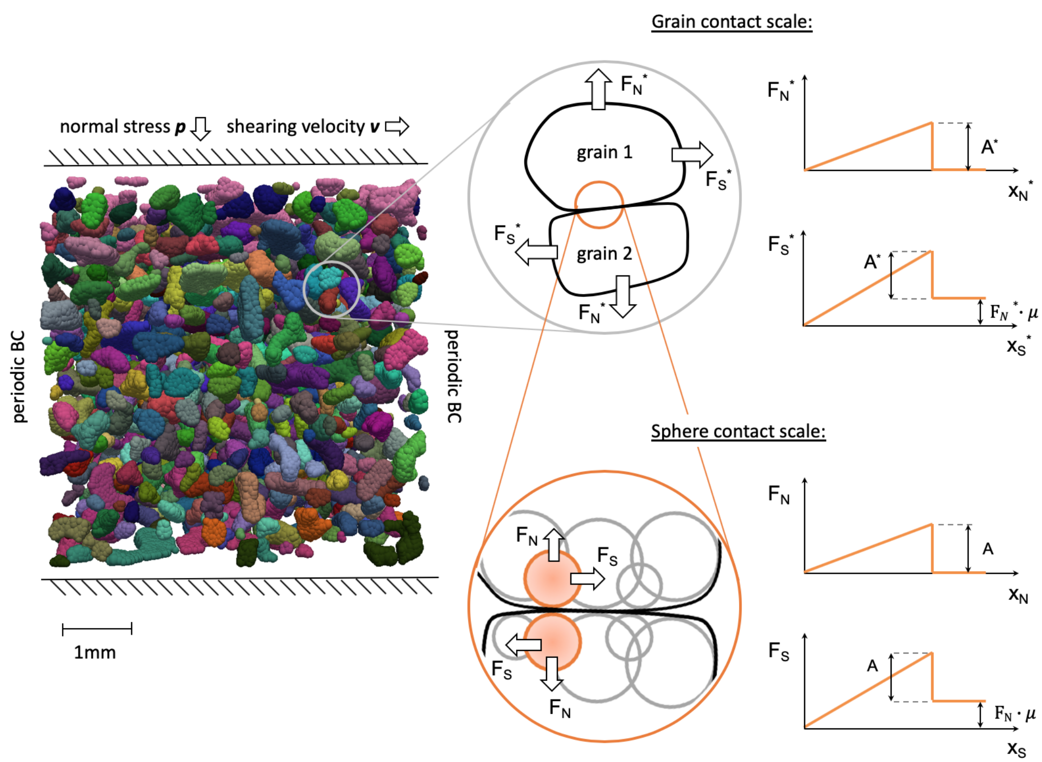

Figure 7.1: Approximated snow sample, as modelled in DEM, along with boundary conditions and applied loading. Individual grains are marked with varying colours for clarity. A schematic zoom is provided into an individual grain contact and the rheology of grain contact is displayed (F_N^* and F_S^* are normal and shear grain contact force respectively, A^* is the grain adhesion and μ is the friction coefficient). A further schematic zoom is provided into an individual sphere contact and the rheology of sphere contact is displayed (F_N and F_S are normal and shear sphere contact force respectively and A is the sphere contact adhesion).

The simulations are performed with DEM solver YADE [Šmilauer et al., 2010]. The initial cohesive sphere contacts are modelled with brittle elastic law, using a contact strength $C = 10^6$ Pa [Haynes, 1973] and Young's modulus $E = 10^8$ Pa. Intergranular sintering [Colbeck, 1998; Szabo and Schneebeli, 2007] is not accounted for in the scope of this paper. It has been verified that the utilized contact stiffness ensures the simulations are performed in the rigid grain limit [Cundall and Strack, 1979; da Cruz et al., 2005]. Contact friction coefficient $\mu = 0.2$ is fixed according to typical ice values [Hagenmuller et al., 2015]. A Cundall's non viscous damping coefficient 0.02 is applied. Gravity is not taken into account as it has a negligible effect on the response on the samples compared to external loading. Lastly, the mass of each grain is derived from the original binary image. Due to volumetric errors induced by grain approximation [Mede et al., 2018a], this results in an effective density typically increased by 15% compared to that of ice.

Analogously to [Mede et al., 2018a], a sensitivity analysis of the simulated mixed-mode loading stress-strain response to the grain approximating parameters has been performed. Nine combinations of grain approximating parameters have been considered (Fig. 7.2.b) for performing the mechanical simulations. The combination A ($D = 0.2$, $R_{min} = 2$) represents the control combination, offering a near-exact reconstruction of grains. This approximation leads to an error of the total ice volume of the reconstructed grains of the same order ($\approx 2\%$) as the one due to X-ray image processing [Hagenmuller et al., 2016].

The mixed-mode loading results (Fig. 7.2.a) produced by parameter combinations B-I are then compared against the reference response produced by parameter combination A. A mechanical error E_M [Mede et al., 2018a] is introduced and defined as the normalized root mean square error of the shear stress response of a mixed-mode loading simulation (performed for $p = 4$ kPa) for a given set of approximating parameters with respect to the reference simulation response. While a coarse approximation results in low number of spheres and relatively high mechanical error, vice-versa is true for a fine approximation. Although the mechanical error is closely related to the number of approximating spheres (and consequently the numerical cost), a fast decay of the mechanical error with the number of spheres allows accurate mechanical results to be obtained at a relatively low computational cost. Parameter combination E (D=0.5, R_{min}=5) was identified as the optimal one for this study.

7.3 Macroscopic response

The response of the considered snow sample to shearing under varying values of normal stress p is presented by a series of snapshots in Fig. 7.3, while

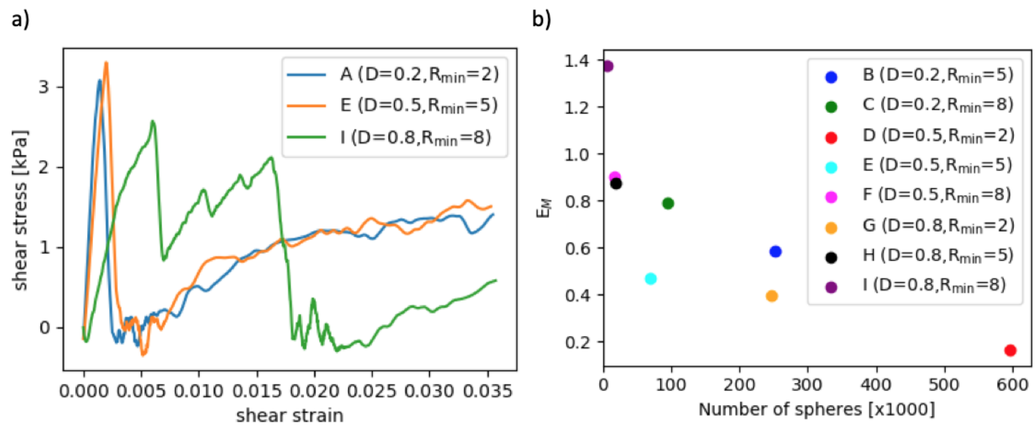

Figure 7.2: a) Simulated mixed-mode loading responses for normal pressure $p = 4$ kPa and parameter combinations A, E and I. b) Mechanical error dependency on the number of approximating spheres for mixed-mode loading simulations performed with different approximating parameters combinations. In both figures, A represents the reference response parameter combination and E the parameter combination that was identified as the optimal one.

the evolution of vertical profiles of damage within the samples for the same values of normal stress is shown in Fig. 7.4. Local damage (Fig. 7.3) is defined for each grain as the ratio of broken cohesive bonds with the neighbouring grains, whereas global damage is defined as the total ratio of broken cohesive bonds. A time scale, normalized by the time of failure (t/t_{fail}) will be used throughout this paper, where the exact definition failure is given in Eq. 7.4. The macroscopic loading and response of the sample are displayed in Fig. 7.5. Figure 7.5.a summarizes the loading conditions: normal stress is first applied to the specimen, resulting in a principal stress angle close to 0°. The fact that the principal stress angle is slightly negative results from the imposed vertical movement of the top face of the sample during the normal loading phase. The macroscopic response curves in terms of shear stress, normal strain and global damage (Figs. 7.5b-c) during this phase are marked by dotted lines. Once the normal loading is applied and kinetic energy of the sample sufficiently low, a constant shear rate is applied, the response to which is marked by solid curves. In general, three qualitatively different modes of failure can be observed, depending on the value of applied normal

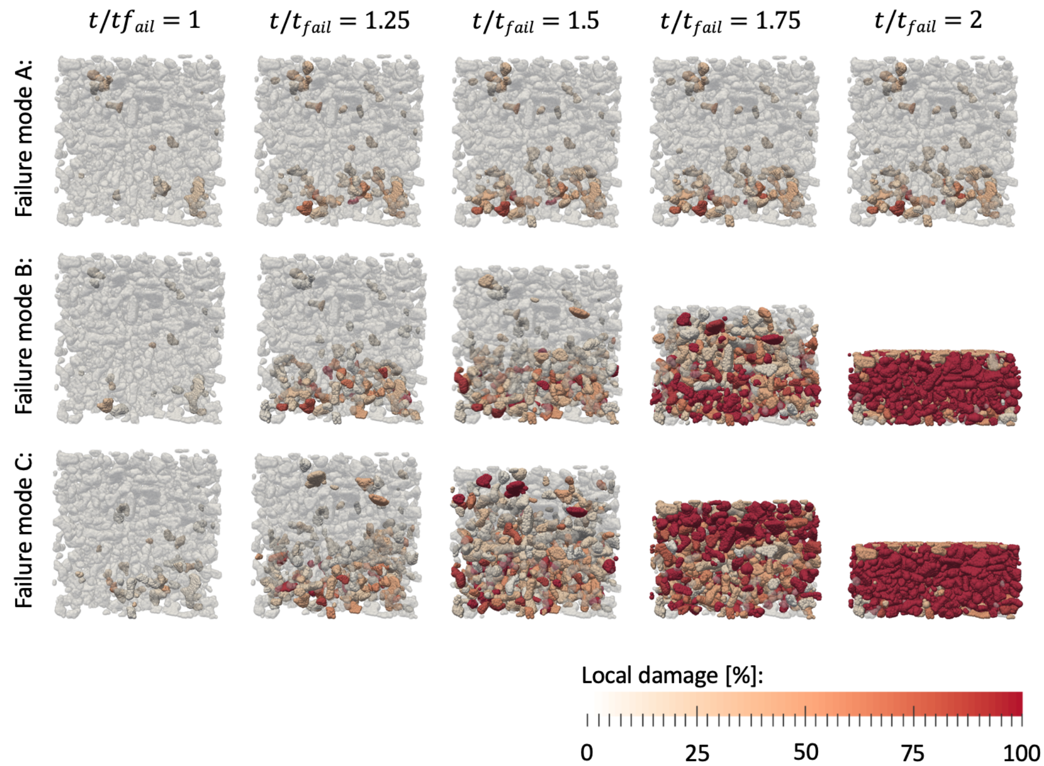

Figure 7.3: Snapshots taken during the shearing simulation for three different values of normal stress: $p = 1$ kPa, $p = 4$ kPa and $p = 9.5$ kPa. Sample responses under these three values of normal stress represent the three different failure modes that were observed in the snow sample.

stress:

Failure mode A: at low normal stresses (for the tested sample, $p < 2$ kPa), the normal loading phase does not produce any significant damage (Fig. 7.5.d) or normal strain (Fig. 7.5.c) of the sample. Subsequent application of shearing results in a quasi-elastic shear stress build-up (Fig. 7.5.b) until a peak shear force is reached, marking the shear failure. Normal strain and global damage remain low at failure onset and local damage appears dispersed (Fig. 7.3). The shear failure is followed by strain softening, which gradually diminishes shear stress to the level of residual stress. The sample fails in a narrow horizontal region (Figs. 7.3 and 7.4), where the damage

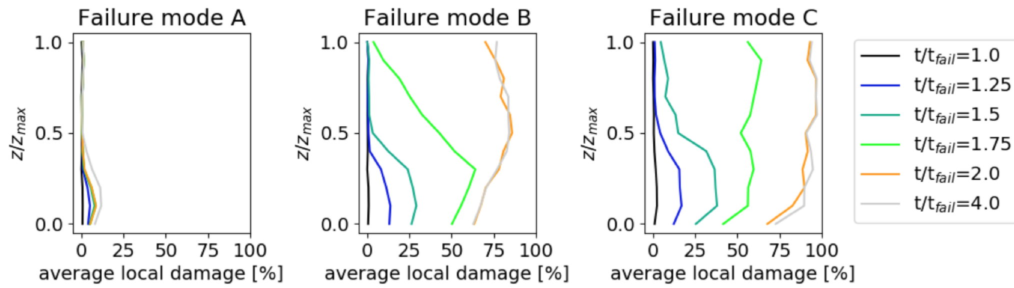

Figure 7.4: The evolution of vertical profiles of damage during the course of mixed-mode loading simulations for three different values of normal stress: $p = 1$ kPa (failure mode A), $p = 4$ kPa (failure mode B) and $p = 9.5$ kPa (failure mode C). Each figure shows a histogram of the average local damage, plotted against normalized vertical dimension of the sample (z/z_{max}).

is highly concentrated and the residual stress is due to friction between two largely intact parts of the specimen. Another partial failure event is observed at $t/t_{fail} \approx 2.5$, which results in a drop in shear stress (Fig. 7.5.a) and a slight increase of damage, which however remains limited to the narrow horizontal region where the primary failure took place (Fig. 7.4). The normal strains and global damage hence remain relatively low throughout the simulation.

Failure mode B: at moderate normal stresses (for the tested sample, $2 \leq p \leq 8.5$ kPa), the pre-failure response is qualitatively similar to that observed in failure mode A. However, as opposed to mode A, the peak shear force is followed by a volumetric collapse of the specimen (Fig. 7.5.c) and rapidly propagating damage that eventually decomposes the specimen into a cohesionless assembly of grains (Fig. 7.3). The sample collapse appears to propagate from the bottom of the sample upwards (Fig. 7.4) and has been shown to be a dynamical process, which initiates at the point of peak shear force and advances spontaneously once initiated [Mede et al., 2018b]. In contrast with the gradual strain softening and shear controlled post-failure response in mode A, mode B is marked by rapidly vanishing stresses and a time-driven response during the collapse phase. Once the sample porosity is sufficiently diminished, the normal strain and the level of damage stabilize. At this point, sample is decomposed into a cohesionless granular medium and the gradually re-emerging shear resistance is the residual stress of a cohesionless granular medium.

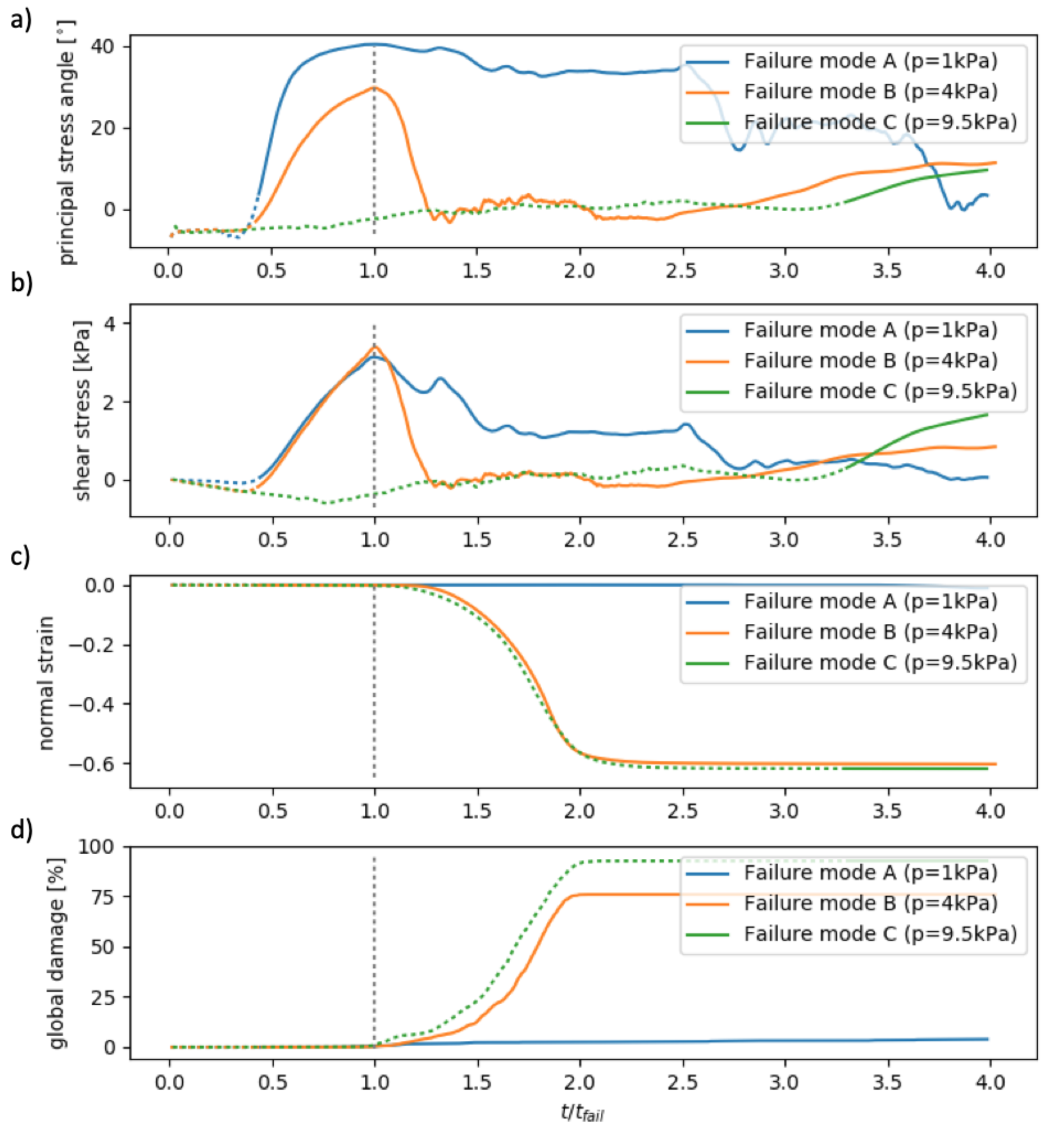

Figure 7.5: The macroscopic response of the snow sample to shearing for three different values of normal stress, which result in the three typical failure modes. The dotted parts of curves signify the normal loading stage and the grey vertical dotted line marks the failure on a normalized time scale.

Failure mode C: at sufficiently high normal stresses (for the tested sample,

$p \geq 9$ kPa), the sample is observed to fail and collapse (Fig. 7.5.c) during the application of the normal force, resulting in a rapid increase of damage (Fig. 7.5.d). Similarly as in mode B, the collapse appears to propagate from the bottom of the sample upwards (Fig. 7.4) and decomposes the sample into a cohesionless assembly of grains (Fig. 7.3). The subsequent application of shearing results in a gradual consolidation of the disintegrated sample and a shear resistance which slowly converges towards the residual stress.

The exact point of failure for each of the failure modes, marked in Fig. 7.5 is based on the second-order work criterion. It has been shown that the vanishing second-order work is a necessary condition for the existence of material instabilities [Nicot et al., 2009; Wan et al., 2013; Daouadji et al., 2011]. In the present case, a normalized definition of the second-order work is utilized:

$$W_2^N(t) = \frac{\int_{\partial\Omega} \delta\vec{f}(t) \cdot \delta\vec{u}(t)\, dS}{max_{\,t}\left(\int_{\partial\Omega} \delta\vec{f}(t) \cdot \delta\vec{u}(t)\, dS\right)}, \tag{7.3}$$

where $\delta\vec{u}$ and $\delta\vec{f}$ are incremental displacement and incremental force per surface unit along the sample boundary $\partial\Omega$. Failure time t_{fail} can thus be defined by:

$$W_2^N(t_{fail}) = 0 \tag{7.4}$$

The normalized second-order work in failure modes A and B exhibits a roughly constant value during the normal loading phase, followed by a steep increase at the onset of shearing ($t/t_{fail} \approx 0.5$). Peak value is reached at $t/t_{fail} \approx 0.6$, after which the second-order work slowly diminishes until a fast decrease takes place just before failure ($t/t_{fail} = 1$). Normalized second-order work in failure mode C also exhibits a roughly constant value during the normal loading phase ($t/t_{fail} < 0.99$), although the plot becomes somewhat more noisy at $t/t_{fail} > 0.5$). In accordance with the chosen loading protocol, shearing is not started immediately after the concluded normal loading phase, due to increasing kinetic energy. The instability thus develops in the absence of shearing. Although the prescribed external force is kept constant, oscillations of the normal force are measured on the sample boundary and a negative second-order work is recorded as a result at $t/t_{fail} = 1$. It should also be noted that the vastly different values of the normalized second-order work in the three failure modes during the normal loading phase are a result of the normalization process, where the calculated value of the second-order work is divided by the highest recorded value before failure (Eq. 7.3).

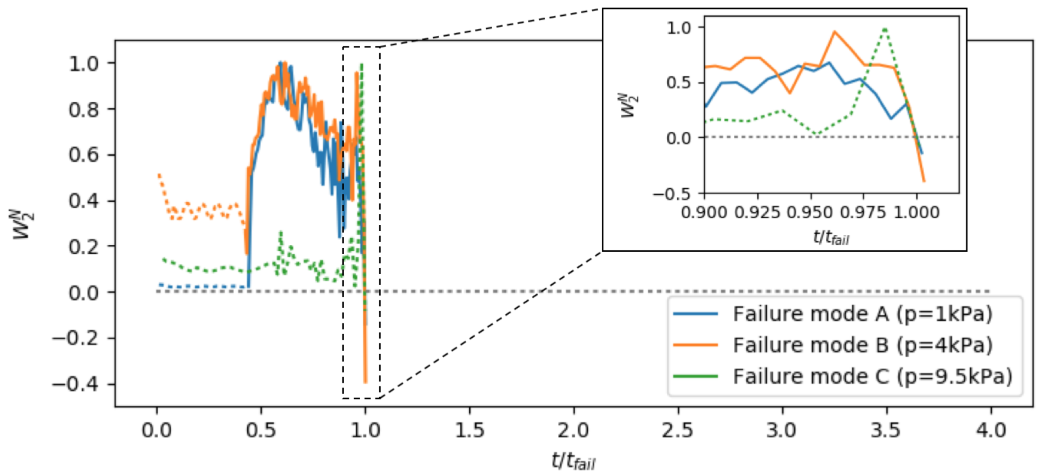

Figure 7.6: Normalized second-order work evolution for three different values of normal stress, which result in the three typical failure modes. For clarity, only the initial parts of second-order work curves are plotted - after the second order work becomes negative and the sample fails, the second-order work plot becomes extremely noisy. The dotted parts of curves signify the normal loading stage and the horizontal dotted grey line marks zero value of second-order work. A zoom is also provided into the vicinity of $t/t_{fail} \approx 1$.

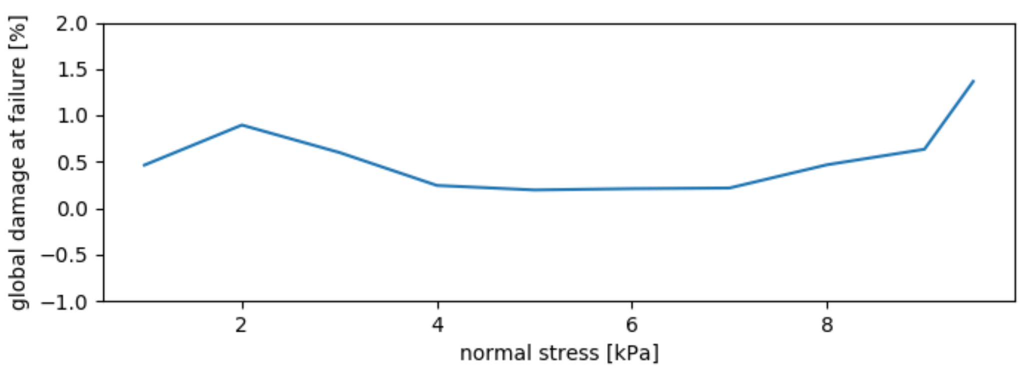

Figure 7.7: The amount of global damage present in the sample at the point of failure.

The level of global damage, necessary to trigger failure is extremely low through the entire range of simulated normal stresses (Fig. 7.7). Moreover, the global damage at failure appears almost completely independent of the applied normal stress. Evidently, failure within a small fraction of the load bearing contacts of the snow sample suffices for the entire sample to fail.

Shear stresses at failure as well as residual shear stresses after failure are plotted against applied normal stresses in Fig. 7.8. A closed failure envelope is observed that stretches far into the negative normal stress domain. While the failure shear stresses roughly follow a Mohr-Coulomb criterion in the domain of low normal stresses, they appear to follow an elliptical relation in the domain of high normal stresses. The transition between the two parts of the failure envelopes coincides with the threshold pressure which marks the transition from failure mode A into failure mode B and above which a normal collapse of the sample is observed. The residual stresses after failure follow a linear relation between shear and normal stress with an average residual friction coefficient 0.49.

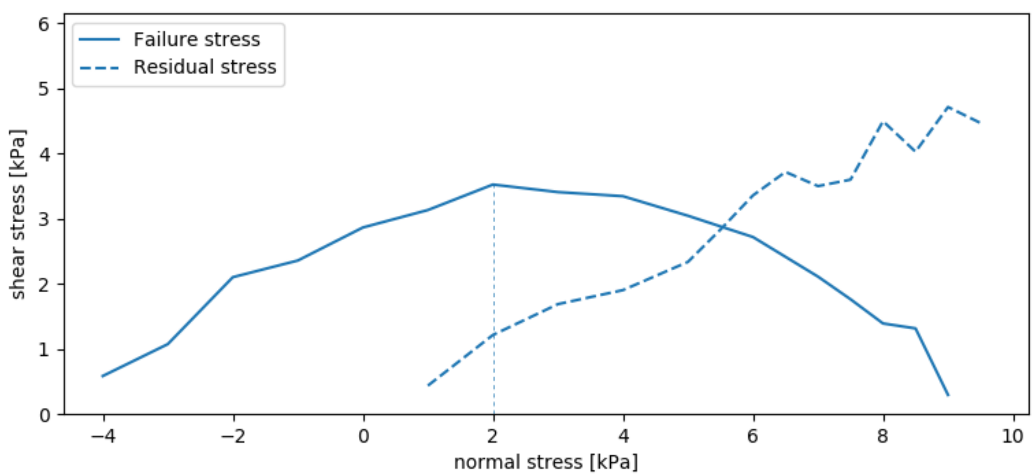

Figure 7.8: Failure envelope and residual stress after failure in the tested snow specimen. The doted vertical line marks the threshold normal stress, above which a collapse of the sample is observed.

Consistent failure modes and qualitatively similar failure envelopes were observed for snow samples of varying snow types and densities, exposed to mixed-mode loading simulations [Mede et al., 2018b]. The observed response can hence be regarded as a general snow characteristic, rather than particularity of the studied snow sample. In the following, individual failure modes are further examined on the microscopic scale.

7.4 Microscopic investigation

The reasons for the fundamentally different response of snow in the three identified failure modes are sought by observations on the microscopic level. DEM simulations provide access to all relevant microscopic descriptors, enabling the analysis of microstructural evolution and the onset of instability that leads to failure.

7.4.1 Contact force distribution

The distribution of particle contact forces during the course of the mixed-mode loading simulations is analysed for all three failure modes. Let's recall that each grain contact consists of multiple approximating sphere contacts. Figure 7.9 displays histograms of normal sphere contact forces at different time steps of before the failure.

The magnitude of normal contact forces steadily increases in all three modes as the failure draws closer. Despite the fact that only compressive and shear loading is applied to the snow samples, a fair amount of contact forces appear to be tensile. While the distribution of tensile and compressive forces seems rather symmetric in failure mode A, the ratio of compressive forces increases with the applied normal stress which produces a somewhat asymmetric distribution in mode B and a clearly asymmetric distribution in mode C.

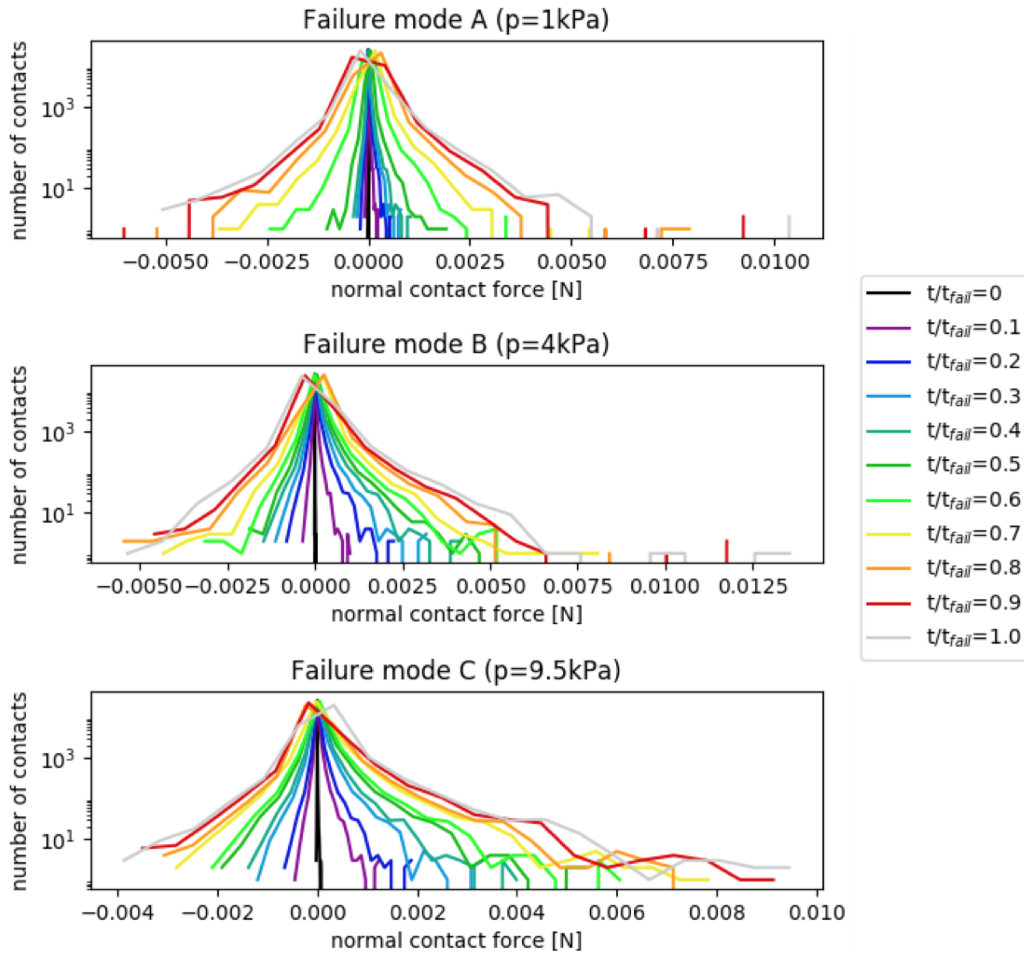

Figure 7.9: Time evolution of the distribution of normal sphere contact forces during the mixed-mode loading simulations for three values of normal stress that result in the three identified failure modes. In accordance with the utilized convention, negative normal contact forces signify tensile forces.

Contact charge C_C is introduced in order to evaluate how close these sphere contacts are to failing. Since no grain rearrangement takes place in the sample before failure, these contacts are the initial cohesive contacts. C_C is thus defined as the ratio between the sphere shear contact force F_S and the maximal admissible contact force F_{crit}:

$$C_C = sgn(F_N)\frac{F_S}{F_{crit}} = sgn(F_N)\frac{F_S}{A + F_N\mu}, \tag{7.5}$$

where the maximal admissible contact force is defined by the Mohr-Coulomb relation between the normal contact force F_N and shear contact force F_S (Fig. 7.1). A and μ are the sphere contact adhesion and friction coefficient respectively. Value $C_C = 0$ refers to a non-loaded cohesive contact and $C_C = \pm 1$, a contact load sufficient to break the cohesion. The sign of the normal contact force is used to distinct between the contact charges of tensile (negative sign) and compressive contacts (positive sign).

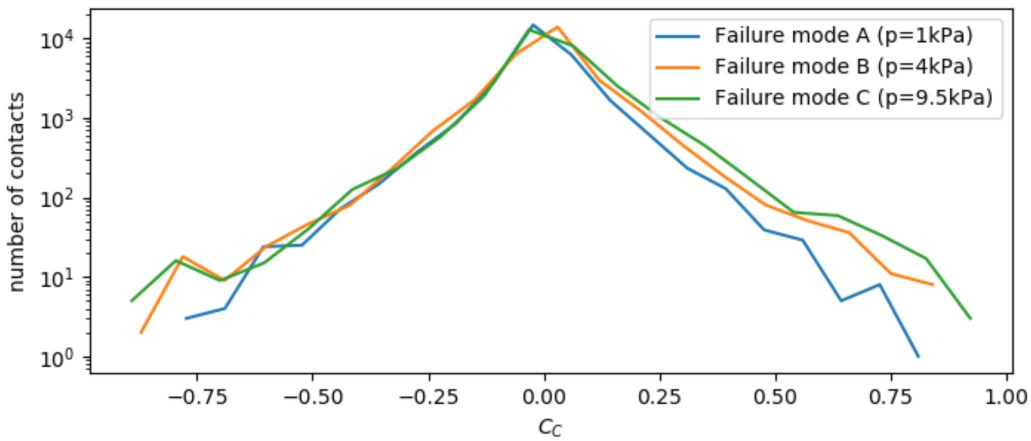

Figure 7.10: Distribution of contact charges at the point of failure under mixed-mode loading for three values of normal stress that result in the three identified failure modes.

Figure 7.10 summarizes the distribution of contact charges at the point of failure for all three identified failure modes. The distribution of positive and negative contact charges is very similar and it can be observed that the ratio of critical contact charges ($|C_C| > 0.5$) is somewhat higher in modes B and C, compared to mode A. The high ratio of critical contact charges at the point of failure could be interpreted as a partial explanation of why failure in modes B and C results in a volumetric collapse - as a small fraction of contacts fail at t_{fail} (Figs. 7.3 and 7.5.d), the increased load on the remaining contacts leads to the failure of a large number of contacts, which were already very close to failing. A more complete explanation is sought by analysing the load carrying fraction of grains within the snow sample.

7.4.2 Force chain analysis

The ultimate strength of a granular material is controlled by the stability of the force chains [Nicot et al., 2017] and a developing material instability is reflected in changes of the force chain network. Force chain buckling has been shown to anticipate material failure [Tordesillas et al., 2009], which is marked by rapid decrease in the force chain lifespans and increase emerging/dying rate of force chains [Wautier et al., 2018]. The evolution of the force chain network in the studied snow sample is thus analysed in order to characterize the microscopic mechanism of the three identified failure modes. Force chains [Peters et al., 2005], are identified by singling out the grains that comply to the following characteristics:

- Force chain grains have a compressive principal stress higher than the mean principal stress in the observed granular medium. Principal stresses in a grain are calculated by accounting for the contact forces of all the grain constituting spheres acooriding to the Love-Weber formula [Love, 2013].

- The principal stress direction of force chain particles is aligned with the force chain. A deviation of no more that 45° is allowed;

- Force chains are composed of at least three contacting particles.

Force chains are identified in the loaded snow sample and their evolution is monitored through the course of the mixed-mode loading simulations. An example of the spatial arrangement of force chains for the shearing simulation under normal stress $p = 4$ kPa is shown in Fig. 7.11. The force chains within the sample can be observed to align with the principal stress angle and assume vertical orientations during the normal loading phase (Fig. 7.11.a) and increasingly tilted orientations as the shear load is added (Figs. 7.11.b and 7.11.c). Additionally, the fact that several force chains can be observed in Fig. 7.11.b as well as Fig. 7.11.c showcases the long force chain lifespans during the pre-failure phase. This is consistent with the fact that no grain rearrangement takes place in the sample, enabling force chains to persist in an unchanged configuration.

The average force chain angles during the course of the shearing simulations for three different values of normal stress, which result in the three respective failure modes, are analysed in Fig. 7.12. Figure 7.13 displays the average lifespan of these force chains for the same three simulations. While

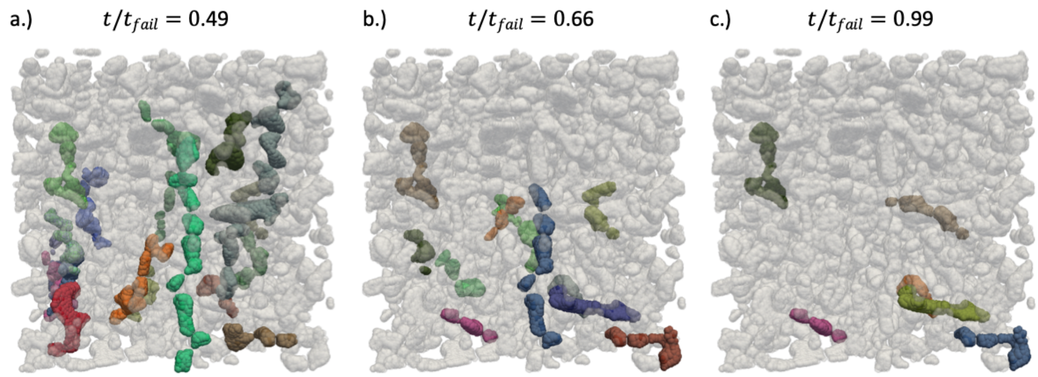

Figure 7.11: Snapshots of the shearing simulations under normal stress $p = 4$ kPa with highlighted force chains.

an alignment of the force chains with the principal stress angle was already noted in Fig. 7.11, this observation is underlined by the striking similarity between the plot of average force chain angles (Fig. 7.12) and the plot of principal stresses within the snow sample (Fig. 7.5.a). Evidently the force chains align in a way that they can transmit the the maximal load.

The normal loading phase ($t/t_{fail} < 0.5$) in failure mode A results in a monotonically increasing average force chain lifespan and a constant average force chain angle of -20° (where the angle 0° marks the vertical direction and the angle 90° marks the horizontal direction). Although 0° angle would be expected under normal loading, it should be recalled that the principal stress angle (Fig. 7.5.a) during the normal loading phase is slightly negative due to imposed vertical movement of the top sample face. Additionally, the highly porous rigid structure of snow limits the ability of force chains to adapt in terms of direction. Application of shearing ($t/t_{fail} \approx 0.5$) immediately results in a slight drop of the average force chain lifespan. The average force chain angle showcases a steep increase at the onset of shearing, which slows down considerably at $t/t_{fail} \approx 0.6$, consistently with the loading angle and the post-peak decrease of the second-order work (Fig. 7.6). Force chain lifespans oscillate around a constant value and their average angle of inclination slowly increases until failure ($t/t_{fail} = 1$). No sudden change in the force chain network is observed at failure - the average angle of inclination starts gradually diminishing while the average lifespan oscillates around a roughly constant value. The force chain life spans exhibit a significant increase in the range $1.8 < t/t_{fail} < 2.7$, which is followed by major drop in the average

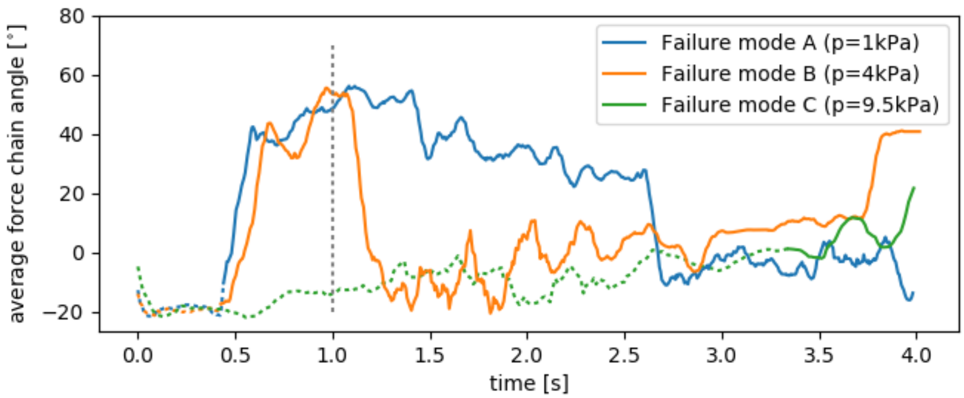

Figure 7.12: Average inclination angle of force chains during the mixed-mode loading simulations for the three identified failure modes, where the angles 0° and 90° mark the vertical and the horizontal direction respectively. The dotted parts of curves signify the normal loading stage for each mode separately and the vertical dashed line marks the onset of failure.

force chain lifespan and inclination angle. This represents a significant force chain breaking event that results in a noticeable increase of average damage within the localized failure band (Fig. 7.4). The latter is consistent with the diminished resistance of the sample to shear loading, which is reflected in the drop of the macroscopic shear stress (Fig. 7.5.b) and the decreasing loading angle (Fig. 7.5.a).

Force chain development in mode B for $t/t_{fail} < 1$ appears very similar to that observed in mode A. The post-failure evolution of the force chain network is however significantly different. Consistently with the onset of the volumetric collapse, a major force chain breaking event is observed, resulting in the average force chain lifespan dropping to a value close to zero. During the collapse, force chains align in the vertical direction due to inertial forces linked to the collapse. Once the volumetric collapse is concluded $t/t_{fail} \approx 2$, the average force chain lifespan and inclination angle start increasing. This is consistent with the slowly re-emerging shear resistance (Fig. 7.5.b) and the evolution of the loading angle (Fig. 7.5.a).

Average force chain lifespan in mode C exhibits a monotonic increase until a minor decrease is observed at $t/t_{fail} \approx 0.5$. This point roughly coincides with the onset of oscillations of the second-order work (Fig. 7.6). The average force chain lifespan reaches a second peak at $t/t_{fail} \approx 0.95$, when a local

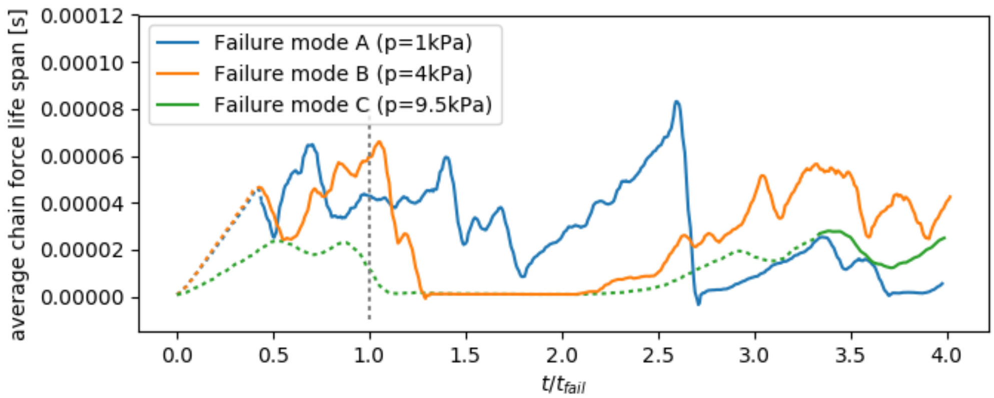

Figure 7.13: Average force chain life span evolution during the mixed-mode loading simulations for all three identified failure modes. The dotted parts of curves signify the normal loading stage for each mode separately and the vertical dashed line marks the onset of failure.

minimum of the normalized second-order work is recorded. Second-order work at this point is still positive, but starts oscillating severely, along with a rapid decrease in of the average force chain lifespan, leading to the onset of collapse at $t/t_{fail} = 1$ and consequent grain rearrangement. The average force chain angle starts at -20° and then gradually increases to 0° during the normal loading phase. No abrupt change of the average force chain angle is observed at failure, consistently with a roughly constant principal stress angle in this phase of the simulation (Fig. 7.5.a). Shearing is applied at $t/t_{fail} \approx 3.4$ and results in a gradual increase of the average force chain angle and lifespan.

Force chain network is thus shown to reflect the loading capacity and the mode of failure of the snow sample. The force chains are shown to align with the principal stress angle in order to transmit the maximal load through the sample. The force chain lifespans on the other hand clearly display the difference of failure in modes A on one hand and modes B and C on the other. While no abrupt change in the force chain lifespans is observed at failure in mode A, a rapid decrease is observed in modes B and C. Consequently, the material maintains a relatively high load bearing capacity in mode A, resulting in a localized failure, whereas the failure of the load bearing fraction of the sample in modes B and C triggers and complete volumetric collapse.

7.4.3 Force distribution within force chains

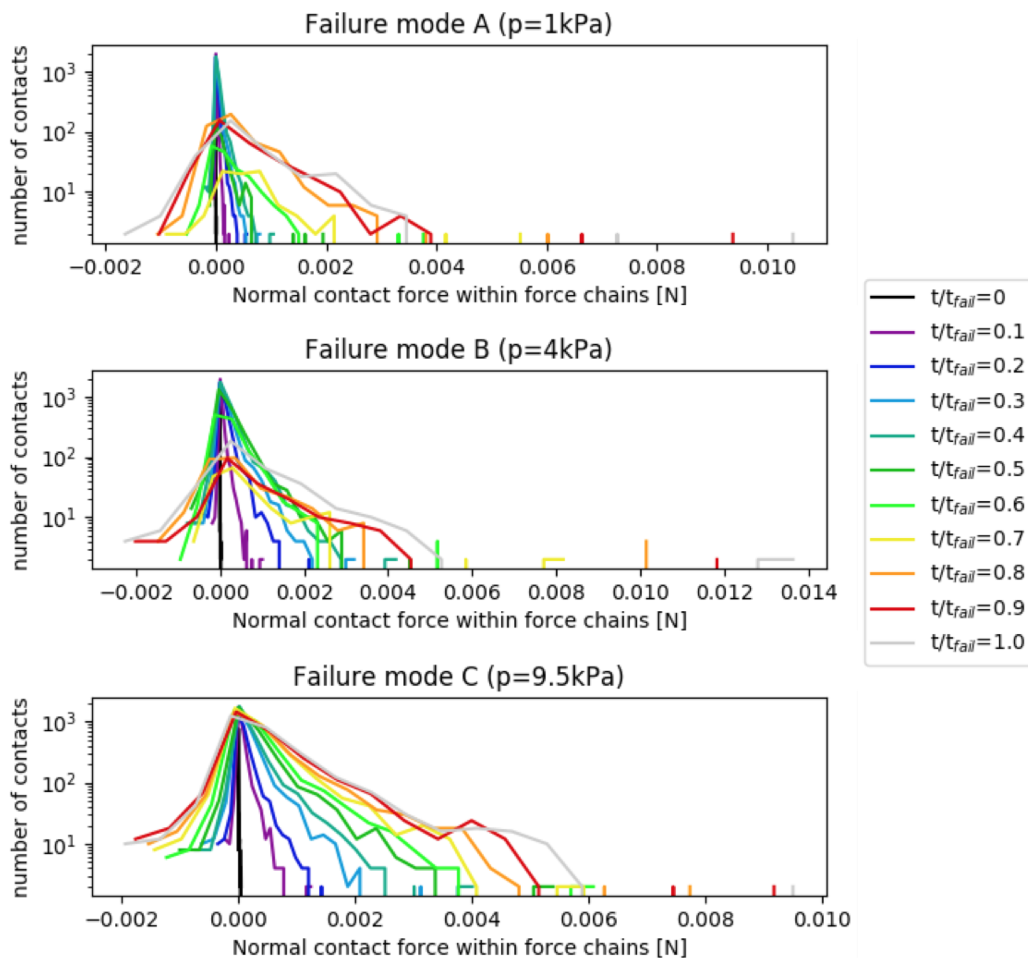

Figure 7.14: Distribution of normal contact forces within the force chains at different time steps before failure for three values of normal stress that result in the three identified failure modes. In accordance with the utilized convention, negative normal contact forces signify tensile forces.

Having defined the force chain network, the contact forces within the force chains can now be analysed. Due to defining characteristics of force chains, contact forces between individual grains of force chains are strictly compressive on the grain scale. This is however not necessarily true for the sphere contacts, as can be observed in Fig. 7.14. While the majority of sphere contact forces in all three modes are compressive, a smaller fraction of contact forces appears to be tensile. Similarly as contact forces in the whole specimen (Fig. 7.9), the magnitudes of tensile as well as compressive sphere contact forces gradually increase in all three failure modes as the failure draws closer. However the number of tensile sphere contacts within the force chains is distinctly higher in modes B and C compared to mode A, especially in the short interval before the onset of failure ($t/t_{fail} > 0.7$). Since the sum of all sphere contact forces for each pair of contacting grains within force chains is compressive, the existence of tensile sphere contacts can be interpreted as force chain bending. More specifically, since the force chains were shown to align with the principal stress angle, this bending could be related to buckling. Volumetric collapse in modes B and C is thus shown to be anticipated by pronounced force chain buckling. A failure can be expected when the force chains become unstable. The force chain stability has previously been shown to be greatly influenced by the grains surrounding the force chains [Nicot et al., 2017]. The contacts between the force chains and the surrounding grains are therefore analysed in order to observe the influences on force chain stability.

7.4.4 Force distribution around force chains

It is generally accepted that compressive confining forces insure the stability of force chains [Nicot et al., 2017] in dense cohesionless granular assemblies. The degree of lateral support has been shown determine the extent to which force chains can resist buckling [Tordesillas and Muthuswamy, 2009]. This reasoning can not be directly applied to snow, due to the fact that it is an extremely loose cohesive granular material. It has already been shown in Fig. 7.9, that even under uniaxial compression, a large amount of particle contact forces are tensile. The latter is possible due to the cohesive nature of these contacts. The applied forces that the surrounding grains supply to the force chain members are observed to be tensile as well as compressive and it is difficult to differentiate which of these have the stabilizing and which the non-stabilizing effect. Instead, it has been analysed how close these contacts are to failing by calculating the contact charge (Eq. 7.5).

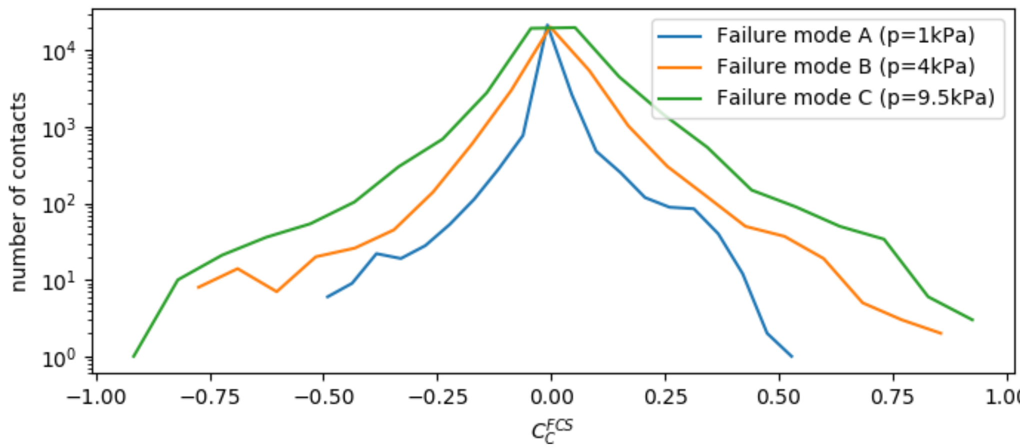

Figure 7.15: Contact charges between the force chain grains and the surrounding grains at the point of failure for the mixed-mode loading simulations under three values of normal stress that result in the three identified failure modes.

Figure 7.15 displays the contact charges of the sphere contacts between the force chain grains and the surrounding grains at the point of failure. It can be observed that the amount of critical contact charges ($|C_C| > 0.5$) at the point of failure is substantially higher in modes B and C, compared to mode A. This difference is particularly striking for the negative contact charges, where a relatively large number of contacts in modes B and C have a critical charge.

The contacts between the force chain members and the surrounding grains provide lateral forces that insure the stability of force chains. A failure in any of these contacts will increase the loading on the remaining contacts and in the case of a high number of critical charges, this can trigger a chain reaction, which will cause a large number of these supporting contacts to fail. While a failure of a compressive contact charge will diminish the exerted force on the force chain, a the failure in a tensile contact will withdraw the support to the force chain completely. This underlines the importance of a high number of critical contact charges at the point of failure in modes B and C. The withdrawn support to the force chains enables the force chain buckling to develop, causing the failure of the load bearing fraction of the snow sample, which results in a complete volumetric collapse of the sample. The failure within force chains is clearly exhibited by the rapidly diminishing force chain lifespans at failure in modes B and C (Fig. 7.13). Low contact charges at failure in mode A on the other hand insure the stability of the force chains, resulting in a relatively high load bearing capacity of the material and consequently a localized failure. This claim is consistent with the high force chain lifespans that do not substantially diminish at failure in mode A (Fig. 7.13).

7.5 Conclusions

Thanks to combined use of microstructure-based DEM modelling and state of art micromechanical analysis, macroscopic snow failure under mixed-mode loading was related to microscopical physical mechanisms, leading to material instabilities.

Snow failure was first characterized on the macroscale and three distinct failure modes were identified. Failure mode A takes place under low values of normal tress and manifests as localized failure of a narrow horizontal band of snow. Failure mode B is observed under moderate values of normal stress, where a shear-induced failure triggers a dynamic volumetric collapse. Failure mode C is observed under high values of normal stress and results is a normal failure and volumetric collapse. The necessary level of global damage, needed for the snow sample to fail was observed to be extremely low for all three failure modes and appears to be independent of the applied normal stress. Failure envelope of snow was shown to feature a closed shape, which appears to follow a Mohr-Coulomb relation at low- and an elliptic cap at high values of normals stress. The transition from linear to the elliptic part of the failure envelope was observed to coincide with the transition from failure mode A to failure mode B, i.e. the threshold normal stress, above which a volumetric collapse of snow is observed.

The volumetric collapse of weak snow layers has been shown to have a key influence on the release of dry snow slab avalanches [Gaume et al., 2015, 2018]. Although this phenomena is well recorded [Van Herwijnen et al., 2010; Johnson et al., 2004], the conditions under which is appears remain unclear. The DEM model developed in the scope of this project, which successfully reproduces the collapse of snow samples, was already utilized to show how volumetric collapse at failure depends on the level of applied normal stress [Mede et al., 2018b]. In this paper we go further and explore the microscopic mechanisms that lead to volumetric collapse. Analysis of particle contact forces showed that compressive as well as tensile forces are present in the sample during the entire loading phase before the onset of failure. This is consistent with the work done by Gaume et al. [2017a] as well as Hagenmuller et al. [2014b,c], who already recorded a large fraction of tensile particle contact forces under simulated compression of snow. While the distribution of tensile and compressive forces in mode A is rather symmetric, the ratio of compressive contact forces forces increases in modes B and C, consistently with the higher value of applied normal stress. At the point of failure a higher ratio of high contact charges in modes B and C suggests that the number of contacts close to failing is increased compared to mode A, which can be considered a partial explanation of why a sudden collapse is observed at failure in these two modes.

A more complete micromechanical explanation was sought by analysing the load carrying fraction of grains within the snow sample. While the force chains were shown to align with the principal stress angle in the snow sample, their average lifespans were observed to reflect the stability of the snow sample. In all three failure modes the force chain lifespans steadily increase during the initial phase of loading and then begin to stagnate shortly before failure is observed. The analysis of sphere contact forces within force chains showed that while the majority of sphere contact forces are compressive, a non-negligible amount of contact forces are tensile. Moreover, the ratio of high tensile forces in modes B and C is decidedly higher than in mode A, particularly when the failure is near. Since the contact forces between the force chain members on the scale of the grain are strictly compressive, consistently with the utilized definition of the force chain, tensile sphere contact forces can be interpreted as force chain bending. As the force chains are aligned with the principal stress direction, it can be assumed that this bending is induced by buckling. We thus show that the phenomena of force chain buckling, which has already been identified as the micromechanical process leading to material failure in the case of dense granular media [Tordesillas et al., 2009] also represents an important mechanism of failure in the case of loose cohesive materials such as snow. Furthermore, the analysis of contacts between the force chain members and the surrounding grains showed that at the point of failure in modes B and C, a relatively high number of contacts are close to failing, which is not the case in mode A. Additionaly, the amount of tensile critical contacts in modes B and C is particularly high. Contacts between the force chain members and the surrounding grains insure the stability of force chains in snow in a similar way that lateral compressive contact forces were shown to insure the stability of force chains in dense granular media [Tordesillas and Muthuswamy, 2009; Nicot et al., 2017]. However, once these contacts start failing, the support to the force chains is diminished in the case of compressive contacts and completely withdrawn in the case of tensile contacts, which allows force chain buckling to develop, eventually leading to force chain collapse. The average lifespans in modes B and C are indeed observed to rapidly decrease at the point of failure, while a very slow gradual decrease of lifespans is observed after failure in mode A. The failure of the load carrying fraction of the sample in modes B and C consequently leads to the volumetric collapse of the sample, while stable force chains result in a localized failure in mode A.

The conducted research thus provides an original insight into the microscopic mechanisms of material instabilities that lead to the volumetric collapse of snow under mixed-mode loading. High contact charges in the vicinity of force chains are identified to trigger volumetric collapse of snow, by withdrawing support to the force chains and allowing force chain buckling to develop, leading to eventual collapse of the load carrying fraction of the snow microstructure.

Appendix

7.A Analysis of the spatial distribution of damage in the snow sample

This appendix provides a detailed insight into the spatial distribution of damage in the snow samples during the mixed-mode shear and normal loading simulations.

7.A.1 Spatial distribution of damage at failure

In order to compare the spatial distributions of damage at the point of failure under different values of applied normal stress, damage distribution similarity DDS is introduced:

$$DDS = 1 - \underbrace{\frac{1}{D_{max} - D_{min}} \sqrt{\frac{\sum_i (D_i^a - D_i^b)^2}{N}}}_{\text{normalized root-mean square deviation}}, \tag{7.6}$$

where D_i^a and D_i^b refer to local damages of an individual grain in the two compared simulations , D_{max} and D_{max} to the maximum and minimum value of local damage and N to the number of grains. The second part of the equation represents a normalized root mean square deviation of the damage distribution between two individual simulations at the point of failure. It is important to stress that the index i runs only through the grains with local damage greater than zero. Since the global level of damage at failure is very low, this is necessary in order to exclude the contributions of undamaged grains. In the opposite case, the DDS between two simulations at the point of failure could be very high simply due to the low level of global damage, which would result in a low root mean square deviation.

Damage distribution similarity between the shearing simulations under different levels of applied normal stress at the point of failure is shown in Fig. 7.16. The value of DDS between a majority of simulations is over 0.6, indicating a strong resemblance, which indicated that failure is initiated by the same microstructural weakness in different loading scenarios. Furthermore an increased DDS between the simulations under the normal stresses 1 kPa $\leq p \leq$ 3 kPa, those in the range 4 kPa $\leq p \leq$ 7 kPa and those in the range 9 kPa $\leq p \leq$ 9.5 kPa can be observed. Although these ranges don't completely coincide with the previously identified normal stress ranges of failure modes A and B, a strong resemblance between the damage distributions of different simulations with the same failure mode is still obvious.

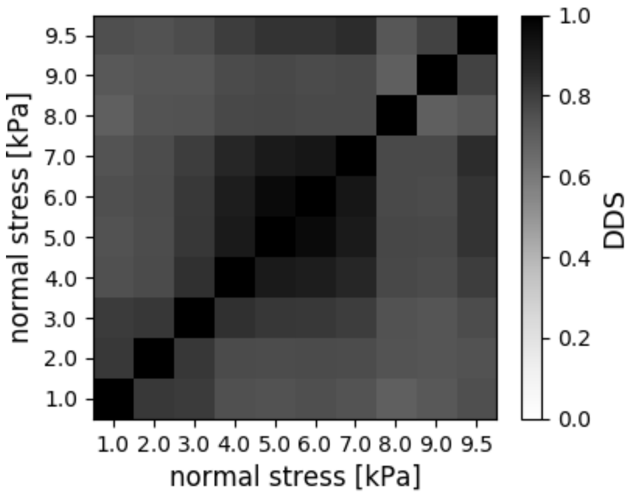

Figure 7.16: Damage distribution similarity between the shear simulations under varying levels of normal stress at the point of failure.

7.A.2 Damage clustering

The localication of spatial distribution of damage was analysed in order to determine how sample failure is related to damage clustering. Moran's index I [Moran, 1950] is a statistical measure of spatial autocorrelation of a given data set and by applying it to the evolution of spatial distribution of local damage during the mixed-mode loading simulations, the amount damage clustering can be quantified. Moran's index of local damage distribution $I(D)$ can be calculated as:

$$I(D) = \frac{N}{\sum_i \sum_j \omega_{ij}} \frac{\sum_i \sum_j \omega_{ij}(D_i - \overline{D})(D_j - \overline{D})}{\sum_i (D_i - \overline{D})^2}, \tag{7.7}$$

where N is the total number of grains, i and j are the grain increments, D is the local damage of individual grains and $\overline{D}$ is the global damage of the sample. The weight matrix ω_{ij} is defined by a method introduced by Liu et al. [2018] for a granular assembly:

$$\omega_{ij} = \begin{cases} 1, & \text{if grains } i \text{ and } j \text{ are in contact} \\ 0, & \text{otherwise.} \end{cases} \tag{7.8}$$

The values of Moran's index range between -1 and 1, where $I = 1$ indicates perfect clustering of similar data values and a spatial heterogeneity. $I = 0$ marks a completely random distribution of values and $I = -1$ would theoretically mean a perfect clustering of dissimilar values, but is rarely observed in nature.

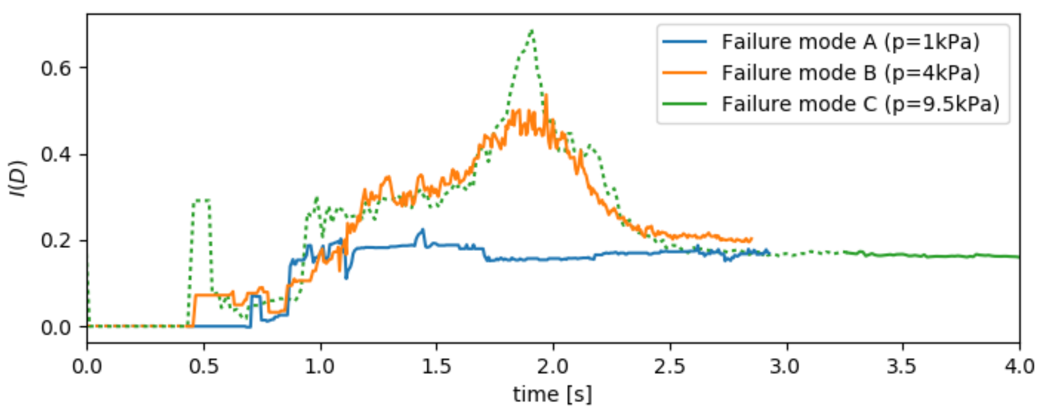

Figure 7.17: The evolution of Moran's index during the mixed-mode loading simulation for all three identified failure modes. The dotted parts of curves signify the normal loading stage and the vertical dashed lines mark the onset of failure for each mode separately.

Figure 7.17 displays the evolution of Moran's index for the shearing simulations under three values of normal strain that result in the three distinctive failure modes. An increase in $I(D)$ observed in mode B and a peak of $I(D)$ is observed in mode C at $t/t_{fail} \approx 0.5$. This event coincides with the first force chain breaking events (Fig. 7.13). The value of Moran's index is then observed to increase to $I(D) \approx 0.2$ in modes A and B and $I(D) \approx 0.3$, by the time of failure onset $t/t_{fail} = 1$. The further development of damage clustering is completely different in mode A, compared to modes B and C. The value of Moran's index remains roughly constant in mode A, consistently with the development of damage, which remains limited to the narrow band along the which the sample fails (Figs. 7.3 and 7.4). The value of $I(D)$ in modes B and C on the other hand exhibits a major increase during the volumetric collapse and reaches a peak at $t/t_{fail} \approx 1.8$. This consistent with Fig. 7.4, where it can be observed that the damage during collapse propagates from the bottom upwards, resulting in high values of $I(D)$. After the volumetric collapse the value of $I(D)$ in modes B and C slowly diminishes and reaches a similar value than in mode A ($I(D) \approx 0.2$) at $t/t_{fail} \approx 3$.

Chapter 8

Conclusion and perspectives

Contents

8.1 Conclusion

The aim of this PhD was the exploration of large strain mechanical response of snow to mixed-mode shear and normal loading, due to its relevance to the modelling of slab avalanche release. In the course of the PhD numerical tools for snow mechanics have been developed and an exciting new insight into mixed-mode loading response of snow has been obtained.

8.1.1 Numerical tools for snow mechanics

Grain approximation A novel method for representing arbitrary grain shapes in DEM framework has been developed. 3D binary images of grains are taken as input information and the medial axis concept is utilized in order to produce an optimal distribution of overlapping spheres that reconstruct the shapes of the grains. With respect to the values of two parameters, a subset of these reconstructing spheres is identified, which constitutes a grain approximation. Depending on the values of the two grain approximating parameters, different levels of grain approximation are possible and a balance is sought between the accuracy of grain representation and the number of utilized spheres. It is shown that the accuracy of mechanical simulations under different loading scenarios is highly correlated to the average relative volumetric error of grain approximation, i.e. the average missing volume of the grains due to to grain approximation. A methodology is introduced that enables the choice of grain approximating parameters, which will result in a certain level of precision of the mechanical simulation.

Discrete element model of snow A microstructure-based numerical model of snow has been developed, which enables large strain simulations. The assumption that snow behaves as a cohesive granular material and that immediate post-failure response is governed by grain rearrangement allowed us to model individual grains as unbreakable entities and employ a DEM solver to perform simulations. Individual grains are hence identified by applying a segmentation algorithm to an X-ray microtomography image of a snow sample, which is taken as input information. The developed algorithm for grain approximation is used to approximate the shape of grains with an accuracy that corresponds the desired accuracy of the mechanical loading simulation. Each grain is placed on its respective position in the ice matrix and elastic-brittle cohesion is built between adjacent grains. The developed model thus enabled us to study the effect of microstructure on failure and post-failure response of snow.

General remarks Certain assumptions have been made in order to reduce the computing time during the course of this research. While the assumptions are reasonable it is nevertheless important to note that the computed results rely on the validity of these assumptions:

- While performing the sensitivity analysis of the mechanical loading simulation of snow with respect to the grain approximating parameters, it was not computationally feasible to perform simulations with completely reconstructed grains. Instead, the simulation response at the highest accuracy of grain approximation was taken as the reference response. The volumetric error of this particular grain approximation is on the same order as the volumetric variation of the input tomographical X-ray image due to the choice of image processing parameters.

- The grain approximating parameters for samples s-RG2 and s-FCDH were chosen by assuming that the functional dependency between volumetric error of grain approximation and mechanical simulation error, demonstrated for sample s-RG1, applies to other snow samples as well.

- Assuming that failure and immediate post-failure response of snow is governed by grain rearrangement allowed us to consider grains as rigid bodies. This significantly reduced the number of degrees of freedom of snow specimens and made it possible to run the simulations in reasonable computational times. As an indication, calculation times on a single core Intel(R) Xeon(R) 2.20GHz processor varied between one day and several weeks, depending on the sample size.

8.1.2 Insights into mixed-mode loading response of snow

The developed discrete element model of snow was utilized in combination with the grain approximating method to simulate the mixed-mode shear and normal loading response of three different snow samples, including two samples of rounded grain snow and one sample of faceted crystals, mixed with depth hoar. The choice of samples allowed us to separately observe the influence of density and snow type on the response of snow. Conducted numerical simulations have provided new insights into the mechanical behaviour of snow relevant to modelling snow avalanche release.

Consistent responses Consistent responses to mixed-mode loading were observed for all three samples. Despite the fact that one of the tested samples is a weak layer sample, no qualitative difference with respect to other two snow samples was observed in terms of failure envelope, post-failure response or activated failure modes. These results contradict a widely accepted assumption that weak layers response under mechanical loading is qualitatively different from that of 'strong' snow. Let us recall that normal failure and collapse have hitherto been associated with weak layers [Van Herwijnen et al., 2010; Gaume et al., 2015], while the failure in 'strong' has been associated with a Mohr-Coulomb relation [McClung, 1977; de Montmollin, 1982; Chandel et al., 2014b]. Consequently, modern approaches to large-scale modelling of snow avalanche release [Gaume et al., 2018] presume different constitutive relations for the weak layer and the slab. The work done in the scope of this thesis challenges this assumption and suggests that the differences in the constitutive mechanical behaviour of 'weak' and 'strong' snow might be quantitative rather than qualitative.

Failure modes Three distinct failure modes of snow have been defined under mixed-mode loading, depending on the level of applied normal stress. Under low values of normal stress, snow samples were shown to fail in shear, along a narrow horizontal band, where all the damage is concentrated. Under moderate normal stresses, shear failure triggers an abrupt volumetric collapse of snow samples. The collapse is a dynamic event which, once started, spontaneously advances independently of shearing. In the case of high normal stresses, snow samples fail and collapse under pure normal loading. While the volumetric collapse is generally associated with weak layers [Gaume et al., 2018], it has recently been shown to have an important effect on bending and fracture of the slab [Gaume et al., 2017b] and the anticrack propagation has been identified to have a major influence on the size of the slab avalanche [Gaume et al., 2018]. While the normal collapse of the weak layer at failure has been experimentaly proven [Johnson et al., 2004], the conditions under which it appears have remained unexplored. During the course of this thesis, collapse has been shown to depend on the loading path rather than the type of snow - it appears to be a general property of snow failure if the applied normal stress is sufficiently high. Additionally, the collapse should be viewed a response to a boundary value problem, rather than an intrinsic constitutive feature of the material. This may have have important consequences on the modelling of collapse wave propagation in slab avalanche release [Gaume et al., 2018].

Failure envelopes Simulated failure envelopes were shown to feature closed shapes, resembling the modified CamClay plasticity envelope, where failure stresses follow a Mohr-Coulomb dependency at low values of normal stress and gradually reduce to zero in an elliptical arc at higher values of normal stress. Moreover, the transition from Mohr-Coulomb dependency to the elliptical cap was shown to roughly coincide with the threshold normal stress, above which the volumetric collapse of snow samples is observed. These results are in good agreement with the failure envelopes for weak snow layers, experimentally obtained by Chandel et al. [2014a] and Reiweger et al. [2015]. A thorough knowledge of the snow failure envelope bears great importance as it is one of the key ingredients for building a constitutive model of snow as demonstrated by a recently developed CamClay-inspired constitutive model of snow [Gaume et al., 2018].

Damage at failure Extremely low level of damage was observed to trigger failure in snow samples. Furthermore, this damage level was shown to be essentially independent of the applied normal stress. The analysis of spatial distribution of damage at failure revealed a high correlation between different loading scenarios, suggesting that failure is initiated in localized preferential zones of weakness in the microstructure. These observations are consistent with the minimum cut density concept [Hagenmuller et al., 2014a], which underlines the fact that the pre-failure response of snow is governed by the weak spots in the connectivity of the ice matrix.

Force chain buckling The evolution of force chain network has been monitored during the mixed-mode loading simulations. Force chains were observed to align with the main principal stress direction and the average force chain lifespan was observed to reflect the mechanism of failure in each particular mode: while no abrupt change in force chain lifespans is observed at failure in mode A, the latter immediately drops to zero at failure in modes B and C due to grain rearrangement during collapse. Distribution of sphere contact forces within the force chains revealed a significant portion of tensile forces, particularly in modes B and C. Since the sum of contact forces on the scale of the grain within force chains is by definition compressive, individual tensile contact forces can be interpreted as a sign of bending. Moreover, since the force chains were shown to align with the principal stress direction within the material, this bending should be induced by buckling. A more pronounced buckling in modes B and C is identified as the microscopic mechanism that leads to the volumetric collapse. While force chain buckling is now widely accepted as the micromechanical process that leads to failure in dense granular materials [Tordesillas et al., 2009; Nicot et al., 2017], little is known on the force chain network evolution in highly porous cohesive materials and particularly snow. This work thus offers a micromechanical explanation of snow failure by relating the stability of the load-bearing meso-structures within snow to its volumetric collapse.

Origins of force chain stability It is generally accepted that compressive confining forces insure the stability of force chains [Nicot et al., 2017] in dense cohesionless granular assemblies. The degree of lateral support has been shown determine the extent to which force chains can resist buckling [Tordesillas and Muthuswamy, 2009]. This reasoning can not be directly applied to snow, due to the fact that compressive as well as tensile forces are applied to the force chain members by the surrounding grains. Instead, the notion of a critical contact was introduced in order to identify the cohesive grain contacts that are very close to failing. It was shown that at the point of failure in modes B and C, a substantially higher portion of the contacts between the force chain members and the surrounding grains qualify as critical contacts, compared to mode A. Once these contacts start failing, an unbalanced force is exerted on the force chain, resulting in force chain bending and eventual collapse. A quickly diminishing average lifespan of force chains is indeed observed at failure modes B and C. The failure of the load bearing fraction of the granular assembly leads to the dramatic volumetric collapse observed in these two modes. Reduced fraction of critical contacts between the force chain members and the surrounding grains at failure in mode A on the other hand insures the force chain stability, which results in unchanged average force chain lifespan at failure and consequently a localized failure within the snow sample.

General remarks Certain remarks should be taken into account concerning the methodology used to produce the given insights into the mixed-mode loading response of snow:

- It should to be noted that only three snow samples were subjected to the mixed-mode loading simulations. The observations on the generality of the identified failure modes as well as qualitative similarities between the mechanical responses of weak layers and 'strong' snow samples rest on a very limited set of data and should thus be interpreted with caution.

- The snow sample response close to failure was observed to be highly sensitive to the loading regime. It needs to be stressed that even small variations in the loading or deformational rate can alter snow response in the vicinity of the failure point.

- The question whether the utilized size of samples is sufficient to consider the mechanical response representative needs to be addressed. The fact that failure is triggered by an extremely low level of damage suggests that the ultimate strength of the sample depends on the few weakest grain bonds. Considering the spatial variability of snow microstructure, the concept of a representative elementary volume is somewhat questionable. It should however be noted that the sample size considered in this study has been shown to result in a representative mechanical response in the case of simulated large strain compression [Hagenmuller et al., 2015] on samples s-RG1 and s-FCDH. Additionally, the size of these two samples was proven sufficient to estimate the minimum cut density [Hagenmuller et al., 2014a], which is related to the minimal damage needed to break the sample. We can thus argue that this sample size is also sufficient to monitor representative damage evolution under mixed-mode loading.

8.2 Perspectives

Based on the work conducted in the scope of this project, perspectives for further research are discussed, as seen by the author of this PhD.

Model improvements While the presented numerical model has been developed to simulate the brittle response of snow, its domain of application could be expanded by altering the grain contact law. By incorporating a cohesive-viscous-elastic contact law and grain sintering, the model could be upgraded to account for ductile behaviour as well. The option of a cohesive-viscous-elastic contact law is unfortunately currently not available in YADE [Šmilauer et al., 2010] and would have to be coded first. However, a DEM model based on the developed methodology remains limited by the rigidity of the grains and is inherently incapable of accounting for intra-granular deformations. This limitation could eventually be overcome by implementing the recent advances in grain fragmentation modelling [Cantor et al., 2017].

Direct experimental validation As a preliminary validation, a good qualitative agreement has been found between the results of the performed simulations and the currently accessible experimental observations. Although needed, a direct quantitative comparison with experiments was not possible since a detailed characterization of the snow microstructure, needed as input for the developed model, is not supplied with available experimental results. However, an experimental campaign is currently under way [Peinke et al., 2018] where the deformation of snow induced by a cone penetration test is directly recorded by X-ray tomography. Such results will finally enable a direct comparison with the results of the developed numerical model of snow and to serve to either validate or ameliorate the developed numerical model.

Constitutive model Modern numerical approaches such as Material Point Method combined with the the ever-increasing computing power now showcase exciting perspectives for large-scale modelling of snow avalanches (Fig. 8.1). However, any approach to large-scale modelling of this complex phenomena relies crucially on the accurate description of the mechanical response of snow on the material scale. Promising steps towards a constitutive law for snow have recently been made with the introduction of the so-called Cohesive CamClay model [Gaume et al., 2018]. While in the latter work the failure response had to be assumed, the methodology developed in this PhD enables this response to be obtained directly from snow microstructure. Some features of the Cohesive CamClay, such as the closed failure envelopes, have already been confirmed in the scope of this PhD, while others remain to be validated. The developed methodology for obtaining a failure response of snow from the microstructure could thus be used to validate or ameliorate the remaining features of Cohesive CamClay, such as the softening function.

Figure 8.1: Simulation of a snow avalanche, performed with the Material Point Method and the use of Cohesive CamClay model [Gaume et al., 2018].

Database of mechanical properties Even though a quantitative response of three snow samples has successfully been simulated, the emphasis of this PhD has been on the exploration of the qualitative failure response of snow.

Before the large-scale simulations of snow avalanches could be used as an engineering tool, a database of mechanical responses of different snow samples needs to be built. This way, actual material parameters for different snow types will be made available for simulations. A large database of mechanical responses will also allow the influence of microstructure on the mechanical response of snow to be statistically explored. As a first step, the effects of microstructural anisotropy on the macroscopic response of snow could be analysed. As an ultimate goal, a functional dependence between the properties of a fabric tensor of snow microstructure and the material parameters of a constitutive model, such as the Cohesive CamClay could be sought.

Bibliography

Ai, J., Chen, J.-F., Rotter, J. M., and Ooi, J. Y. (2011). Assessment of rolling resistance models in discrete element simulations. *Powder Technology*, 206(3):269 – 282.

Albaba, A., Lambert, S., Nicot, F., and Chareyre, B. (2015). Relation between microstructure and loading applied by a granular flow to a rigid wall using dem modeling. *Granular Matter*, 17(5):603–616.

Allen, M. P. and Tildesley, D. J. (2017). *Computer simulation of liquids*. Oxford university press.

Alley, R. (1987). Firn densification by grain-boundary sliding: a first model. *Le Journal de Physique Colloques*, 48(C1):C1–249.

Amberger, S., Friedl, M., Goniva, C., Pirker, S., and Kloss, C. (2012). Approximation of objects by spheres for multisphere simulations in dem. *ECCOMAS-2012*.

Ancey, C. (2001). Snow avalanches. In *Geomorphological fluid mechanics*, pages 319–338. Springer.

Andò, E., Hall, S. A., Viggiani, G., Desrues, J., and Bésuelle, P. (2012). Experimental micromechanics: grain-scale observation of sand deformation. *Geotechnique Letters*, 2(3):107–112.

Arnaud, L., Gay, M., Barnola, J.-M., and Duval, P. (1998). Imaging of firn and bubbly ice in coaxial reflected light: a new technique for the characterization of these porous media. *Journal of Glaciology*, 44(147):326–332.

Blum, H. (1976). *Models for the Perception of Speech and Visual Form*, chapter A transformation for extracting new descriptors of shape. MIT Press.

Bradley, C., Brown, R., and Williams, T. (1977). Short notes: On depth hoar and the strength of snow. *Journal of Glaciology*, 18(78):145–147.

Bradshaw, G. and O'Sullivan, C. (2004). Adaptive medial-axis approximation for sphere-tree construction. *ACM Transactions on Graphics (TOG)*, 23(1):1–26.

Bucher, E. (1956). Contribution to the theoretical foundations of avalanche defense construction. Technical report, SNOW ICE AND PERMAFROST RESEARCH ESTABLISHMENT WILMETTE IL.

Cambou, B., Jean, M., and Radjaï, F. (2013). *Micromechanics of granular materials*. John Wiley & Sons.

Cantor, D., Azéma, E., Sornay, P., and Radjaï, F. (2017). Three-dimensional bonded-cell model for grain fragmentation. *Computational Particle Mechanics*, 4(4):441–450.

Capelli, A., Kapil, J. C., Reiweger, I., Or, D., and Schweizer, J. (2016). Speed and attenuation of acoustic waves in snow: Laboratory experiments and modeling with biot's theory. *Cold Regions Science and Technology*, 125:1–11.

Chandel, C., Mahajan, P., Srivastava, P., and Kumar, V. (2014a). The behaviour of snow under the effect of combined compressive and shear loading. *Current Science*, pages 888–894.

Chandel, C., Srivastava, P., and Mahajan, P. (2014b). Micromechanical analysis of deformation of snow using x-ray tomography. *Cold Regions Science and Technology*, 101:14–23.

Chiaia, B., Cornetti, P., and Frigo, B. (2008). Triggering of dry snow slab avalanches: stress versus fracture mechanical approach. *Cold Regions Science and Technology*, 53(2):170–178.

Clelland, M. and O'bannon, A. (2012). *Allen & Mike's avalanche book: A guide to staying safe in avalanche terrain*. Rowman & Littlefield.

Coeurjolly, D., Hulin, J., and Sivignon, I. (2008). Finding a minimum medial axis of a discrete shape is np-hard. *Theoretical Computer Science*, 206(1-2):72–79.

Colbeck, S. (1983). Theory of metamorphism of dry snow. *Journal of Geophysical Research: Oceans*, 88(C9):5475–5482.

Colbeck, S. (1998). Sintering in a dry snow cover. *Journal of Applied Physics*, 84(8):4585–4589.

Colbeck, S. C. (1974). The capillary effects on water percolation in homogeneous snow. *Journal of Glaciology*, 13(67):85–97.

Colbeck, S. C. (1997). A review of sintering in seasonal snow. Technical report, COLD REGIONS RESEARCH AND ENGINEERING LAB HANOVER NH.

Combe, G. and Roux, J.-N. (2009). Discrete numerical simulation, quasistatic deformation and the origins of strain in granular materials. *arXiv preprint arXiv:0901.3842*.

Cundall, P. and Strack, O. (1979). Discrete numerical model for granular assemblies. *Geotechnique*, 29(1):47–65.

Da Cruz, F., Emam, S., Prochnow, M., Roux, J.-N., and Chevoir, F. (2005). Rheophysics of dense granular materials: Discrete simulation of plane shear flows. *Physical Review E*, 72(2):021309.

da Cruz, F., Emam, S., Prochnow, M., Roux, J.-N., and Chevoir, F. m. c. (2005). Rheophysics of dense granular materials: Discrete simulation of plane shear flows. *Phys. Rev. E*, 72:021309.

Daouadji, A., Darve, F., Al Gali, H., Hicher, P., Laouafa, F., Lignon, S., Nicot, F., Nova, R., Pinheiro, M., Prunier, F., et al. (2011). Diffuse failure in geomaterials: Experiments, theory and modelling. *International Journal for Numerical and Analytical Methods in Geomechanics*, 35(16):1731–1773.

De Crécy, L. (1980). Avalanche zoning in france–regulation and technical bases. *Journal of Glaciology*, 26(94):325–330.

de Montmollin, V. (1982). Shear test on snow explained by fast metamorphism. *Journal of Glaciology*, 28(98):187–198.

De Quervain, M. (1966). *Problems of avalanche research*. na.

Drescher, A. and De Jong, G. D. J. (1972). Photoelastic verification of a mechanical model for the flow of a granular material. *Journal of the Mechanics and Physics of Solids*, 20(5):337–340.

Duclos, A. (1999). Déclenchement de plaques à distance. *Neige Avalanches*, 86:2–5.

Durand, Y., Giraud, G., Brun, E., Mérindol, L., and Martin, E. (1999). A computer-based system simulating snowpack structures as a tool for regional avalanche forecasting. *Journal of Glaciology*, 45(151):469–484.

Fardin, N., Stephansson, O., and Jing, L. (2001). The scale dependence of rock joint surface roughness. *International Journal of Rock Mechanics and Mining Sciences*, 38(5):659–669.

Ferellec, J.-F. and McDowell, G. R. (2010). A method to model realistic particle shape and inertia in dem. *Granular Matter*, 12(5):459–467.

Fierz, C. (2009). *The International Classification for Seasonal Snow on the Ground*. IHP-VI Technical Documents in hydrology. UNESCO/IHP.

Flin, F., Brzoska, J.-B., Lesaffre, B., Coléou, C., and Pieritz, R. A. (2004). Three-dimensional geometric measurements of snow microstructural evolution under isothermal conditions. *Annals of glaciology*, 38:39–44.

Föhn, P. M., Camponovo, C., and Krüsi, G. (1998). Mechanical and structural properties of weak snow layers measured in situ. *Annals of glaciology*, 26:1–6.

Fukuzawa, T. and Narita, H. (1992). An experimental study on the mechanical behavior of a depth hoar layer under shear stress. In *Proceedings of the International Snow Science Workshop in Breckenridge, Colorado*, pages 171–175.

Fyffe, B. and Zaiser, M. (2007). Interplay of basal shear fracture and slab rupture in slab avalanche release. *Cold Regions Science and Technology*, 49(1):26–38.

Gao, R., Du, X., Zeng, Y., Li, Y., and Yan, J. (2012). A new method to simulate irregular particles by discrete element method. *Journal of Rock Mechanics and Geotechnical Engineering*, 4(3):276 – 281.

Gaume, J. (2012). *Prédétermination des hauteurs de départ d'avalanches. Modélisation combinée statistique-mécanique*. PhD thesis, Grenoble.

Gaume, J., Gast, T., Teran, J., van Herwijnen, A., and Jiang, C. (2018). Dynamic anticrack propagation in snow. *Nature communications*, 9(1):3047.

Gaume, J., Löwe, H., Tan, S., and Tsang, L. (2017a). Scaling laws for the mechanics of loose and cohesive granular materials based on baxter's sticky hard spheres. *Physical Review E*, 96(3):032914.

Gaume, J., Schweizer, J., Herwijnen, A., Chambon, G., Reuter, B., Eckert, N., and Naaim, M. (2014). Evaluation of slope stability with respect to snowpack spatial variability. *Journal of Geophysical Research: Earth Surface*, 119(9):1783–1799.

Gaume, J., van Herwijnen, A., Chambon, G., Birkeland, K. W., and Schweizer, J. (2015). Modeling of crack propagation in weak snowpack layers using the discrete element method. *Cryosphere*, 9(5):1915–1932.

Gaume, J., van Herwijnen, A., Chambon, G., Wever, N., and Schweizer, J. (2017b). Snow fracture in relation to slab avalanche release: critical state for the onset of crack propagation. *The Cryosphere*, 11(1):217–228.

Gerling, B., Löwe, H., and van Herwijnen, A. (2017a). Measuring the elastic modulus of snow. *Geophysical Research Letters*, 44(21):11–088.

Gerling, B., Löwe, H., and van Herwijnen, A. (2017b). Measuring the elastic modulus of snow. *Geophysical Research Letters*, 44(21):11–088.

Giddings, J. C. and LaChapelle, E. (1962). The formation rate of depth hoar. *Journal of Geophysical Research*, 67(6):2377–2383.

Hagenmuller, P. (2014). *Modélisation du comportement mécanique de la neige à partir d'images microtomographiques*. PhD thesis, Université de Grenoble.

Hagenmuller, P., Calonne, N., Chambon, G., Flin, F., Geindreau, C., and Naaim, M. (2014a). Characterization of the snow microstructural bonding system through the minimum cut density. *Cold Regions Science and Technology*, 108:72–79.

Hagenmuller, P., Chambon, G., Flin, F., Morin, S., and Naaim, M. (2014b). Snow as a granular material: assessment of a new grain segmentation algorithm. *Granular Matter*, 16(4):421–432.

Hagenmuller, P., Chambon, G., Lesaffre, B., Flin, F., and Naaim, M. (2013). Energy-based binary segmentation of snow microtomographic images. *Journal of Glaciology*, 59(217):859–873.

Hagenmuller, P., Chambon, G., and Naaim, M. (2015). Microstructure-based modeling of snow mechanics: A discrete element approach. *Cryosphere*, 9(5):1969–1982.

Hagenmuller, P., Matzl, M., Chambon, G., and Schneebeli, M. (2016). Sensitivity of snow density and specific surface area measured by microtomography to different image processing algorithms. *Cryosphere*, 10(3):1039–1054.

Hagenmuller, P., Theile, T., and Schneebeli, M. (2014c). Numerical simulation of microstructural damage and tensile strength of snow. *Geophysical Research Letters*, 41(1):86–89.

Hart, R., Cundall, P., and Lemos, J. (1988). Formulation of a three-dimensional distinct element model—part ii. mechanical calculations for motion and interaction of a system composed of many polyhedral blocks. In *International Journal of Rock Mechanics and Mining Sciences & Geomechanics Abstracts*, volume 25, pages 117–125. Elsevier.

Haynes, F. D. (1973). Tensile strength of ice under triaxial stresses. Technical report, COLD REGIONS RESEARCH AND ENGINEERING LAB HANOVER NH.

Heierli, J., Gumbsch, P., and Zaiser, M. (2008). Anticrack nucleation as triggering mechanism for snow slab avalanches. *Science*, 321(5886):240–243.

Hill, R. (1958). A general theory of uniqueness and stability in elastic-plastic solids. *Journal of the Mechanics and Physics of Solids*, 6(3):236–249.

Hogue, C. (1998). Shape representation and contact detection for discrete element simulations of arbitrary geometries. *Engineering Computations*, 15(3):374–390.

Jamieson, B. and Johnston, C. D. (2001). Evaluation of the shear frame test for weak snowpack layers. *Annals of Glaciology*, 32:59–69.

Jamieson, J. and Johnston, C. (1992). Snowpack characteristics associated with avalanche accidents. *Canadian Geotechnical Journal*, 29(5):862–866.

Jamieson, J. and Johnston, C. (1995). Monitoring a shear frame stability index and skier-triggered slab avalanches involving persistent snowpack weaknesses. In *Proceedings International Snow Science Workshop, Snowbird, Utah, USA*, volume 30, pages 14–21.

Jamieson, J. B. and Schweizer, J. (2000). Texture and strength changes of buried surface-hoar layers with implications for dry snow-slab avalanche release. *Journal of Glaciology*, 46(152):151–160.

Jiusto, J. E. and Weickmann, H. (1973). Types of snowfall. *Bulletin of the American Meteorological Society*, 54(11):1148–1162.

Johnson, B. C., Jamieson, J. B., and Stewart, R. R. (2004). Seismic measurement of fracture speed in a weak snowpack layer. *Cold Regions Science and Technology*, 40(1-2):41–45.

Johnson, J. B. and Hopkins, M. A. (2005). Identifying microstructural deformation mechanisms in snow using discrete-element modeling. *Journal of Glaciology*, 51(174):432–442.

Joshi, S., Mahajan, P., and Upadhyay, A. (2006). Study of layered snow under shear and tension. In *Proceedings ISSW*, pages 165–173.

Keeler, C. and Weeks, W. (1968). Investigations into the mechanical properties of alpine snow-packs. *Journal of Glaciology*, 7(50):253–271.

Köchle, B. and Schneebeli, M. (2014). Three-dimensional microstructure and numerical calculation of elastic properties of alpine snow with a focus on weak layers. *Journal of Glaciology*, 60(222):705–713.

Kochmanová, N. and Tanaka, H. (2010). Role of microstructure in the mechanical behaviour of clay. In *Soil Behavior and Geo-Micromechanics*, pages 166–171.

Kovacs, A., Weeks, W., and Michitti, F. (1969). Variation of some mechanical properties of polar snow, camp century, greenland. usa cold regions research and engineering laboratory. *Research Report*, 276:33.

Kruggel-Emden, H., Rickelt, S., Wirtz, S., and Scherer, V. (2008). A study on the validity of the multi-sphere discrete element method. *Powder Technology*, 188(2):153–165.

Lade, P. V. (1992). Static instability and liquefaction of loose fine sandy slopes. *Journal of Geotechnical Engineering*, 118(1):51–71.

Lee, Y., Fang, C., Tsou, Y.-R., Lu, L.-S., and Yang, C.-T. (2009). A packing algorithm for three-dimensional convex particles. *Granular Matter*, 11(5):307–315.

Liu, J., Nicot, F., and Zhou, W. (2018). Sustainability of internal structures during shear band forming in 2d granular materials. *Powder Technology*, 338:458–470.

Love, A. E. H. (2013). *A treatise on the mathematical theory of elasticity*. Cambridge university press.

Markou, I. (2016). Effect of grain shape and size on the mechanical behavior of reinforced sand. *Procedia engineering*, 143:146–152.

Marshall, H.-P. and Johnson, J. B. (2009). Accurate inversion of high-resolution snow penetrometer signals for microstructural and micromechanical properties. *Journal of Geophysical Research: Earth Surface*, 114(F4).

McClung, D. (1977). Direct simple shear tests on snow and their relation to slab avalanche formation. *Journal of Glaciology*.

McClung, D. (1979a). Shear fracture precipitated by strain softening as a mechanism of dry slab avalanche release. *Journal of Geophisical Research*.

McClung, D. M. (1979b). Shear fracture precipitated by strain softening as a mechanism of dry slab avalanche release. *Journal of Geophysical Research: Solid Earth*, 84(B7):3519–3526.

McClung, D. M. (1987). *Mechanics of snow slab failure from a geotechnical perspective*. National Research Council Canada, Institute for Research in Construction.

Mede, T. (2018). Snow samples. https://osf.io/x59fh/.

Mede, T., Chambon, G., Hagenmuller, P., and Nicot, F. (2018a). A medial axis based method for irregular grain shape representation in dem simulations. *Granular Matter*, 20(1):16.

Mede, T., Chambon, G., Hagenmuller, P., and Nicot, F. (2018b). Snow failure modes under mixed load- ing. *Geophysical Research Letters*, page under revision.

Meister, R. (2002). Avalanches: warning, rescue and prevention. *Avalanche News*, 62:37–44.

Mellor, M. (1974). *A review of basic snow mechanics*. US Army Cold Regions Research and Engineering Laboratory.

Mollema, P. and Antonellini, M. (1996). Compaction bands: a structural analog for anti-mode i cracks in aeolian sandstone. *Tectonophysics*, 267(1-4):209–228.

Moran, P. A. (1950). Notes on continuous stochastic phenomena. *Biometrika*, 37(1/2):17–23.

Nakaya, U. (1958). Visco-elastic properties of snow and ice in greenland ice cap. *Journal of the Faculty of Science, Hokkaido University. Ser. 2*, 5(3):119–164.

Narita, H. (1980). Mechanical behaviour and structure of snow under uniaxial tensile stress. *Journal of Glaciology*, 26(94):275–282.

Narita, H. (1984). An experimental study on tensile fracture of snow. *Contributions from the institute of Low Temperature Science*, 32:1–37.

Nicot, F., Sibille, L., and Darve, F. (2009). Bifurcation in granular materials: An attempt for a unified framework. *International Journal of Solids and Structures*, 46(22-23):3938–3947.

Nicot, F., Xiong, H., Wautier, A., Lerbet, J., and Darve, F. (2017). Force chain collapse as grain column buckling in granular materials. *Granular Matter*, 19(2):18.

Peinke, I., Hagenmuller, P., Ando, E., Flin, F., Chambon, G., and Roulles, J. (2018). Three-dimensional measurements of the deformation of snow induced by a cone penetration test. In *EGU General Assembly Conference Abstracts*, volume 20, page 14148.

Perla, R. and LaChapelle, E. (1970). A theory of snow slab failure. *Journal of Geophysical Research*, 75(36):7619–7627.

Peters, J., Muthuswamy, M., Wibowo, J., and Tordesillas, A. (2005). Characterization of force chains in granular material. *Physical review E*, 72(4):041307.

Price, M., Murariu, V., and Morrison, G. (2007). Sphere clump generation and trajectory comparison for real particles. *Proceedings of Discrete Element Modelling 2007*.

Radjai, F. and Dubois, F. (2011). *Discrete-element modeling of granular materials*. Wiley-Iste.

Radjai, F., Wolf, D. E., Jean, M., and Moreau, J.-J. (1998). Bimodal character of stress transmission in granular packings. *Physical review letters*, 80(1):61.

Reiweger, I., Gaume, J., and Schweizer, J. (2015). A new mixed-mode failure criterion for weak snowpack layers. *Geophysical Research Letters*, 42(5):1427–1432.

Reiweger, I. and Schweizer, J. (2013). Weak layer fracture: facets and depth hoar. *Cryosphere*, 7(5).

Reiweger, I., Schweizer, J., Ernst, R., and Dual, J. (2010). Load-controlled test apparatus for snow. *Cold Regions Science and Technology*, 62(2-3):119–125.

Reuter, B., Proksch, M., Loewe, H., van Herwijnen, A., and Schweizer, J. (2013). On how to measure snow mechanical properties relevant to slab avalanche release. In *Proceedings ISSW*, pages 7–11.

Reuter, B. and Schweizer, J. (2018). Describing snow instability by failure initiation, crack propagation and slab tensile support. *Geophysical Research Letters*.

Schleef, S., Löwe, H., and Schneebeli, M. (2014). Hot-pressure sintering of low-density snow analyzed by x-ray microtomography and in situ microcompression. *Acta Materialia*, 71:185 – 194.

Schneebeli, M. (2004). Numerical simulation of elastic stress in the microstructure of snow. *Annals of Glaciology*, 38:339–342.

Schweizer, J. (1998). Laboratory experiments on shear failure of snow. *Annals of Glaciology*, 26:97–102.

Schweizer, J. (1999). Review of dry snow slab avalanche release. *Cold Regions Science and Technology*, 30(1-3):43–57.

Schweizer, J. (2014). On recent advances in applied snow and avalanche research. *Cold Regions Science and Technology*, (97):57–59.

Schweizer, J. and Jamieson, J. (2001). Snow cover properties for skier triggering of avalanches. *Cold Regions Science and Technology*, 33(2-3):207–221.

Schweizer, J., Jamieson, J., and Schneebeli, M. (2003). Snow avalanche formation. *Reviews of Geophysics*, 41(4):2–1 – 2–25.

Schweizer, J., Reuter, B., van Herwijnen, A., and Gaume, J. (2016). Avalanche release 101. In *Proceedings ISSW*, pages 1–11.

Shapiro, L. H., Johnson, J. B., Sturm, M., and Blaisdell, G. L. (1997). Snow mechanics: review of the state of knowledge and applications. Technical report, COLD REGIONS RESEARCH AND ENGINEERING LAB HANOVER NH.

Sheng, Y., Lawrence, C., Briscoe, B., and Thornton, C. (2004). Numerical studies of uniaxial powder compaction process by 3d dem. *Engineering Computations*, 21(2/3/4):304–317.

Shertzer, R. H. and Adams, E. E. (2011). Anisotropic thermal conductivity model for dry snow. *Cold Regions Science and Technology*, 69(2-3):122–128.

Sigrist, C. (2006). *Measurement of fracture mechanical properties of snow and application to dry snow slab avalanche release*. PhD thesis, ETH Zurich.

Šmilauer, V., Catalano, E., Chareyre, B., Dorofeenko, S., Duriez, J., Gladky, A., Kozicki, J., Modenese, C., Scholtès, L., Sibille, L., et al. (2010). Yade reference documentation. *Yade Documentation*, 474(1).

Smith, J. (1965). The elastic constants, strength and density of greenland snow as determined from measurements of sonic wave velocity. us cold regions research and engineering laboratory, hanover. Technical report, NH, Technical report 167, 18 p.

Sommerfeld, R. (1973). Statistical problems in snow mechanics. *USDA For Serv Gen Tech Rep RM Rocky Mt For Range Exp Stn For Serv US Dep Agric*.

Srivastava, P. K., Chandel, C., Mahajan, P., and Pankaj, P. (2016). Prediction of anisotropic elastic properties of snow from its microstructure. *Cold Regions Science and Technology*, 125:85–100.

Stolpner, S., Kry, P., and Siddiqi, K. (2012). Medial spheres for shape approximation. *IEEE Transactions on Pattern Analysis and Machine Intelligence*, 34(6):1234–1240.

Szabo, D. and Schneebeli, M. (2007). Subsecond sintering of ice. *Applied Physics Letters*, 90(15):151916.

Szarf, K., Combe, G., and Villard, P. (2009). Influence of the grains shape on the mechanical behavior of granular materials. *AIP Conference Proceedings*, 1145(1):357–360.

Terzaghi, K. (1951). *Theoretical soil mechanics*. Chapman And Hall, Limited.; London.

Theile, T., Löwe, H., Theile, T., and Schneebeli, M. (2011). Simulating creep of snow based on microstructure and the anisotropic deformation of ice. *Acta Materialia*, 59(18):7104–7113.

Tordesillas, A. and Muthuswamy, M. (2009). On the modeling of confined buckling of force chains. *Journal of the Mechanics and Physics of Solids*, 57(4):706–727.

Tordesillas, A., Zhang, J., and Behringer, R. (2009). Buckling force chains in dense granular assemblies: physical and numerical experiments. *Geomechanics and Geoengineering: An International Journal*, 4(1):3–16.

Upadhyay, A., Joshi, S., and Chandel, C. (2007). Tensile strength of snow using centrifugal technique. *Defence Science Journal*, 57(6):787.

Van Herwijnen, A. and Heierli, J. (2009). Measurement of crack-face friction in collapsed weak snow layers. *Geophysical Research Letters*, 36(23).

Van Herwijnen, A., Schweizer, J., and Heierli, J. (2010). Measurement of the deformation field associated with fracture propagation in weak snowpack layers. *Journal of Geophysical Research: Earth Surface*, 115(F3).

Walters, D. J. and Adams, E. E. (2012). Directional mechanical properties of radiation recrystallized snow layers from experimental testing. In *Proceedings International Snow Science Workshop, edited by: Johnson, J. and Conway, H., Anchorage, Alaska, USA*, pages 16–21. Citeseer.

Walters, D. J., Adams, E. E., Staron, P. J., and McKittrick, L. R. (2010). Shear deformation of radiation recrystallized near surface facets. In *Proceedings International Snow Science Workshop, edited by Osterhuber, R., Lake Tahoe, CA, USA*, pages 17–22.

Wan, R., Nicot, F., and Darve, F. (2017). *Failure in Geomaterials: A Contemporary Treatise*. Elsevier.

Wan, R., Pinheiro, M., Daouadji, A., Jrad, M., and Darve, F. (2013). Diffuse instabilities with transition to localization in loose granular materials. *International Journal for Numerical and Analytical Methods in Geomechanics*, 37(10):1292–1311.

Watts, R., Henderson, D., and Baxter, R. (1971). Hard spheres with surface adhesion: The percus-yevick approximation and the energy equation. *Advances in Chemical Physics: Chemical Dynamics: Papers in Honor of Henry Eyring*, pages 421–430.

Wautier, A., Bonelli, S., and Nicot, F. (2017). A micromechanical approach of suffusion based on a length scale analysis of the grain detachment and grain transport processes. In *EPJ Web of Conferences*, volume 140, page 09022. EDP Sciences.

Wautier, A., Bonelli, S., and Nicot, F. (2018). Micro-inertia origin of instabilities in granular materials. *International Journal for Numerical and Analytical Methods in Geomechanics*, 42(9):1037–1056.

Wautier, A., Geindreau, C., and Flin, F. (2015). Linking snow microstructure to its macroscopic elastic stiffness tensor: A numerical homogenization method and its application to 3-d images from x-ray tomography. *Geophysical Research Letters*, 42(19):8031–8041.

Wensrich, C. and Katterfeld, A. (2012). Rolling friction as a technique for modelling particle shape in dem. *Powder Technology*, 217:409–417.

Wittmer, J., Claudin, P., Cates, M., and Bouchaud, J.-P. (1996). An explanation for the central stress minimum in sand piles. *Nature*, 382(6589):336.

Zhao, T. (2017). *Coupled DEM-CFD Analyses of Landslide-Induced Debris Flows*. Springer.

Zhao, Y., Xue, Q., Huang, F.-x., Hu, X.-t., and Li, J.-s. (2016). Experimental study on the microstructure and mechanical behaviors of leachate-polluted compacted clay. *Environmental Earth Sciences*, 75(12):1006.